Max-Planck-Institut
für Meteorologie

MAX-PLANCK-GESELLSCHAFT

International Max Planck Research School
on Earth System Modelling

The impact of black carbon aerosol induced snow darkening on the radiation balance in ECHAM6: Quantifying the contribution of wildfires for present and future conditions

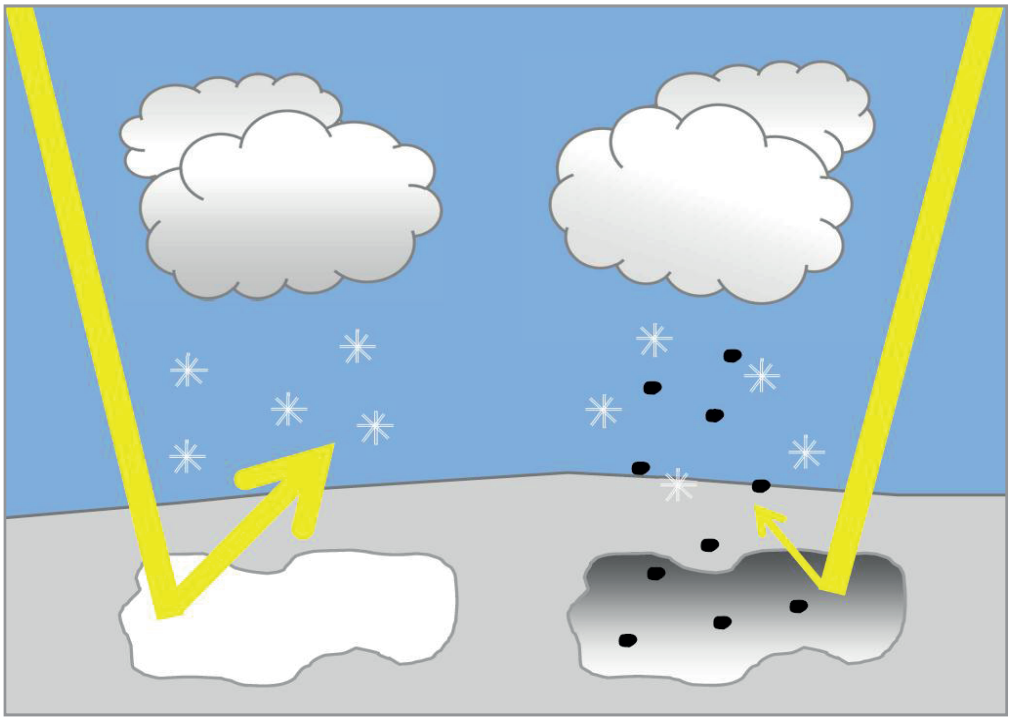

Jessica Engels

Hamburg 2016

Berichte zur Erdsystemforschung
Reports on Earth System Science

180
2016

Hinweis

Die Berichte zur Erdsystemforschung werden vom Max-Planck-Institut für Meteorologie in Hamburg in unregelmäßiger Abfolge herausgegeben.

Sie enthalten wissenschaftliche und technische Beiträge, inklusive Dissertationen.

Die Beiträge geben nicht notwendigerweise die Auffassung des Instituts wieder.

Die "Berichte zur Erdsystemforschung" führen die vorherigen Reihen "Reports" und "Examensarbeiten" weiter.

Notice

The Reports on Earth System Science are published by the Max Planck Institute for Meteorology in Hamburg. They appear in irregular intervals.

They contain scientific and technical contributions, including Ph. D. theses.

The Reports do not necessarily reflect the opinion of the Institute.

The "Reports on Earth System Science" continue the former "Reports" and "Examensarbeiten" of the Max Planck Institute.

Anschrift / Address

Max-Planck-Institut für Meteorologie
Bundesstrasse 53
20146 Hamburg
Deutschland

Tel./Phone: +49 (0)40 4 11 73 - 0
Fax: +49 (0)40 4 11 73 - 298

name.surname@mpimet.mpg.de
www.mpimet.mpg.de

Layout

Bettina Diallo and Norbert P. Noreiks
Communication

Copyright

The impact of black carbon aerosol induced snow darkening on the radiation balance in ECHAM6: Quantifying the contribution of wildfires for present and future conditions

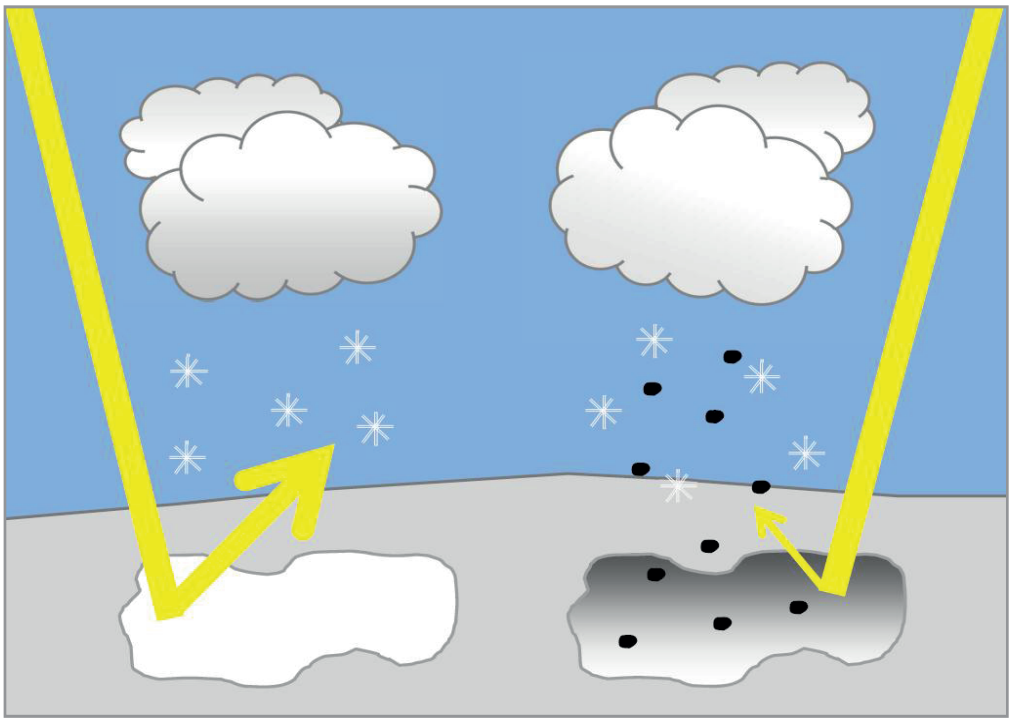

Dissertation with the aim of achieving a doctoral degree
at the Faculty of Mathematics, Informatics and Natural Sciences
Department of Earth Sciences of Universität Hamburg

submitted by

Jessica Engels

Hamburg 2016

Jessica Engels

Max-Planck-Institut für Meteorologie
Bundesstrasse 53
20146 Hamburg

Tag der Disputation: 26.4.2016

Folgende Gutachter empfehlen die Annahme der Dissertation:

Prof. Dr. Martin Claussen
Dr. Silvia Kloster

Berichte zur Erdsystemforschung / Max-Planck-Institut für Meteorologie 180
Reports on Earth System Science / Max Planck Institute for Meteorology 2016

ISSN 1614-1199

Abstract

The presence of light-absorbing black carbon (BC) aerosols counteracts the general cooling trend of aerosols in the Earth's atmosphere. Deposited on snow covered surfaces, BC aerosols enhance the absorption of solar radiation by the darkening of the snow. The stronger absorption leads to earlier snow melt, thereby triggering the snow-albedo-feedback. As shown in previous studies applying global circulation models (GCMs), already small amounts of BC aerosols deposited on snow cause relevant snow albedo changes. These changes influence the climate significantly, especially due to the high efficacy of the snow darkening effect compared to other forcing agents in the Earth System.

The present study gives a first estimate of the effect of the darkening of snow covered surfaces through BC aerosol deposition on the radiation balance for projected future conditions. In addition, the contribution of wildfire BC aerosols to the overall snow darkening effect was assessed, as wildfires represent one of the major contributors to the overall BC aerosol emissions. For this, the global general circulation model ECHAM6 of the Max Planck Institute Earth System Model (MPI-ESM) was extended by a snow-albedo-scheme which explicitly accounts for the snow darkening effect by BC aerosols. Simulations were performed for pre-industrial, present-day as well as projected future conditions, following the Representative Concentration Pathway 8.5 for the end of the 21st century. An evaluation of the model performance against measurements of BC concentrations in snow showed a reasonable performance of the new model framework. The effect of snow darkening by BC aerosols assessed in the present study is at the lower bound of other estimates for present-day conditions ($+6.69 \pm 3.14$ mWm^{-2}). For pre-industrial times, the effect decreases to about $+5.70 \pm 3.72$ mWm^{-2} and is projected to decline even more considerably for future conditions ($+1.85 \pm 1.67$ mWm^{-2}), especially in the Arctic region. Here, changes in climate and in BC aerosol deposition fluxes contribute equally to the reduction of the projected future radiative forcing compared to present-day. Locally, the radiative forcing due to BC aerosol deposition on snow e.g. in mountainous regions like in Tibet is high, exceeding values of $+1$ Wm^{-2}, supporting the large local impact of the snow darkening effect as discussed in previous studies.

The snow darkening effect of wildfire BC aerosol deposition will decline by 42 % between present-day und projected future conditions as a consequence of changes in climate and wildfire emissions. The contribution of wildfires to the overall snow darkening effect through BC aerosols amounts to 50 % for present-day and to 57 % for projected future conditions assuming that present-day anthropogenic BC aerosol emissions remain constant. Accounting for decreasing projected future anthropogenic BC aerosol emissions, leads to a wildfire contribution of about 90 % for the Arctic region.

Overall, the implemented snow-albedo-scheme provides a promising tool integrated in a GCM for the investigation of the snow darkening effect through the deposition of BC aerosols on snow. The snow darkening effect by BC aerosols is of low importance globally. Locally, however, the contribution to the overall aerosol-climate as well as wildfire-climate interactions will play a larger role. For projected future conditions, wildfires are the major contributor to the snow darkening effect by BC aerosol deposition compared to anthropogenic BC aerosol emission sources.

Zusammenfassung

Die Anwesenheit von Licht absorbierenden Rußaerosolen wirkt dem allgemeinen Kühlungseffekt von Aerosolen in der Erdatmosphäre entgegen. Rußaerosole lagern sich auf schneebedeckten Oberflächen ab, dunkeln den Schnee ab und verstärken so die Absorption solarer Einstrahlung. Die stärkere Absorption führt zu einer früheren Schneeschmelze und löst dabei die Schnee-Albedo-Rückkopplung aus. Vorangegangene Studien zeigen unter Verwendung von globalen Zirkulationsmodellen, dass schon geringe Mengen Ruß auf Schnee wesentliche Albedoänderungen verursachen. Diese Änderungen beeinflussen das Klima signifikant, besonders wegen der starken Effizienz des Schneeabdunklungseffekts im Vergleich zu anderen Strahlungsantrieben im Erdsystem.

Die vorliegende Studie untersucht den Effekt von abgedunkelten Schneeflächen durch Ruß auf die Strahlungsbilanz und liefert erstmals eine Abschätzung unter zukünftigen Bedingungen. Zusätzlich wurde der Anteil von Rußaerosolen durch Vegetationsbrände am gesamten Schneeabdunklungseffekt bestimmt, da Vegetationsbrände einen großen Teil zu den gesamten Rußaerosolemissionen beitragen. Dafür wurde das globale Zirkulationsmodell ECHAM6 des Erdsystemmodells des Max-Planck-Instituts um ein Schnee-Albedo-Schema erweitert, welches den Schneeabdunklungseffekt explizit berücksichtigt. Simulationen wurden für vorindustrielle und heutige Bedingungen durchgeführt. Für Simulationen unter zukünftigen Bedingungen wurde das Representative Concentration Pathway 8.5 am Ende des 21. Jahrhunderts berücksichtigt. Eine Evaluation der Modellergebnisse gegen Messungen der Rußkonzentration in Schnee zeigt eine sinnvolle Performanz der neuen Modellkomponente. Der sich ergebende heutige Schneeabdunklungseffekt durch Rußaeorosole liegt am unteren Rand der Abschätzungen anderer Studien ($+6.69 \pm 3.14$ mWm^{-2}). Für die vorindustrielle Zeit sinkt der Effekt auf ungefähr $+5.70 \pm 3.72$ mWm^{-2}. Unter zukünftigen Bedingungen sinkt der Effekt noch stärker ($+1.85 \pm 1.67$ mWm^{-2}) und wird besonders schwach in der arktischen Region. Hier tragen Änderungen im Klima und in den Flüssen der Rußaerosolablagerung gleichermaßen zum schwächeren Strahlungsantrieb im Vergleich zu heute bei. Lokal ist der Strahlungsantrieb durch Rußablagerung auf Schnee stärker als global und erreicht in Gebirgsregionen wie dem Tibet Werte über $+1$ Wm^{-2}.

Der Schneeabdunklungseffekt durch die Ablagerung von Ruß durch Vegetationsbrände nimmt zwischen heutigen und zukünftigen Bedingungen um 42 % ab. Ursachen dafür sind Änderungen im Klima und in Rußemissionen durch Vegetationsbrände. Unter der Annahme, dass die heutigen anthropogenen Rußemissionen konstant bleiben, steigt der Anteil von Vegetationsbränden am gesamten Schneeabdunklungseffekt durch Rußaerosole von 50 % für heutige auf 57 % für zukünftige Bedingungen. Die Annahme von abnehmenden anthropogenen Rußaerosolemissionen führt zu einem Anteil von 90 % durch Vegetationsbrände in der arktischen Region.

Insgesamt liefert das Schnee-Albedo-Schema im Rahmen eines GCMs ein überzeugendes Werkzeug, um den Schneeabdunkelungseffekt durch die Ablagerung von Ruß auf Schnee zu untersuchen. Auf globaler Skala ist der Schneeabdunklungseffekt schwach. Lokal beeinflusst er die Aerosol-Klima- und Vegetationsbrand-Klima-Wechselwirkungen stark. Im Vergleich zu anthropogenen Rußaerosolquellen tragen unter zukünftigen Bedingungen besonders Vegetationsbrände zum Schneeabdun-

klungseffekt durch Rußaerosolablagerungen bei.

Contents

Chapter 1

Introduction

1.1 Aerosols in the Earth System

For the most part the Earth's atmosphere is composed of gases. A small fraction of the mass or volume of the atmosphere, however, consists of solid and liquid matter in the form of particles. Despite their small mass fraction, these aerosol particles have a large impact on climate by their interaction with solar as well as terrestrial radiation. In addition, aerosols influence biogeochemistry and atmospheric chemical cycles (Boucher et al., 2013). The aerosols originate from a variety of natural as well as anthropogenic sources and are distinguished between primary and secondary aerosols: Primary aerosols are emitted directly from sources such as biomass burning (e.g. black and organic carbon), volcanic eruptions (e.g. volcanic ash), incomplete combustion of fossil fuels (e.g. black carbon), from arid land by wind erosion (mineral dust), and ocean surfaces (e.g. sea salt). The secondary aerosols are commonly formed by gas-to-particle conversion in the atmosphere from gaseous precursors.
In the atmosphere, aerosols have an impact on climate via their type-specific properties to scatter and absorb solar and terrestrial radiation influencing the atmospheric radiation balance (Mahowald et al., 2011). This is the so-called direct aerosol effect. The direct aerosol effect covers the changes in the radiation balance of the Earth system due to the scattering and the absorption of solar and the scattering, absorption, and emission of thermal radiation by aerosols (Haywood et al., 2000). The indirect aerosol effect results from the aerosols' property to serve as cloud or ice condensation nuclei (Pöschl, 2005). This indirect aerosol effect is split into two components, namely the cloud-albedo and the cloud-lifetime effect. The cloud-albedo effect describes that an increase in the aerosol concentration, at constant water content, causes smaller cloud droplets, thereby enhancing the reflection of solar radiation back into space by a cloud (Twomey, 1977). In addition, the smaller size and the larger number of cloud droplets reduce the efficiency of precipitation, increasing the cloud's lifetime (cloud-lifetime effect, Albrecht, 1989).
Several studies assessed the direct (e.g. Haywood et al., 2000; Myhre et al., 2013a) and the indirect (e.g. Lohmann and Feichter, 2005) aerosol effect by applying general circulation models (GCMs) including aerosol microphysical models. The best estimate for present-day conditions as summarized in the Fifth Assessment Report of the Intergovernmental Panel on Climate Change shows a radiative forcing of about -0.35 (-0.85 to +0.15) Wm^{-2} (Myhre et al., 2013b). Thus, the negative radiative forcing by aerosols compensates the global anthropogenic well-mixed greenhouse gas radiative

forcing (+2.83 (+2.54 to +3.12) Wm^{-2}; Myhre et al., 2013b) to a considerable degree (Charlson et al., 1992).
Aerosols do not only affect the atmosphere, but also the surface. When deposited on the surface, aerosols may darken snow covered surfaces and can modify the land as well as the ocean biogeochemistry through the deposition of nutrients (Mahowald et al., 2011). Finally, aerosols have an impact on air quality affecting public health (e.g. Dockery et al., 1993; Rabl and Spadaro, 2000).

1.2 Black carbon aerosols

Most aerosol species scatter solar radiation back to space thereby cooling the atmosphere. The presence of light-absorbing aerosols counteracts this cooling trend by absorbing visible light so that more energy remains in the Earth's atmosphere. The property of light-absorbing aerosols to absorb visible light in turn leading to a warming of the atmosphere was already identified by Charlson and Pilat (1969). The few particle species absorbing visible light inclose black carbon or 'soot', organic carbon species (usually referring to the carbon fraction of the aerosol which is not black) as well as dust. Here, in particular black carbon attracted special attention differing from the other aerosol types as no other substance in the atmosphere exists with such a strong ability to absorb visible light (Bond, 2004). Black carbon is a distinct type of carbonaceous material which is formed in flames by incomplete combustion of fossil fuels, biofuels and biomass. It is refractory, and insoluble. Once emitted, black carbon aerosols undergo regional and intercontinental transport until the particles are deposited on the Earth's surface after a short lifetime of a few days to weeks. The sources black carbon aerosols are emitted from are diverse and cover anthropogenic (e.g. industrial emissions, agricultural burning, traffic) as well as natural (e.g. wildfires) sources, summing up to emissions of about 7.5 $Tgyear^{-1}$ (2 to 29 $Tgyear^{-1}$) estimated by a bottom-up inventory method for the year 2000 (Bond et al., 2013). The comprehensive study on black carbon by Bond et al. (2013) provides a positive total radiative forcing by black carbon aerosols to sum up to about +1.1 (+0.17 to +2.1) Wm^{-2}. As the load of black carbon aerosols emitted into the atmosphere increased considerably over the industrial era (e.g. Bond et al., 2007), some studies suggested that a reduction in black carbon aerosols might potentially lead to a decline in the rate of global warming by lowering the positive radiative forcing due to black carbon aerosols (e.g. Hansen et al., 2000; Jacobson, 2005). However, even if there is an agreement among climate models that black carbon aerosols cause a warming on climate primarily in the Northern Hemisphere, the level of scientific understanding is still low to very low for many processes influencing the Earth System associated with black carbon aerosols (Bond et al., 2013).

1.2.1 Black carbon aerosol deposition on snow

One source of uncertainty with regard to the full effect of black carbon aerosols on climate is the deposition of black carbon aerosols on snow and ice. Very small

quantities of black carbon particles deposited on snow and ice covered surfaces, as well as sea ice, can reduce the albedo of snow and ice significantly (Warren and Wiscombe, 1980). For the Arctic, the albedo can be reduced by about 1.5 %, and the reduction in snow-covered Northern Hemisphere land regions can reach up to 3 % (Hansen and Nazarenko, 2004). Several global modelling studies (e.g. Jacobson, 2004; Flanner et al., 2007; Koch et al., 2009; Skeie et al., 2011) have assessed the effect of the deposition of black carbon aerosols on climate and are summarized in the IPCC AR5. Here, the present-day radiative forcing from black carbon on snow ranges from +0.01 to +0.08 Wm^{-2} (Boucher et al., 2013). The positive radiative forcing of the darkening of snow by the deposition of black carbon particles is small on the global scale, compared to other forcing agents within the Earth system. The effectiveness of this forcing is, however, large: the 'efficacy', the global mean temperature change per unit forcing produced by the deposition of black carbon aerosols on snow relative to the temperature response caused by atmospheric CO_2 forcing from the same initial climate state (Hansen, 2005), is 1.7 to 4.5 (e.g. Hansen and Nazarenko, 2004; Flanner et al., 2007; Flanner et al., 2009). The stronger response of the global mean temperature results from the fact that the radiative forcing is placed directly in the cryosphere, enhancing the temperature response by a number of positive feedbacks (Boucher et al., 2013; Pithan and Mauritsen, 2014). The sensitivity of the Arctic region particularly to Northern Hemisphere short-lived pollutants, was also suggested by Shindell and Faluvegi (2009), showing that black carbon is one substantial contributor to the rapid warming in the Arctic over the past three decades. Albedo reductions of the size as estimated in Hansen and Nazarenko (2004) have the potential to lead to a simulated global radiative forcing of about 0.16 Wm^{-2}, in turn causing a positive temperature response of about +0.24 K (Hansen, 2005).
The deposition of black carbon aerosols on snow can also influence the climate by changing the timing of snow melt (e.g. Jacobi et al., 2015), leading to an earlier exposure of the underlying darker soil which determines the snow and ice-albedo feedback (e.g. Hansen and Nazarenko, 2004; Jacobson, 2004; Flanner et al., 2007). Another factor which determines the strength of the snow albedo feedback is the metamorphism of the snow. Here, the age of the snow causes snow grains to grow, thereby leading to a lower albedo of the snow and a potential larger albedo perturbation when black carbon aerosols are deposited on the snow (e.g. Warren and Wiscombe, 1980; Flanner and Zender, 2006; Hadley and Kirchstetter, 2012).

Regionally, the radiative forcing related to the deposition of black carbon aerosols on snow and ice can be strong. Regions like the Himalayas, the Tibetan Plateau, and the Hindu Kush region have become of great interest (e.g. Xu et al., 2012). These regions are regarded as particularly vulnerable as they include numerous glaciers (e.g. Kääb et al., 2012) and snow-covered regions (e.g. Ménégoz et al., 2013) which are exposed to high radiation intensities due to the high altitude and lie in the proximity to large anthropogenic black carbon emission sources such as India or Southeast Asia. Modelling estimates provide an annual radiative forcing caused by the deposition of black carbon aerosols on snow of 1 to 3 Wm^{-2} in the Himalayas (Ménégoz et al., 2014) and of about 5 to 15 Wm^{-2} for the Tibetan Plateau (Kopacz et al., 2011). For the spring season, Flanner et al. (2007) estimate a radiative forcing over the Tibetan

Plateau exceeding 20 Wm^{-2}. A strong radiative forcing of this order can result in a retreat of glaciers (e.g. Xu et al., 2009) and the changes in the timing of snow melt (e.g. Flanner et al., 2007) which might have consequences for the hydrological cycle and the water resources in those regions, possibly affecting the living conditions of the population in that area concerning water availability and food security (e.g. Immerzeel et al., 2010).

Note that all estimates of the radiative forcing by the deposition of black carbon aerosols on snow are based on studies applying global climate models, which are related to large uncertainties. As an example, Jiao et al. (2014) quantified the spread in Arctic radiative forcing related to black carbon aerosol deposition on snow ranging from 0.06 to 0.28 Wm^{-2} using simulated black carbon deposition fields from 25 different state-of-the-art aerosol-climate models. The spread in the radiative forcing partly stems from varying models and model setups applied in the different studies e.g. different global emission inventories of black carbon aerosols, different atmospheric transport and deposition processes used in the different studies, different snow and ice cover representations among the models, different snow grain size and different melt water scavenging representations. A state-of-the-art tool to investigate the effect of the deposition of black carbon aerosols on snow is the snow albedo model SNICAR (Flanner et al., 2007; Flanner et al., 2009). The SNICAR model has been developed for the use in the Community Land Model (CLM) and calculates the snow albedo containing impurities as well as the evolution of the snow grain size. The SNICAR model has been implemented in other Earth System Models (ESMs, e.g. Sand et al., 2013).

However, most studies report present-day estimates of the radiative forcing related to the black carbon aerosol deposition on snow and ice, whereas studies for pre-industrial conditions are rare (e.g. Lawrence et al., 2012) and no study exists yet for projected future black carbon deposition and climate conditions. Thus, the present study aims to extend the current estimates by the assessment of the effect of the snow darkening by black carbon aerosols on the radiative forcing for pre-industrial and projected future conditions.

The use of satellite remote sensing to estimate the albedo reductions related to the deposition of black carbon aerosols on snow is in general not feasible (Warren, 2013). Typical black carbon concentrations in snow in remote areas of the Northern Hemisphere amount to about 3-30 $ng(BC)g(snow)^{-1}$ leading to a reduction of the snow albedo of cold fine-grained snow of a few percent (visible wavelength albedo 0-2 %). Snow albedo reductions of this size already lead to a significant influence on climate (e.g. Hansen and Nazarenko, 2004). However, factors like the surface roughness, thin clouds, and the patchiness as well as the thinness of the snow cover can alter the detected surface albedo in a similar range which makes the attribution of the small signal difficult. Zege et al. (2011) recommend using remote sensing to identify black carbon concentrations in snow only in highly polluted areas e.g. near industrial cities characterized by black carbon in snow content exceeding 1000 $ng(BC)g(snow)^{-1}$. In addition, a recent study by Polashenski et al. (2015) suggests that the detected

trend in declining albedo over the Greenland Ice Sheet (e.g. Stroeve et al., 2013; Dumont et al., 2014) partly results from uncorrected Terra satellite sensor degradation.

One parameter that allows to evaluate and to constrain the model performances is the concentration of black carbon aerosols in snow. Here, measurements of black carbon concentrations in snow have been conducted in several regions in the Northern Hemisphere like in large parts of the Arctic, China, and in Russia (e.g. Clarke and Noone, 1985; Doherty et al., 2010; Ye et al., 2012; Wang et al., 2013). As measuring black carbon concentrations in snow in remote regions like the Arctic or Antarctic is a challenging task, still not many studies are available and the spatial and temporal coverage of these studies is limited. Uncertainties in the estimated black carbon concentrations in snow arise e.g. from instrumental noise, systematic biases through the assumptions the data analysis is built on, uncertainty in the mass absorption efficiency of black carbon, and the question whether the analysed samples are representative for a broad region (Doherty et al., 2010). In addition, also a few laboratory measurements (e.g Hadley and Kirchstetter, 2012) and field studies (e.g. Conway et al., 1996; Brandt et al., 2011) treating pure snow with known impurity amounts are available. These studies provide an insight into the scavenging efficiency of black carbon aerosols out of the snowpack during melting as well as the accumulation of black carbon aerosols remaining at the surface of the snowpack after the melting process.

1.2.2 Fires as a source of black carbon aerosols

According to Bond et al. (2013), open burning represents one of the major sources of black carbon aerosol emissions. Here, vegetation fires or wildfires, whether set by humans or naturally by lightning, contribute to about 40 % to the total black carbon aerosol emissions (about 2.8 out of 7.5 Tgyear^{-1}). Wildfires are a global phenomenon and represent a key parameter influencing the Earth System, affecting e.g. ecosystems, land-surface properties, the carbon cycle, atmospheric chemistry, the cryosphere, and the climate.
Ward et al. (2012) estimated the radiative forcing of fires in pre-industrial climate conditions to sum up to about -1 Wm^{-2}, whereas the radiative forcing of fires increases to about -0.5 Wm^{-2} for the present-day period, and to -0.8 Wm^{-2} for projected future conditions (including impacts of greenhouse gas concentrations, aerosol effects, land and snow surface albedo). However, wildfires do not only influence climate by multiple processes, but are also controlled by climate conditions (Marlon et al., 2008; Bowman et al., 2009). To assess the complex wildfire-climate interactions, dynamic global vegetation models (DGVMs) are applied including e.g. sophisticated fire models like the process-based fire model SPITFIRE (Thonicke et al., 2010). The dominant source of uncertainties in the emission estimates of black carbon aerosols emitted from wildfires arise from the emission factors (Andreae and Merlet, 2001; Akagi et al., 2011), however, additional uncertainties arise from the information about fuel load, combustion completeness as well as burned area e.g. due to the deficiency of satellites to detect small fires (Randerson et al., 2012; Bond et al., 2013).
Wildfire emissions mostly result from wildfires occurring in tropical regions contribut-

ing about 80 % (Bond et al., 2013). However, according to Flannigan et al. (2009), future fire regimes will change and lead to a global increase in burned area, showing a high spatial variability also including areas of no change or decreases in some regions. Flannigan et al. (2009) also project a lengthening of the fire season for boreal and temperate regions in a warmer future climate. Especially for the northern high latitudes the fire season will potentially lengthen by more than 20 day per year by the end of the century (Flannigan et al., 2013). In addition, Westerling et al. (2006) suggest increasing wildfire activity along with higher temperatures for the Western United States. Black carbon aerosols emitted from wildfires which reduce the snow albedo on the Greenland Ice Sheet are hypothesized to have triggered melting events in the dry snow zone in 1889 and 2012 (Keegan et al., 2014).
However, no studies exist yet to assess the potential interaction of projected changes in future wildfire regimes and the climate influencing the effect of the deposition of wildfire black carbon aerosols on snow. Here, this study aims to give a first estimate of the contribution of wildfires to the overall snow darkening effect by black carbon aerosols.

1.3 Key research questions addressed in the present study

The overall scientific objective of the present study is to investigate whether the deposition of black carbon aerosols on snow affecting the radiation balance plays a key role for aerosol-climate as well as wildfire-climate interactions under pre-industrial, present-day and projected future climate conditions for the end of the 21st century. For this, a scheme to assess the effect of the deposition of black carbon aerosols on snow on the albedo is implemented in the atmospheric general circulation model ECHAM6 (Stevens et al., 2013) of the Max Planck Institute Earth System Model (MPI-ESM, Giorgetta et al., 2013). This new modelling framework allows to explore the following key research questions:

(i) How large is the radiative forcing caused by the darkening of snow covered surfaces through the deposition of black carbon aerosols for pre-industrial, present-day and future (end of the 21st century) climate states and black carbon aerosol deposition fluxes?

(ii) How much of the change in the radiative forcing caused by the black carbon deposition fluxes on snow covered surfaces between present-day and the future (end of the 21st century) can be attributed to changes in the climate and how much to changes in the aerosol deposition fluxes?

(iii) To what extent do black carbon aerosols released from wildfires contribute to the radiative forcing caused by snow darkening for present-day conditions and how might this contribution change with a different future (end of the 21st century) fire regime?

Chapter 2 of the present study introduces the new modelling framework to assess the effect of the deposition of black carbon aerosols on snow on the snow albedo which is implemented in ECHAM6 based on the SNICAR model. This new modelling framework is evaluated against observational data in chapter 3. Here, an important parameter is the simulated snow cover, which is compared against satellite-based observational data sets. The basis to assess the effect of the darkening of snow by black carbon aerosols is a correct representation of the concentrations of black carbon in snow. Thus, simulated black carbon concentrations in snow are compared to measurements. For this an evaluation data set has been compiled including measurement data of several campaigns conducted over widespread regions globally and during varying times periods.
Key research question (i) is addressed in chapter 4. The radiative forcing caused by the deposition of black carbon aerosols on snow covered land surfaces is analysed for pre-industrial, present-day, as well as future conditions. As future projection the present study applies the Representative Concentration Pathway 8.5 (RCP8.5) scenario (Riahi et al., 2007) for the end of the 21st century. The RCP8.5 scenario is selected to estimate the impact of a warmer climate on the snow darkening effect by BC aerosols for projected future conditions, as the RCP8.5 scenario is the strongest projection in terms of climate conditions compared to other RCP scenarios. Pre-industrial and projected future conditions are compared to present-day conditions which are summarized in chapter 3.
Sensitivity experiments have been performed to allow a factor separation to disentangle the impact of changes in climate conditions as well as the impact of changes in black carbon aerosol deposition fluxes on the change in the radiative forcing between present-day and the projected future addressing key research question (ii) in chapter 5.
Key research question (iii) is addressed in chapter 6. The radiative forcing by wildfire emissions through snow darkening is analysed for present-day and projected future climate conditions. Wildfire emissions have been estimated using the process-based fire regime model SPITFIRE. The radiative forcing is compared to the total radiative forcing estimated in key research question (i) as well as to the radiative forcing caused by projected changes in anthropogenic aerosol emissions in the future.
In the end, a summary and concluding remarks are found in chapter 7, and an outlook for further applications is provided as well as a summary of desirable improvements concerning future model development.

Chapter 2

Methodology

This chapter summarizes the design of the model and the experiments applied to assess the effect of black carbon (BC) aerosols deposited on land-based snow on the radiation balance. For this, the global circulation model ECHAM6 developed at the Max Planck Institute for Meteorology (MPI-M) including the land surface component JSBACH is used as described in section 2.1. The standard version of the land surface component JSBACH does not explicitly account for the deposition of BC aerosols on snow, but includes a simple snow albedo scheme accounting for the darkening of snow over time. This standard snow aging scheme considers e.g. the growth of the snow grain size and the enrichment of snow with impurity particles and is described in section 2.1.1. To account explicitly for the effect of snow darkening induced by the deposition of BC aerosols on snow on the radiation balance, the standard albedo scheme in JSBACH is extended by a snow-albedo-scheme which comprises two processes:

(i) The **mixing of BC aerosols into the snow** providing BC concentrations in snow in ng(BC)g(snow)$^{-1}$. Here, the mixing is implemented as a non-linear process by the distinction between four exclusive mixing cases depending on the available snow amount.

(ii) The **reduction of the snow albedo due to BC contamination of snow** using pre-calculated lookup tables. For this, snow albedos as a function of BC concentrations in snow depending on different snow grain sizes have been pre-calculated using the single-layer implementation of the Snow, Ice, and Aerosol Radiation (SNICAR) model (SNICAR-online; Flanner et al., 2007), which is a state-of-the-art snow albedo model, and are provided as lookup tables in JSBACH. The BC concentrations in snow obtained from the mixing scheme (i) and the snow age simulated in JSBACH were translated into snow albedo changes using these pre-calculated lookup tables.

The implemented snow-albedo-scheme combining the processes (i) and (ii) is described in section 2.1.2. Section 2.2 introduces the BC aerosol deposition fields based on standardized emission inventories used in this study and section 2.3 summarizes the experimental design for the single simulations performed for the present study.

2.1 Model Setup - the global circulation model ECHAM6

ECHAM6 is the latest version of the ECHAM atmospheric general circulation model of the Max Planck Institute Earth System Model (MPI-ESM; Giorgetta et al., 2013) described in Stevens et al. (2013) originating from a model version of the European Centre for Medium Range Weather Forecasts (ECMWF). All land surface processes in ECHAM6 are calculated by the land surface component JSBACH (Brovkin et al., 2013; Reick et al., 2013; Schneck et al., 2013). Each grid box in JSBACH is divided into fractional tiles which are covered by several Plant Functional Types (PFTs) representing sub-grid scale heterogeneity by combining different characteristics of natural and anthropogenic vegetation types. The radiative transfer for the shortwave and the longwave part of the electromagnetic spectrum in ECHAM6 is calculated separately using the rapid radiation transfer model as optimized for general circulation models (RRTM-G; Iacono et al., 2008). The two-stream approach calculates upward and downward irradiances by utilizing the correlated-k approach (k denotes absorption) to calculate longwave and shortwave fluxes as well as heating fluxes efficiently and accurately for the application to general circulation models. Changes in land surface properties e.g. vegetation and snow cover distribution affect amongst other parameters the land-surface albedo which in turn influences the radiation balance. The land-surface albedo representation in the standard version of ECHAM6 with a focus on the implementation of the snow age process over time is described in section 2.1.1. The improved snow albedo representation accounting for the effect of BC contamination of snow by the explicit deposition of BC aerosols on snow is summarized in section 2.1.2.

2.1.1 Surface albedo implementation with a focus on snow aging

Changes in the vegetation cover modify the physical properties of the land surface by influencing e.g. water, heat or radiation fluxes. The spatial and temporal changes in the surface albedo in ECHAM6 are calculated depending on the snow cover of the soil and the vegetation canopy, on the leaf area index (LAI), as well as on the desert fraction and the fractional vegetation cover distribution. The calculation is applied for the visible (VIS, 0.3-0.7 μm) and near infrared (NIR, 0.7-3.0 μm) range, respectively. If the surface is free of glaciers, the total surface albedo α is represented by a combination of one out of four albedo values: The albedo of surfaces covered by green leaves α_{leaf}, the albedo of soils α_{soil}, the albedo of snow covered soils α_{snow} and the albedo of snow covered vegetation canopy $\alpha_{snow,c}$. The albedo of snow covered canopy $\alpha_{\mathrm{snow,c}}$ is set to a constant value of 0.2. A detailed description of the albedo scheme is summarized in Otto et al. (2011). The composition of the total surface albedo α is illustrated in Figure 2.1.

The metamorphism of snow changes the snow albedo over time through for example the growth of the snow grain size, the enrichment of snow with impurity particles like soot or dust, as well as the presence of liquid water in the snow (e.g. Warren,

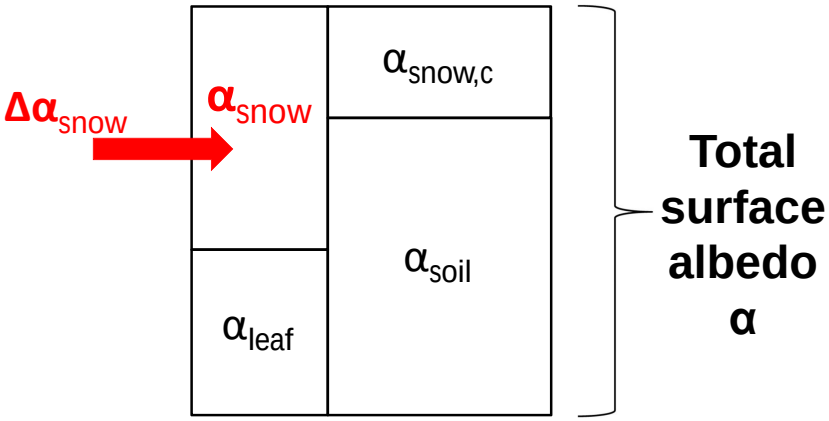

Figure 2.1: Scheme of the influence of the snow albedo reductions ($\Delta\alpha_{\text{snow}}$) on the total surface albedo (α) in the implemented snow-albedo-scheme in ECHAM6. The total surface albedo consists of the albedo of surfaces covered by green leaves (α_{leaf}), the albedo of snow covered soil (α_{snow}), the albedo of snow covered forest canopy ($\alpha_{\text{snow,c}}$), and the albedo of other soils (α_{soil}).

1982). Currently two different simple parametrizations are implemented in ECHAM6 to derive the darkening of the albedo of snow covered surfaces α_{snow}, which can be applied independently or as a linear combination.
The first parameterization is based on the former ECHAM5 parameterization described in detail in Roeckner et al. (2003) and Roesch and Roeckner (2006), assuming that the snow albedo α_{snow} decreases linearly with the surface temperature. Here, the temperature values range from the minimum value at the melting point ($\alpha_{\text{snow,vis}} = 0.5$, $\alpha_{\text{snow,nir}} = 0.3$) to a maximum value for temperatures below -5°C ($\alpha_{\text{snow,vis}} = 0.9$, $\alpha_{\text{snow,nir}} = 0.7$).
The second parameterization is based on the Biosphere-Atmosphere Transfer Scheme (BATS) described in Dickinson et al. (1986). The BATS scheme takes into account that snow ages over time accounting for influences from impurity deposition and snow grain growth caused by water vapour diffusion, and the freezing of meltwater which is combined in the so-called snow age factor. In the following, this key parameter of the BATS scheme, the snow age factor, is described in detail as this factor is used in the present study as input parameter for the explicit representation of the darkening of the snow albedo due to impurity deposition as described in the following section 2.1.2. This snow age factor f_{age} is defined as

$$f_{age} = \frac{\tau_{snow}}{1 + \tau_{snow}} \tag{2.1}$$

where τ_{snow} represents the non-dimensional age of snow. The snow age factor ranges between 0 and 1, where 0 indicates fresh snow and 1 aged snow. In Dickinson et al. (1986) the incremented non-dimensional age of snow is defined as follows

$$\Delta\tau_{snow} = (r_1 + r_2 + r_3)\frac{\Delta t}{\tau_0} \tag{2.2}$$

with $\tau_0^{-1} = 1 \cdot 10^{-6} s^{-1}$.

The term r_1 represents the effect of snow grain growth due to vapour diffusion and is expressed by

$$r_1 = exp\Big[5000(\frac{1}{273.15} - \frac{1}{T_S})\Big]$$

where T_S describes the surface temperature [K]. The second term r_2 represents the additional effect of snow grain growth near and at the freezing of meltwater,

$$r_2 = (r_1)^{10} \leq 1$$

and r_3 represents the effect of dirt and soot

$$r_3 = \begin{cases} 0.01 & \text{over Antarctica} \\ 0.3 & \text{elsewhere.} \end{cases}$$

The definition of τ_{snow} as implemented in JSBACH deviates from the formulation in Dickinson et al. (1986):

$$\tau_{snow}^{t+1} = (\tau_{snow}^{t} + \Delta\tau_{snow})\Big(1 - \frac{max(0, \Delta S_n)}{\Delta P_s}\Big) \tag{2.3}$$

where $t+1$ represents the current time step and ΔS_n is the snow water equivalent (in kgm^{-2}) in one time step Δt. ΔP_s is the amount of fresh snow required to restore the age of the snow, thus refreshing the snow albedo as well. Dickinson et al. (1986) suggest that at least a snow amount of 10 kgm^{-2} (10 mm water equivalent) is needed to restore the snow age and increases the snow albedo to its maximum value. In the current model version of JSBACH a threshold of 2 kgm^{-2} is used. Also the recommended distinction of the effect of dirt and soot between the Antarctic and elsewhere is not considered. Here, a value of 0.3 is applied globally.

2.1.2 Implemented snow-albedo-scheme to explicitly simulate the effect of the deposition of BC aerosols on the snow albedo

The current snow albedo scheme in ECHAM6 does not explicitly account for the deposition of BC aerosols on snow and the resulting reduction of the snow albedo. To improve the current snow albedo implementation in ECHAM6, first, the mixing of BC aerosols into the snow has been implemented in JSBACH as described in section 2.1.2.1. Second, the reduction of the snow albedo caused by BC aerosols mixed into the snow has been parameterized. The snow albedo values as function of BC concentrations in snow and snow age (considering different snow grain sizes) are obtained from the single-layer implementation of the SNICAR model (SNICAR-online; Flanner et al., 2007) and are described in section 2.1.2.2. The scheme combining the mixing of BC aerosols into the snow and the calculation of the snow albedo reductions due to the BC aerosol contamination of snow for different snow ages is named the *snow-albedo-scheme* in the following and is illustrated in Figure 2.2. This

snow-albedo-scheme has been only implemented to affect the snow albedo α_{snow} over land, not over sea ice. In addition, snow albedo reductions of the snow covered canopy $\alpha_{\text{snow,c}}$ are not taken into account. Here, the albedo of the snow covered canopy $\alpha_{\text{snow,c}}$ is set to a constant albedo value of 0.2 which is already a low albedo value so that reducing this snow albedo will play a minor role.

Compared to the comprehensive and complex standard SNICAR model (Flanner et al., 2007; Flanner et al., 2009) which has been developed for the use in the Community Land Model version 4 (CLM4; Oleson et al., 2010), some simplifications were required to match the given model structure of ECHAM6. Whereas the snow physics in the standard SNICAR model are represented in up to five snow layers including complex processes like thermal diffusion or vertically resolved melting and re-freezing (Flanner and Zender, 2005), the present study uses a simple single-layer snow model for the mixing of BC aerosols into the snow. Snow albedo changes are represented for snow grain sizes ranging from 50 to 1000 μm in the SNICAR model. In the present study, four snow grain sizes have been selected representing the snow grain growth over time.

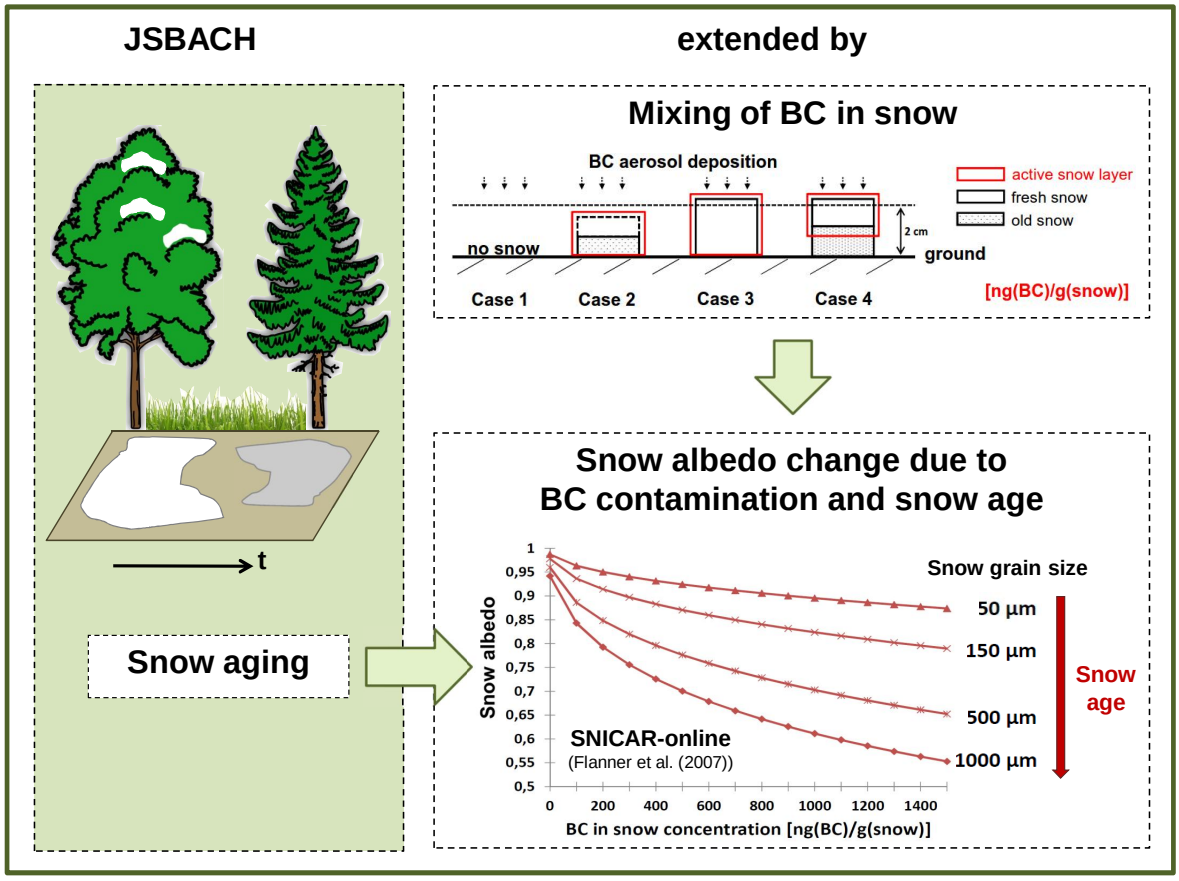

Figure 2.2: Illustration of the implemented snow-albedo-scheme in ECHAM6 to explicitly account for the deposition of BC aerosols on snow affecting the snow albedo. The snow aging in JSBACH (section 2.1.1) and the extension of JSBACH by the mixing of BC aerosols in snow (section 2.1.2.1) and by the snow albedo changes due to BC contamination of snow (section 2.1.2.2) are described in the main text.

2.1.2.1 Mixing of BC aerosols into the snow

To assess the effect of the darkening induced by BC aerosol deposition on snow on the radiation balance, first of all the BC aerosols deposited on the snow covered surface need to be mixed into the snow. For this, a simple scheme has been implemented in JSBACH to calculate the BC concentrations in snow. First, the available snow mass ($snow^{t+1}_{mass}$ in $\mathrm{kgm^{-2}}$) is calculated for every time step $t+1$ by

$$snow^{t+1}_{mass} = snow^{t}_{mass} + snow^{t+1}_{precip} \cdot \Delta t - snow^{t+1}_{melt} \cdot \Delta t. \tag{2.4}$$

The snow mass at the current time step $t+1$ is the sum of the snow mass available in the former time step $snow^{t}_{mass}$ and the fresh snowfall ($snow^{t+1}_{precip}$ in $\mathrm{kgm^{-2}s^{-1}}$) at the current time step reduced by the snowmelt ($snow^{t+1}_{melt}$ in $\mathrm{kgm^{-2}s^{-1}}$) of the current time step. Δt is the length of the time step in s. The snow mass is calculated over land as well as over glaciers.

Flanner and Zender (2005) show that about 20-45 % of the exponential decay of solar absorption with depth within a snowpack occurs even more than 2 cm beneath the surface. However, in most climate models the absorption occurring in a snowpack is limited to the top-most snow layer and occurs uniformly. Thus, an active snow layer (asl) of 2 cm was defined in the current implementation, characterizing the snow layer which is active in terms of radiative processes.

After determining the available snow layer by Equation 2.4, the available amount of BC aerosols deposited on the ground in every time step $t+1$ is calculated separately for soluble (s, dep^{t+1}_{s} in $\mathrm{kgm^{-2}s^{-1}}$) and insoluble (i, dep^{t+1}_{i} in $\mathrm{kgm^{-2}s^{-1}}$) BC aerosols. BC aerosol deposition fluxes are thereby prescribed in the model as described in section 2.2. The BC aerosol deposition fluxes of both the soluble and insoluble BC aerosols are the sum of the aerosol amount deposited by wet deposition (wetdep), dry deposition (drydep) as well as sedimentation (sedi)

$$dep^{t+1}_{s} = wetdep^{t+1}_{s} + drydep^{t+1}_{s} + sedi^{t+1}_{s} \tag{2.5}$$

$$dep^{t+1}_{i} = wetdep^{t+1}_{i} + drydep^{t+1}_{i} + sedi^{t+1}_{i}. \tag{2.6}$$

The BC aerosols are represented by four size classes: Nucleation, Aitken, accumulation, and coarse mode and are distinguished between insoluble and soluble modes. For this study, the sum of all size classes is taken into account, but separate for soluble and insoluble modes. With the obtained available amount of snow (Equation 2.4) as well as the amount of soluble and insoluble BC aerosols (Equations 2.5 and 2.6), the BC concentrations in snow in $\mathrm{ng(BC)g(snow)^{-1}}$ are calculated by distinguishing between four exclusive cases of the non-linear mixing of BC aerosols in the snow listed in the following and illustrated schematically in Figure 2.3.

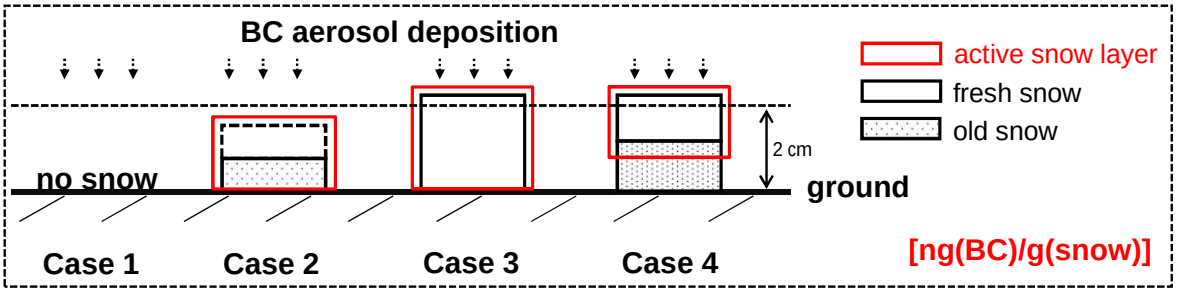

Figure 2.3: Scheme of the non-linear mixing of BC aerosols into the snow considering four different cases of snow layer conditions as implemented in ECHAM6 to provide BC concentrations in snow in ng(BC)g(snow)$^{-1}$.

Case 1: No snow is lying on the ground as well as no fresh snowfall occurs. The resulting BC concentrations in snow are zero ng(BC)g(snow)$^{-1}$.

Case 2: The snow depth is between 0 cm and the active snow layer. In this case either a layer of old snow is present which is lower than the active snow layer or fresh snow falls on the ground yielding a snow depth which is also lower than the defined active snow layer. In addition, also fresh snow can fall on a layer of old snow which sums up to a total snow layer which is lower than the active snow layer. Here, the amount of soluble (BC_s^{t+1} in kgm^{-2}) and insoluble (BC_i^{t+1} in kgm^{-2}) BC aerosols in snow is defined separately as follows

$$BC_s^{t+1} = BC_s^t + dep_s^{t+1} \cdot \Delta t - scavenging_s^{t+1} \tag{2.7}$$

$$BC_i^{t+1} = BC_i^t + dep_i^{t+1} \cdot \Delta t - scavenging_i^{t+1} \tag{2.8}$$

with

$$scavenging_s^{t+1} = \frac{0.2 \cdot snow_{melt}^{t+1} \cdot \Delta t \cdot BC_s^t}{snow_{mass}^{t+1}} \tag{2.9}$$

$$scavenging_i^{t+1} = \frac{0.03 \cdot snow_{melt}^{t+1} \cdot \Delta t \cdot BC_i^t}{snow_{mass}^{t+1}}. \tag{2.10}$$

The BC in snow content for soluble and insoluble BC aerosols is described by the sum of the BC in snow content of the former time step and the BC aerosol deposition of the current time step reduced by the scavenging of BC aerosols during the melting process. The terms $scavenging_s^{t+1}$ and $scavenging_i^{t+1}$ in kgm^{-2} represent the scavenging of BC aerosols during the melting process out of the BC in snow content of the former time step (BC_s^t, BC_i^t). The equations are adapted from equation 7.35 of the technical description of the Community Land Model (CLM) version 4.0 (Oleson et al., 2010). Here, the amount of 20 % of soluble BC aerosols is assumed to be removed during snow melt, whereas only 3 % of

the insoluble BC aerosol amount is washed out during melting. These values are consistent with the values used for the scavenging process in Flanner et al. (2007) based on observations of aerosol transport with snow meltwater from Conway et al. (1996). However, the uncertainty related to these observed values is large. Limitations arise from the fact that the parameters are only distinguished between soluble and insoluble BC aerosols and not between the different size classes (nucleation, Aitken, accumulation, and coarse mode). The BC aerosols are mixed uniformly in the available snow layer. The BC concentrations in snow (BC_{con}^{t+1} in kg(BC)kg(snow)$^{-1}$) for the current time step $t+1$ arise from the sum of the soluble and insoluble BC in snow content divided by the available snow mass

$$BC_{con}^{t+1} = \frac{(BC_s^{t+1} + BC_i^{t+1})}{snow_{mass}^{t+1}}. \tag{2.11}$$

Case 3: The snow depth of fresh snowfall is higher than the active snow layer. This case serves as a form of 'reset case'. If the fresh snowfall exceeds the height of the active snow layer, only the total height of the fresh snow layer is taken into account neglecting underlying old snow including former BC concentrations in snow. Thus, this case excludes the scavenging of BC aerosols during the melting process. The BC aerosols of the current time step $t+1$ are mixed uniformly into the snow layer. For this, the amount of deposited soluble as well as insoluble BC aerosols is calculated following Equations 2.5 and 2.6. The BC concentration in snow is calculated as follows

$$BC_{con}^{t+1} = \frac{(dep_s^{t+1} \cdot \Delta t + dep_i^{t+1} \cdot \Delta t)}{snow_{precip}^{t+1}}. \tag{2.12}$$

Case 4: Fresh snowfall on a layer of old snow exceeds the height of the active snow layer. If fresh snow (less than 2 cm) falls on top of a layer of old snow which altogether exceeds the height of the active snow layer, the upper 2 cm of the defined active snow layer are taken into account where the deposited BC aerosols are mixed into uniformly. Thus, this case considers new snowfall, but the old snow layer beneath the fresh snow still affects the BC concentrations in snow of the current time step $t+1$. This case includes the possibility that the old snow layer of the former time step rises above the defined height of the active snow layer. However, this case ensures that only the upper 2 cm of the snow layer are taken into account. The amount of the deposited BC aerosols is calculated following Equations 2.5 and 2.6. The BC concentrations in snow for soluble as well as insoluble aerosols in the snow, respectively, are calculated by

the following equations

$$BC_s^{t+1} = \frac{(asl \cdot \rho_{snow} - snow_{precip}^{t+1} \cdot \Delta t) \cdot BC_s^t}{asl \cdot \rho_{snow}} + \frac{(snow_{precip}^{t+1} \cdot dep_s^{t+1}) \cdot \Delta t)}{asl \cdot \rho_{snow}} - scavenging_s^{t+1} \tag{2.13}$$

$$BC_i^{t+1} = \frac{(asl \cdot \rho_{snow} - snow_{precip}^{t+1} \cdot \Delta t) \cdot BC_i^t}{asl \cdot \rho_{snow}} + \frac{(snow_{precip}^{t+1} \cdot dep_i^{t+1}) \cdot \Delta t)}{asl \cdot \rho_{snow}} - scavenging_i^{t+1}. \tag{2.14}$$

Here, asl represents the defined active snow layer of 2 cm and ρ_{snow} corresponds to the density of snow with 300 kgm^{-3}. The equations 2.13 and 2.14 consist of three parts: The BC concentrations in snow available in the old snow layer in relation to the active snow layer of 2 cm, the amount of BC aerosol deposition is mixed into the remaining fresh snow layer as well as the scavenging of BC aerosols by the melting process as defined in Equations 2.9 and 2.10. The total BC concentration in snow is calculated as follows

$$BC_{con}^{t+1} = \frac{(BC_s^{t+1} + BC_i^{t+1})}{asl \cdot \rho_{snow}}. \tag{2.15}$$

The BC concentrations in snow are restricted by an upper bound of 1500 ng(BC)g(snow)$^{-1}$ and serve as an input parameter for the calculation of the snow albedo reductions.

2.1.2.2 Calculation of the snow albedo reductions due to BC contamination and snow age

The snow albedo reductions due to BC concentrations in snow is implemented in JSBACH based on SNICAR-online (http://snow.engin.umich.edu/info.html; Flanner et al., 2007). This single-layer implementation of the Snow, Ice, and Aerosol Radiation (SNICAR) model (Flanner et al., 2007; Flanner et al., 2009), which is a state-of-the-art snow albedo model, provides the snow albedo for unique combinations of impurity content (BC, dust, and volcanic ash), different snow grain effective radii and varying incident solar flux characteristics. The standard SNICAR model applies a multi-layer two-stream radiative transfer approximation based on Warren and Wiscombe (1980) and Toon et al. (1989). In addition, the SNICAR model treats snow as a collection of ice spheres, obtaining Mie parameters like the single scattering albedo and the extinction coefficient for lognormally distributed aerosols from offline-computed lookup tables (Flanner and Zender, 2006). In the online version, the radiative transfer solution applied is a single-layer version of the multiple-scattering, multi-layer approximation

described by Toon et al. (1989). Hadley and Kirchstetter (2012) extensively verified the SNICAR model against laboratory measurements, showing a good agreement between simulated and measured snow albedo reductions attributed to the black carbon aerosol deposition on snow.

The SNICAR-online model provides the opportunity to vary parameters like the incident radiation (diffuse or direct), the solar zenith angle, the surface spectral distribution, the snowpack thickness and density, as well as the albedo of the underlying ground. From this SNICAR-online model, albedo values as a function of BC concentrations in snow and wavelengths (provided in 0.01 μm intervals) are obtained for selected snow grain sizes. The parameters chosen for the calculation are summarized in Appendix A. The calculation was done separately for the visible (0.3-0.7 μm) and the near-infrared (0.7-1.5 μm) range. The albedo values for the visible and near-infrared range are spectrally weighted into broadband albedo according to incident solar flux (Thomas and Stamnes, 1999). Here, surface incident fluxes typical of mid-latitude winter and Summit, Greenland, for clear-sky and cloudy conditions are used, generated with the atmospheric Shortwave Narrowband Model (SWNB) (Stamnes et al., 1988; Zender et al., 1997). For the present study, BC concentrations in snow were varied between 0 and 1500 ng(BC)g(snow)$^{-1}$ for 16 intervals with a width of 100 ng(BC)g(snow)$^{-1}$. The age of snow is accounted for by assigning different snow grain sizes to different snow ages. Thus, the calculations were done for four snow grain sizes (50, 150, 500, 1000 μm, respectively). A radius of 50 μm corresponds to fresh snow, whereas a radius of 1000 μm corresponds to old snow. Figure 2.4 represents the obtained snow albedos for the visible and near-infrared range as a function of BC concentrations in snow and snow age. Both the visible as well as the near-infrared range show a strong sensitivity of the snow albedo contaminated by BC aerosols on the snow grain size. Only small amounts of BC aerosols mixed in the snow are needed to alter the snow albedo significantly. The larger snow albedo changes occur in the visible range. Here, a maximum snow albedo change of up to 0.407 can be reached in the implemented scheme, whereas the possible maximum change in the snow albedo for the near-infrared range reaches a value of 0.205. Thus, the analysis in this study is restricted to snow albedo changes in the visible range.

The snow albedo reductions $\Delta\alpha_{\text{snow}}$ due to BC contamination influence the total surface albedo α via the snow albedo α_{snow} in ECHAM6. The relation of the snow albedo α_{snow} to the total surface albedo is illustrated in Figure 2.1. The snow albedo reduction is determined by subtracting the snow albedo for a BC concentration in snow at time step $t+1$ ($\alpha^{t+1}_{snow,BC^{t+1},vis}$, $\alpha^{t+1}_{snow,BC^{t+1},nir}$) from the snow albedo for a BC concentration in snow of zero ($\alpha^{t+1}_{snow,BC=0,vis}$, $\alpha^{t+1}_{snow,BC=0,nir}$). The snow albedo reductions are calculated separately for the visible as well as near-infrared range ($\Delta\alpha^{t+1}_{snow,vis}$, $\Delta\alpha^{t+1}_{snow,nir}$).

$$\Delta\alpha^{t+1}_{snow,vis} = \alpha^{t+1}_{snow,BC=0,vis} - \alpha^{t+1}_{snow,BC^{t+1},vis} \tag{2.16}$$

$$\Delta\alpha^{t+1}_{snow,nir} = \alpha^{t+1}_{snow,BC=0,nir} - \alpha^{t+1}_{snow,BC^{t+1},nir}. \tag{2.17}$$

In addition, this calculation has to take into account the snow grain size dependency. For this study, the snow age factor as derived in the BATS scheme is used to estimate the respective grain size of the snow. Here is assumed that a snow age of 0 equals fresh snow with a grain size of 50 μm, a snow age of 0.1 is assigned to a grain size of 150 μm, a snow age of 0.5 is assigned to a grain size of 500 μm, and a snow age of 1.0 is assigned to a grain size of 1000 μm. This grain size information allows to interpolate between the different snow albedo values representative for different snow grain sizes. The resulting snow albedo reductions ($\Delta\alpha^{t+1}_{snow,vis}$, $\Delta\alpha^{t+1}_{snow,nir}$) are subtracted from the snow albedo α_{snow} influencing the total surface albedo in ECHAM6 as shown in Figure 2.1, and subsequently altering the radiation balance.

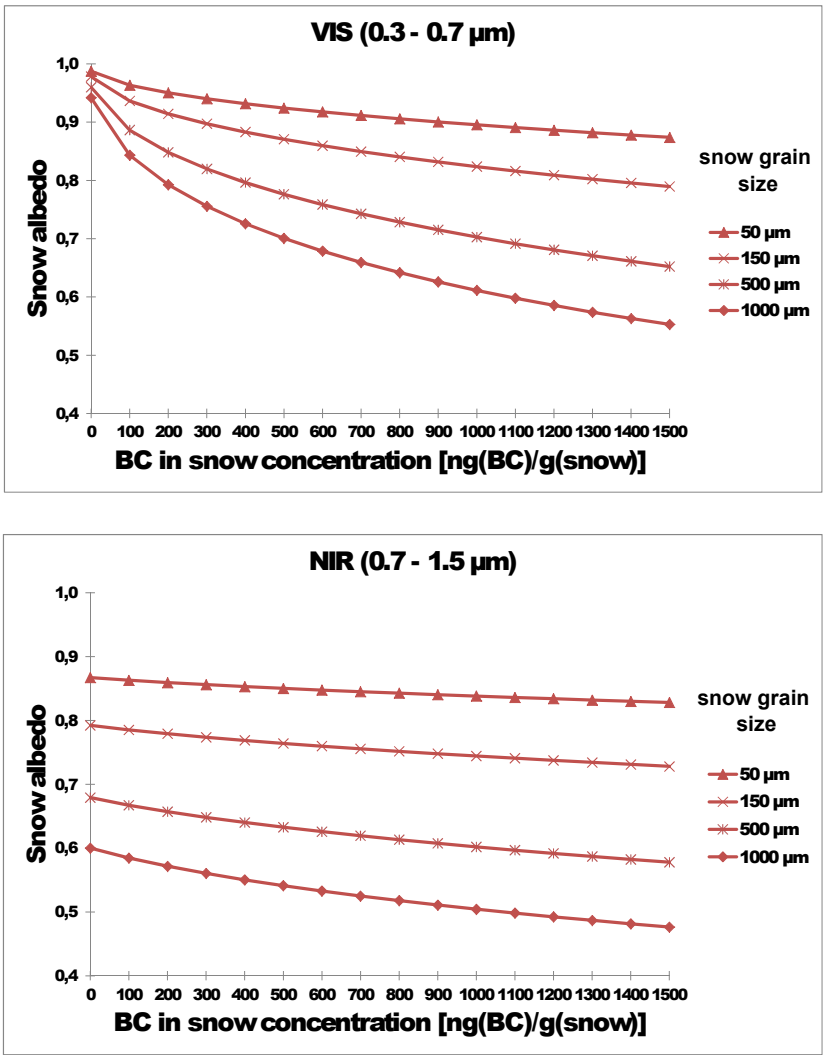

Figure 2.4: Snow albedo dependency on BC concentrations in snow provided by the single-layer simulator SNICAR-online (Flanner et al., 2007, http://snow.engin.umich.edu/info.html) for the visible (VIS, top) and near-infrared (NIR, bottom) for different snow grain sizes (50, 150, 500, 1000 μm) representing different snow ages.

2.2 Black carbon deposition fluxes simulated with ECHAM6-HAM2

The BC aerosol deposition fluxes which are prescribed in the ECHAM6 simulations for the present study are described in the following. Here, the BC aerosol deposition fluxes caused by all emission sources are taken into account for pre-industrial, present-day and projected future conditions. As the anthropogenic BC aerosol emissions used to derive the BC aerosol deposition fluxes are all based on the Atmospheric Chemistry and Climate Model Intercomparison Project (ACCMIP; Lamarque et al., 2010) data set, this model setup is referred to as the *ACCMIP-setup* in the following.

BC aerosol deposition fluxes were taken from former ECHAM6 simulations including the aerosol module HAM2.2. The model setup used to provide the BC aerosol deposition fluxes covering the pre-industrial (PI) and the present-day (PD) time period is described in detail in Stanelle et al. (2014) only differing in the model version: In Stanelle et al. (2014) ECHAM6-HAM2.1 was used whereas for the present study the latest version ECHAM6-HAM2.2 was used. This development was based on studies by Bourgeois and Bey (2011) and von Hardenberg et al. (2012) which verified an underestimation in the long-range transport of BC aerosols resulting from an overestimation of wet deposition during the aerosol transport from the mid-latitudes to the Arctic regions in ECHAM5-HAM1. As the long-range transport is essential for the BC aerosol deposition fluxes in the Arctic, in this study the improved model version including a more physically based wet deposition scheme was applied. However, the aerosol long-range transport is still too weak in the current model version which is supported by too low simulated BC concentrations in snow north of 70°N as shown in the model evaluation of BC concentrations in snow in section 3.2.
To assess the effect of BC aerosol deposition on snow in the future, the Representative Concentration Pathway (RCP) 8.5 is used, which represents the strongest scenario in terms of climate leading to lower snow cover compared to present-day conditions. In the RCP8.5, high population density combined with a slow income growth is projected leading to a high energy demand and highest greenhouse gas emissions compared to the other RCP scenarios at long sight. While climate mitigation policies are absent in the RCP8.5 scenario, air quality legislation plays an important role leading to a significant decline of the emissions towards the end of the century (Riahi et al., 2007). In the simulation performed for the projected future time period (2090-2099) to receive future BC aerosol deposition fields, greenhouse gases, sea surface temperatures (SSTs), sea ice concentrations (SICs), and land cover taken from the Coupled Model Intercomparison Project Phase 5 (CMIP5) simulations with MPI-ESM-LR (member r1i1p1)(Giorgetta et al., 2013) are prescribed. This differs from the simulation setup as used in Stanelle et al. (2014) for the pre-industrial and present-day time period where these parameters are taken from the Atmosphere Model Intercomparison Project 2 (AMIP II). The emissions of anthropogenic aerosols are taken from the Atmospheric Chemistry and Climate Model Intercomparison Project (ACCMIP, Lamarque et al., 2010) data set for the RCP8.5 scenario (van Vuuren et al., 2011; Riahi et al., 2007) which were used as well for pre-industrial and present-day conditions in Stanelle et al.

Table 2.1: Global total (top) as well as total Arctic (60°N-90°N, bottom) BC aerosol deposition fluxes and standard deviations in Tgyear^{-1} as simulated in ECHAM6-HAM2.2 for the pre-industrial (PI, 1880-1889), present-day (PD, 2000-2009), and projected future (RCP85, 2090-2099) time period. Shown is the total amount of BC aerosols deposited as annual (ANNUAL) as well as seasonal means (DJF, MAM, JJA, and SON).

Total BC aerosol deposition fluxes	**GLOBAL**		
[**Tgyear^{-1}**]	PI	PD	RCP85
ANNUAL	3.90 ± 0.08	7.41 ± 0.49	4.45 ± 0.59
DJF	3.76 ± 0.10	7.86 ± 0.20	4.62 ± 0.23
MAM	3.50 ± 0.09	7.05 ± 0.13	3.86 ± 0.22
JJA	3.95 ± 0.09	7.29 ± 0.43	4.76 ± 0.59
SON	4.40 ± 0.07	7.45 ± 0.59	4.56 ± 0.67
	ARCTIC		
	PI	PD	RCP85
ANNUAL	0.22 ± 0.01	0.22 ± 0.05	0.10 ± 0.07
DJF	0.15 ± 0.01	0.17 ± 0.03	0.04 ± 0.01
MAM	0.21 ± 0.02	0.23 ± 0.04	0.09 ± 0.04
JJA	0.28 ± 0.02	0.25 ± 0.03	0.19 ± 0.05
SON	0.25 ± 0.02	0.24 ± 0.06	0.10 ± 0.04

(2014).

Table 2.1 summarizes the global total as well as total Arctic (60°N-90°N) BC aerosol deposition fluxes in Tgyear^{-1} as simulated in ECHAM6-HAM2.2 for the three time periods pre-industrial (PI, 1880-1889), present-day (PD, 2000-2009) and the projected future (RCP85, 2090-2099), respectively. Here, the total BC aerosol deposition fluxes are shown as annual (ANNUAL) as well as seasonal (DJF, MAM, JJA, SON) means. The BC aerosol deposition fluxes represent total deposition fluxes including the nucleation, Aitken, accumulation, and the coarse BC mode for the soluble as well as the insoluble state covering wet and dry deposition as well as sedimentation. On the global scale, the PD period shows the highest amount of BC aerosol deposition fluxes with 7.4 Tgyear^{-1}. The PI period shows about 47 % (3.9 Tgyear^{-1}) lower BC aerosol deposition fluxes, the RCP85 simulation about 40 % (4.5 Tgyear^{-1}) lower BC aerosol deposition fluxes compared to the PD period. Note here that the PI time period in the present study covers the end of the 19$^{\text{th}}$ century at the time when the industrial revolution was already well underway. Thus, even lower BC aerosol deposition fluxes would be expected for the time period before the start of the industrial revolution. Restricting the region to the Arctic stretching out over 60°N to 90°N, the amounts of BC aerosol deposition fluxes show almost equal values for the PI and PD period with 0.22 Tgyear^{-1}, whereas the RCP85 simulation shows about 54 % (0.10 Tgyear^{-1}) lower BC aerosol deposition fluxes for the Arctic region compared to the PD simulation. The present-day BC aerosol deposition fluxes fall well within the range of Arctic BC aerosol deposition fluxes reported by Jiao et al. (2014): In this study, 25 different models par-

ticipating in the two phases of the Aerosol Comparisons between Observations and Models (AeroCom) project simulating BC aerosol deposition fluxes are compared. According to Myhre et al. (2013a), most of the models participating in AeroCom phase II have used anthropogenic aerosol emissions based on ACCMIP (Lamarque et al., 2010). As the anthropogenic aerosol emissions used in Stanelle et al. (2014) are also based on ACCMIP (Lamarque et al., 2010), the resulting BC aerosol deposition fluxes used in the present-study should be comparable. Jiao et al. (2014) report present-day Arctic BC aerosol deposition fluxes which range from 0.11 to 0.23 Tgyear^{-1} for the phase I models and from 0.13 to 0.34 Tgyear^{-1} for the phase II models. This compares nicely to the 0.22 Tgyear^{-1} applied in this study.

Regarding the different seasons on a global scale, the highest BC aerosol deposition fluxes are reached in JJA for the RCP85 simulation (4.76 Tgyear^{-1}), whereas for the

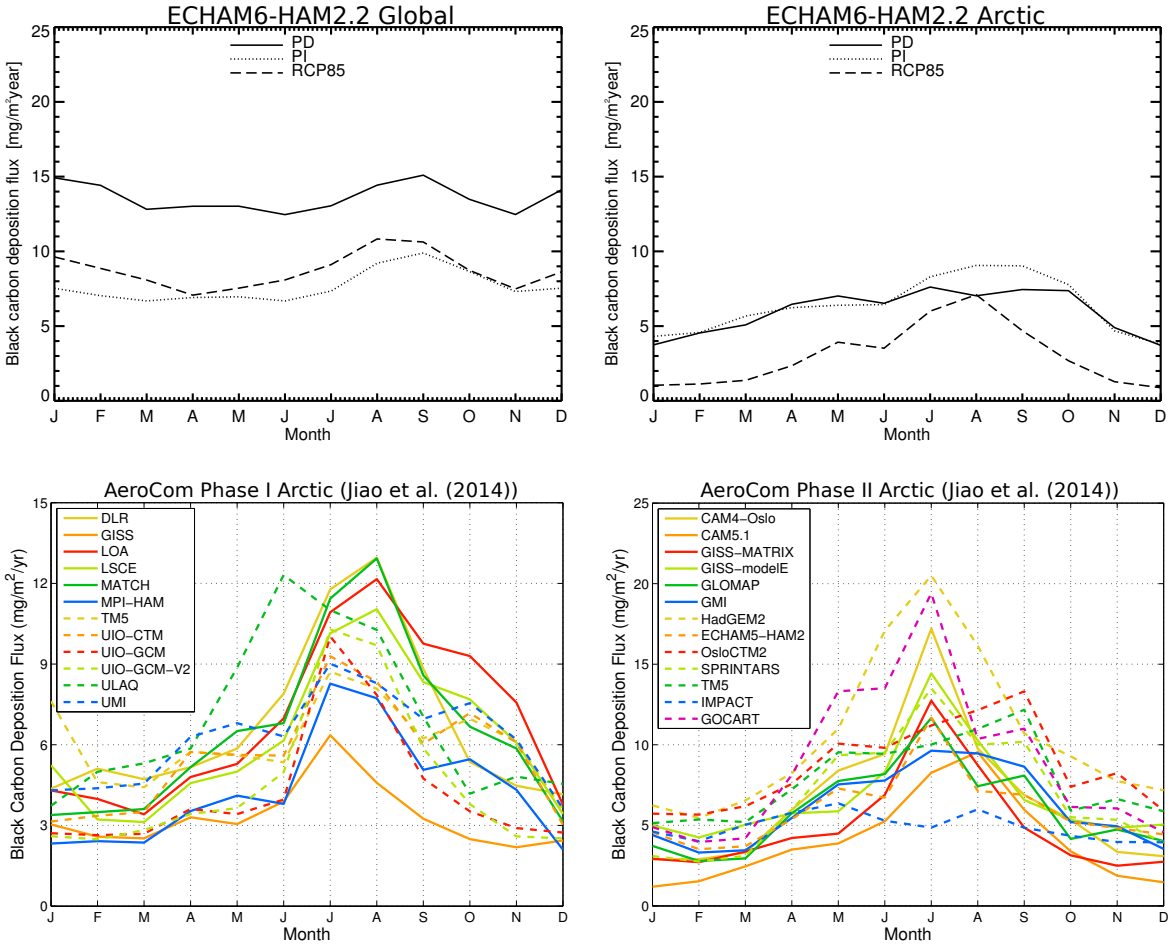

Figure 2.5: Top left: Global monthly mean BC aerosol deposition fluxes in mgm^{-2}year^{-1} averaged over ten simulation years for the PI (1880-1889), PD (2000-2009), and the projected RCP85 (2090-2099) simulation, respectively. Top right: Monthly mean BC aerosol deposition fluxes in mgm^{-2}year^{-1} for the Arctic (60°N-90°N) averaged over ten simulation years for the PI (1880-1889), PD (2000-2009), and projected RCP85 (2090-2099) simulation, respectively. Bottom: Seasonal cycle of BC aerosol deposition fluxes for the Arctic region (60°N-90°N) for phase I models (left) and phase II models (right) of the AeroCom project taken from Jiao et al. (2014). Note the different scale on the ordinate for the plot on the left.

PD simulation highest BC aerosol deposition fluxes are found in DJF (7.86 Tgyear^{-1}), and in SON for the PI simulation (4.40 Tgyear^{-1}). This is also shown in the seasonal cycle of the BC aerosol deposition fluxes in mgm^{-2}year^{-1} for the three different time periods PI, PD, and RCP85, as shown in the top panel in Figure 2.5 on the left: All simulations show a similar development of the BC aerosol deposition over the year with increasing BC aerosol deposition fluxes in the summer season peaking in September for the PI and PD simulation and in August for the RCP85 simulation. For the Arctic, highest BC aerosol deposition fluxes occur in JJA for all three simulations, but the seasonal cycle differs for the three time periods as shown in the top panel in Figure 2.5 on the right: The PI and the future RCP85 simulations show a clear peak in the BC aerosol deposition fluxes at the end of the summer season, whereas the PD simulation shows a more smooth deposition flux from spring to autumn. The PI and the RCP85 simulations peak in August, whereas the PD simulation peaks in July.

The seasonal cycles of the BC aerosol deposition fluxes of the phase I and phase II models used in the AeroCom comparison study by Jiao et al. (2014) for the Arctic are shown in the bottom panels of Figure 2.5, respectively. The present-day ECHAM6-HAM2.2 BC aerosol deposition fluxes in the Arctic (Figure 2.5, top (right)) show a similar behaviour in the seasonal cycle compared to the phase II models used in Jiao et al. (2014). The amount of the BC aerosols deposited in the Arctic as simulated with ECHAM6-HAM2.2 falls in the range of other models used in phase II of the AeroCom project.

2.3 Experimental design

This section summarizes the performed set of simulations to isolate the effect of the darkening of snow by the deposition of BC aerosols on land-based snowpack for pre-industrial, present-day and projected future conditions following the RCP8.5 scenario for the end of the 21st century. Here, BC aerosols emitted from all sources are taken into account.

To isolate the effect on climate caused by the deposition of BC aerosols on snow leading to a darkening of the snow albedo, ECHAM6 was used with the horizontal resolution T63 (1.875° x 1.875°) considering 47 vertical layers (spanning from the surface up to 0.01 hPa) and a time step of 10 minutes. The version of ECHAM6 used for the present study includes the implemented snow-albedo-scheme described in section 2.1.2. The snow albedo in ECHAM6 is determined following the BATS scheme (section 2.1.1). Climate conditions including sea surface temperatures (SSTs) as well as sea ice concentrations (SICs) are prescribed from CMIP5 simulations (Giorgetta et al., 2013) as boundary conditions. In addition, BC aerosol deposition fluxes from ECHAM6-HAM2 simulations resulting from the ACCMIP-setup described in section 2.2 are prescribed. A scheme of the model setup is shown in Figure 2.6. Each simulation was performed for 11 years, at which the first simulation year was treated as model spin up time, so that only the last ten years of each simulation were included in the analysis.

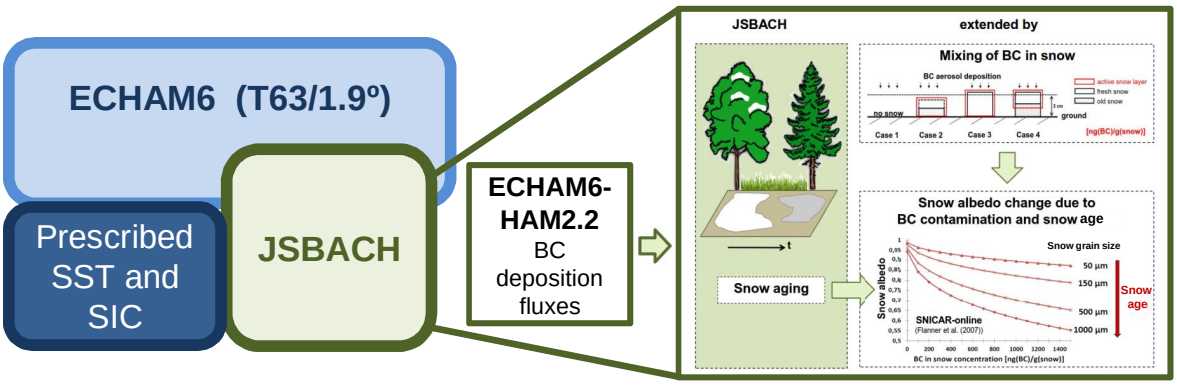

Figure 2.6: Scheme of the model setup used to isolate the climate effect of the deposition of BC aerosols on snow using ECHAM6 with prescribed BC aerosol deposition fluxes.

To estimate the effect of the deposition of BC aerosols on land-based snowpack on climate, the changes in the radiation balance are estimated in terms of the instantaneous radiative forcing as defined in the Fifth Assessment Report (AR5) of the Intergovernmental Panel on Climate Change (IPCC; Myhre et al., 2013b). Therefore, the radiative transfer scheme in ECHAM6 is run twice within one simulation, once with and once without snow albedo reductions resulting from the contamination of snow due to BC aerosols. Here, the differences in the radiative forcing are calculated from the differences including and excluding BC aerosol deposition fluxes within one simulation. Applying this model setup, the net flux change under fixed temperature conditions everywhere is obtained at the top of the atmosphere (TOA) as well as at the surface. A similar method was applied in other modelling studies (e.g. Goldenson et al., 2012). Assuming that the impact of the snow albedo reductions due to BC aerosol deposition on snow on the stratospheric temperatures is small, the in this way obtained instantaneous radiative forcing can be equated with the radiative forcing allowing for stratospheric temperatures to readjust.
Note here, while the radiation scheme is called twice, once with and once without snow albedo reductions, the physics of ECHAM are run with the albedo not taking BC concentrations in snow into account.

With the described model setup, the set of experiments summarized in Table 2.2 was performed. To evaluate the implemented snow-albedo-scheme, the PD simulation accounting for present-day climate as well as present-day BC aerosol deposition fluxes was performed. To assess in addition the effect of BC aerosol deposition on snow on climate for pre-industrial conditions, the PI simulation considering both pre-industrial climate and BC aerosol deposition fluxes was performed. The effect of the deposition of projected future BC aerosols on projected future snow cover is assessed by the RCP85 simulation applying projected future climate as well as future BC aerosol deposition fluxes following the RCP8.5 scenario. The RCP8.5 scenario is selected to estimate the effect of a warmer climate on the effect of the snow contamination by BC aerosols for projected future conditions, as the RCP8.5 scenario is the strongest projection in terms of climate conditions compared to other RCP scenarios. In

Table 2.2: Setup of the single ECHAM6 simulations to isolate the climate effect of BC contamination of snow. Here, the climate (sea surface temperatures and sea ice concentrations) and the BC aerosol deposition fluxes (ECHAM6-HAM2.2) are prescribed as boundary conditions representative for pre-industrial (PI), present-day (PD), and projected future conditions following the Representative Concentration Pathway 8.5 (RCP85) in different combinations. Each simulation covers ten years.

Experiment	**Climate**	**BC aerosol deposition**	**Time period**
PI	PI	PI	1880-1889
PD	PD	PD	2000-2009
RCP85	RCP8.5	RCP8.5	2090-2099
cPD_dRCP85	PD	RCP8.5	2000-2009
cRCP85_dPD	RCP8.5	PD	2090-2099

addition, decreasing BC aerosol emissions at the end of the 21st century are projected in this scenario.

To further disentangle the contribution of the climate and the BC aerosol deposition fluxes as well as the synergies between the processes on the changes in projected future instantaneous radiative forcing compared to present-day conditions, two additional experiments were performed to follow the factor separation technique by Stein and Alpert (1993). For the cPD_dRCP85 simulation present-day climate combined with projected future BC aerosol deposition fluxes following the RCP8.5 scenario were used, whereas the cRCP85_dPD simulation is based on projected future climate conditions following the RCP8.5 scenario and present-day climate conditions.

Chapter 3

Impact of present-day BC aerosol deposition on snow cover, BC concentrations in snow, albedo, and radiation

This chapter summarizes the simulated impact of present-day (PD, 2000-2009) BC aerosol deposition fluxes originating from anthropogenic as well as natural emission sources on land-based snowpack. The resulting BC concentrations in snow (section 3.2) cause snow albedo and total surface albedo reductions (section 3.3) and influence the radiation budget (section 3.4) which is described in the following. Section 3.1 begins with the evaluation of the present-day snow cover representation in ECHAM6, which is crucial for the accurate representation of BC concentrations in snow.

3.1 Present-day snow cover representation in ECHAM6

An accurate representation of the snow cover in climate models is crucial due to the ability of the snow cover to significantly enhance the surface albedo and thus impacting the climate (e.g. Vaughan et al., 2013). The impact of BC aerosols deposited on snow is also strongly controlled by the snow cover. Only when snow is present BC aerosol deposition fluxes will alter the surface albedo. Climate models thereby differ in their ability to reproduce present-day observed snow cover (e.g. Brutel-Vuilmet et al., 2013). Therefore, the climate impact of snow darkening caused by BC aerosol deposition on snow will differ in different climate models as a consequence of varying snow cover representations. To get an estimate on the representativeness of simulated snow cover in ECHAM6, the present-day simulation is compared to two satellite-based observational data sets (MODIS and IMS). The two data sets are introduced in section 3.1.1. Section 3.1.2 presents the comparison of simulated and observed snow cover. Note, that this comparison does not satisfy a full evaluation of the simulated snow cover in ECHAM6, as this would require a careful consideration of the uncertainties related to the satellite-based observational data sets, which is beyond the scope of the present study.

3.1.1 Observational data sets

To evaluate the model performance of ECHAM6 with respect to simulated present-day snow cover, two independent satellite-based data sets, MODIS and IMS, were used to partly account for the large uncertainty related to satellite based snow cover observations (e.g. Brown and Robinson, 2011). Both data sets are provided by the Integrated Climate Data Center (ICDC, http://icdc.zmaw.de). In the following, the snow cover data sets and their application in the comparison are described.

3.1.1.1 MODIS snow cover data set

The first data set used is the snow cover data set of the Moderate Resolution Image Spectroradiometer (MODIS). This data set contains global data of fractional monthly mean snow cover over land on a Climate Modeling Grid (CMG) consisting of 7200 column by 3600 row arrays with a 0.05° x 0.05° grid cell size. At the time of downloading the data set, data were available from March 2000 to December 2014. Data for the dates August 2000, June 2001, March 2002, and December 2003, however, are missing in the time series. The basis of the data set are global daily data on the same grid, which are obtained from global data on a 500 m grid resulting from an interpolation of the fractional snow cover which is derived from every single MODIS overpass. Here, the MODIS channels 4 (0.55 μm) and 6 (1.6 μm) are used for the calculation of the Normalized Difference Snow Index (NDSI) to obtain the fractional snow cover. Concerning the quality of the monthly data set, pixels where no snow cover is available as well as pixels where snow cover values are doubtful are identified and indicated. Here, clouds, missing daylight, open water, and an ambiguous classification are taken into account. A detailed description of the data set can be found in Hall et al. (2006) as well as on the website of the National Snow & Ice Data Center (NSIDC, http://nsidc.org). To compare the simulated snow cover fraction of ECHAM6 in a grid box to the MODIS snow cover, the MODIS data set was remapped to the T63 (1.875° x 1.875°) model resolution used in the present study. The MODIS data set does not contain snow cover in the northern high latitudes in the winter season due to missing sun light in this time period. To compare the simulated snow cover only in grid boxes where satellite-retrieved snow cover is available, a snow mask for each of the months November, December, January, and February, respectively, was generated. The simulated snow cover was only compared where the snow masks contain values in more than 9 times compared to the total number of 14 months for the 14 years analysed (2000-2014).

3.1.1.2 IMS snow cover data set

The second data set used is compiled by the Interactive Multisensor Snow and Ice Mapping System (IMS; Ramsay, 1998). This data set is unique as it is the only long-term snow cover data set which is manually created by the visual analysis of satellite analysts. Thus, the data set is independent from other data sets. The data set covers the Northern Hemisphere and is provided on a polar stereographic projection centred at 90°N. In the present study, the 24 km resolution with a grid size number of 1024 x 1024

is used. This resolution covers the longest time period for which the snow cover data are available on a daily time step (February 1997 until present). At the time of downloading the data set, the snow cover data were available from October 1998 to December 2014. The data set distinguishes whether a grid cell is covered by snow or not. In contrast to the MODIS data set no further fractional information about the snow and ice cover is given. The satellite analysts use the available satellite imagery originating from polar orbiting satellites as well as geostationary satellites which are complemented by passive microwave satellite data when e.g. daylight was missing or cloud cover existed. Further, additional information from persistence of the snow cover as well as ground weather observations are used. This system provides a quite reliable data set for many periods and regions (Armstrong and Brodzik, 2002). In addition, the IMS product is produced in near-real time so that it can be used as initialization fields for numerical weather prediction models. A detailed description of the data set can be found on the IMS website (http://nsidc.org/data/docs/noaa/g02156_ims_snow_ice_analysis/index.html) and in National Ice Center (2008).
For the comparison to the simulated snow cover the IMS data set was remapped from a polar stereographic grid to the Gaussian grid used in the current model version (T63, 1.875° x 1.875°) resolution. As only the occurrence of the snow cover is available, the daily data were aggregated to data covering the total time period or a respective season by summing up the grid boxes that are marked as snow covered divided by the number of days within the total time period or the respective season. The same was done for the ECHAM6 simulation taking only snow cover fractions into account which are larger than 1 %.

3.1.2 Simulated versus observed snow cover

Figure 3.1 shows on the left the differences in the snow cover from the MODIS data set compared to the simulated present-day snow cover. On the right, the differences in the time period grid boxes are covered by snow between the IMS data set and the present-day simulation are shown.
Compared to the MODIS data set, the model underestimates the snow cover in most regions, except in the region of Greenland and in some mountainous regions like the Tibetan Plateau and in Siberia where the simulated snow cover is overestimated. Compared to the IMS data set, the simulation underestimates the time the regions are snow covered for most regions, except mountainous regions around the Tibetan Plateau, Mongolia, Siberia as well as at the western coast of North America for which the model overestimates snow cover presence averaged over the time period.

More in detail, Figure 3.2 shows the snow cover differences for the two data sets for the different seasons compared to the simulated present-day snow cover. The comparison to both data sets shows an underestimation of the simulated snow cover especially in winter (DJF) and spring (MAM) for most southerly margins of seasonal snow cover between 30°N and 60°N where the snow cover is sparse and only occurs in the winter time. Other than the MODIS data set, the IMS data set points to an overestimation in the mountainous regions around the Tibetan Plateau of the snow cover duration in these seasons (DJF, MAM) as well as an even more pronounced overestimation

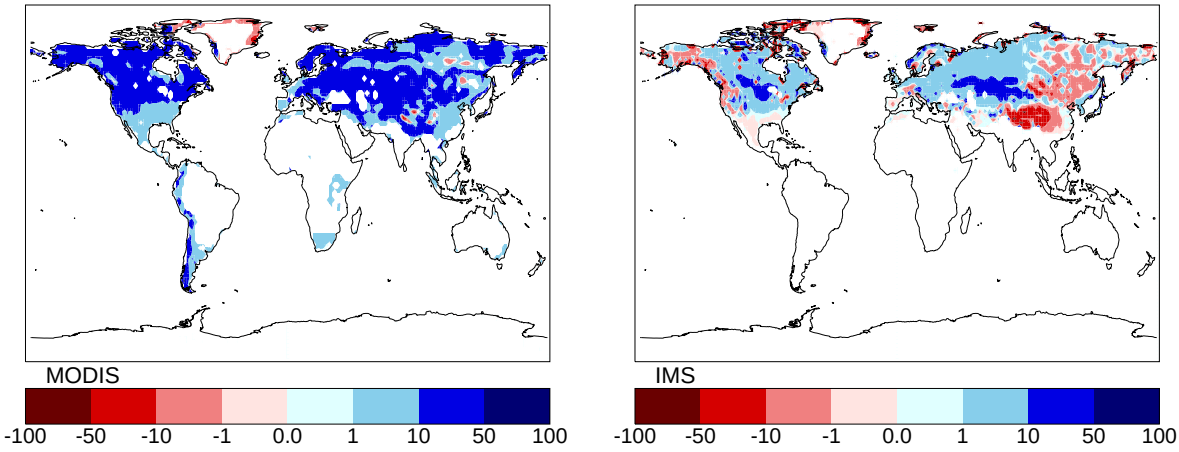

Figure 3.1: Differences in present-day observed and simulated snow cover. Left: MODIS snow cover fraction averaged over 2000-2014 minus simulated present-day snow cover averaged over 2000-2009. Missing snow cover fractions in the MODIS data in the winter time due to absent sunlight in the northern high latitudes are taken into account. Right: Differences in the percentage of the time the respective grid boxes are covered by snow in the IMS data set (1998-2014) minus present-day simulated snow cover (2000-2009). Here, only differences where both data sets contain snow cover are taken into account.

for the autumn season (SON) in almost all regions of the Northern Hemisphere. For SON, the MODIS data set also shows small-area patterns of overestimated snow cover around the Mongolian region. Both data sets indicate mostly an underestimation in the simulated snow cover in the summer season (JJA).

The comparison of the ECHAM6 simulation to satellite-based observational snow cover data sets is broadly consistent with former studies which compared simulated snow cover to observations. Brutel-Vuilmet et al. (2013), for example, analysed the land snow cover during boreal spring simulated by climate models as part of CMIP5 by a comparison to observations. Here, only the seasonal snow cover of ice-free land in the Northern Hemisphere is taken into account. Overall, the CMIP5 models reproduce the seasonal cycle of the snow cover rather accurate over the northern parts of the boreal regions. However, 50 % of the models show a tendency to simulate too frequent snow cover in spring in the southerly region at the margins of seasonal snow cover, whereas the remaining 50 % of the models simulate too scarce snow cover. Brutel-Vuilmet et al. (2013) also state a large overestimation of spring snow cover over the region Tibet, Mongolia and China. This is in line with the model behaviour of the current ECHAM6 model version and seems to be a general problem in climate models which might be a result from an underestimation of the warming of the boreal land surface at that time of the year (Brutel-Vuilmet et al., 2013).

The underestimation in simulated spring time snow cover for Northern Eurasia is in line with the study by Räisänen et al. (2014) in which the offset of the snow cover in spring over Northern Eurasia as simulated in ECHAM5 (version 5.4) is compared to observations in more detail. The study highlights that snow melts too early in northern Europe, in the western parts of northern Eurasia as well as

in the northern most regions like the Taymyr peninsula. They point out that the early snow melt relates to snow melt that occurs at too low temperatures, which is related to the treatment of the surface energy budget: As the surface temperature for snow-covered and snow-free areas in a grid box are not determined separately, the surface temperature can not rise above 0°C before all the snow in the grid box has disappeared. Thus, too much of the radiation is dissipated for the melting of snow instead of heating the air. Räisänen et al. (2014) also note that in ECHAM6 the snowmelt still occurs at too low temperatures as well based on the simulations performed in Stevens et al. (2013). This behaviour can also be seen in the comparison of the present-day simulated spring time snow cover in the present study compared to the two satellite-based snow cover data sets.

Underestimating the snow cover in the model might have an effect on the resulting effect of snow contamination due to BC aerosols on the radiation: More potentially snow covered regions in the spring season, when the highest amount of snow cover has accumulated over the winter season and the radiation is already stronger than in winter, might lead to a stronger effect on the radiation due to the deposition of BC aerosols on additional snow cover (e.g. Flanner et al., 2007). However, the IMS data set also shows a strong overestimation of the snow cover e.g. in autumn (SON), which might also lead to an overestimation of the effect on the radiation caused by the deposition of BC aerosols on snow in this particular season. Overall, however, a direct estimate of the effect of an under- or overestimated snow cover of the impact of snow darkening caused by the deposition of BC aerosols is difficult, as the BC concentration in snow depends non-linearly on the snowfall.

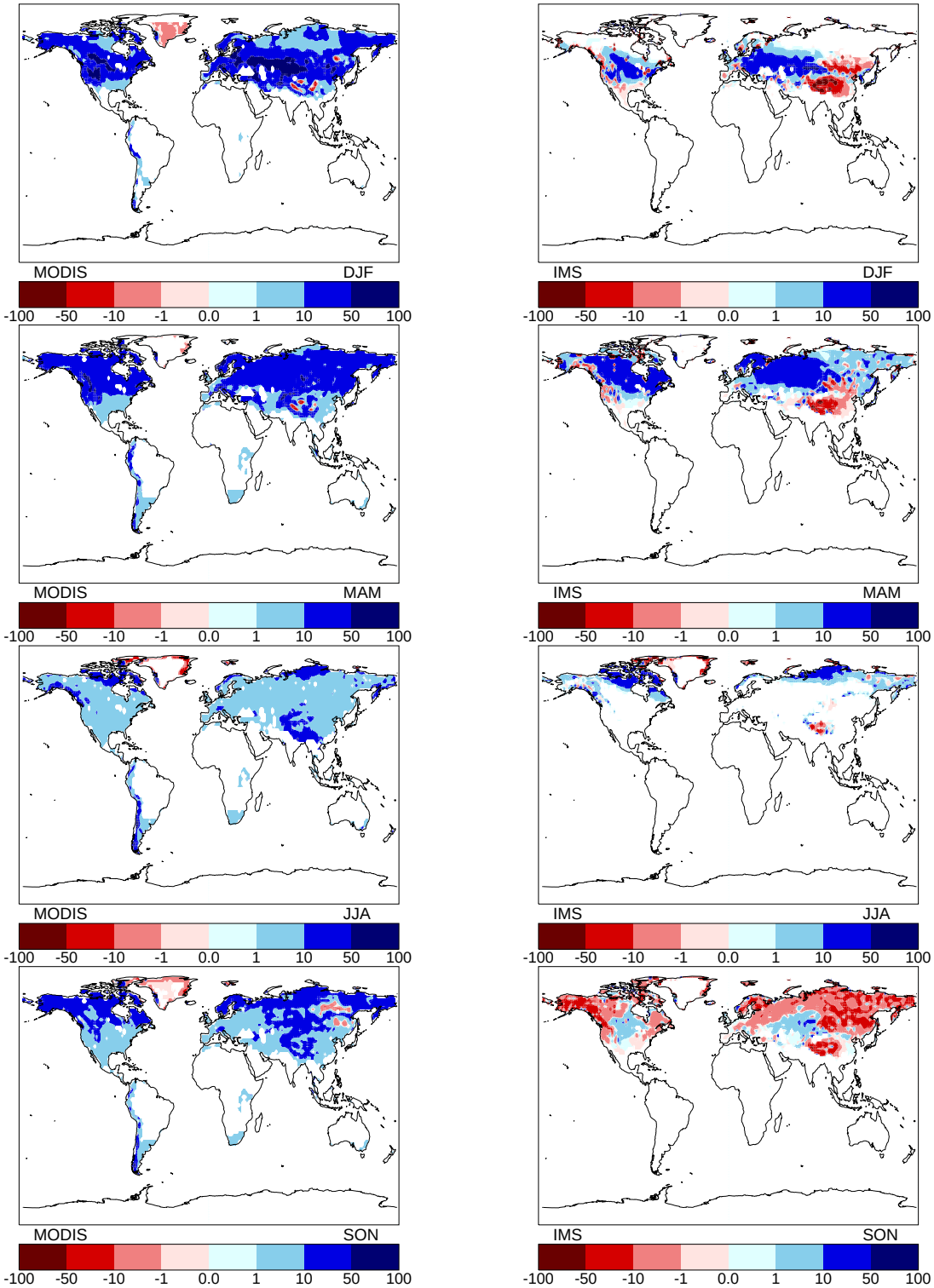

Figure 3.2: Differences in present-day observed and simulated snow cover for the different seasons (DJF, MAM, JJA, SON). Left: MODIS snow cover fraction averaged over 2000-2014 minus simulated present-day snow cover averaged over 2000-2009. Missing snow cover fractions in the winter time due to absent sunlight in the northern high latitudes are taken into account. Right: Differences in the percentage of the time the respective grid boxes are covered by snow in the IMS data set (1998-2014) minus present-day simulated snow cover (2000-2009). Here, only differences where both data sets contain snow cover are taken into account.

3.2 Measured and simulated BC concentrations in snow

To quantify the radiative effect of the deposition of BC aerosols on snow using a model requires the accurate representation of BC concentrations in snow. For the evaluation of the model performance of the implemented snow-albedo-scheme, present-day BC concentrations in snow as simulated in ECHAM6 are compared to BC concentrations in snow obtained from field studies. In addition, the simulated BC concentrations in snow are compared to other global modelling studies.

A comprehensive evaluation data set was collected to validate the simulated BC concentrations in snow covering different regions and time periods: The study by Ye et al. (2012) reports measured BC in snow content in the northern Xinjiang province in north-western China in January and February 2012 and the study by Wang et al. (2013) reports BC concentrations in snow from snow samples collected in six provinces across northern China in January and February 2010. In the comprehensive study by Doherty et al. (2010), Arctic snow is surveyed to extend and update the survey of Clarke and Noone (1985). Snow samples were collected in 1998 and 2005-2009 mainly in the months from March to May with the exception that snow samples on the Greenland Ice Sheet were collected in the summer months. The study by Doherty et al. (2010) obtains a better spatial resolution compared to Clarke and Noone (1985) covering widespread areas in the remote regions of Alaska, Canada, Greenland, Svalbard, Norway, Russia, and the Arctic Ocean. In Flanner et al. (2007) several studies carried out in the 1980s and the 1990s are summarized covering measurement sites e.g. in the Arctic, Greenland, and the Antarctic. The measurement sites are shown in Figure 3.3. The varying measurement techniques and the respective uncertainties of the estimated BC concentrations in snow are discussed in the particular studies. The four selected studies cover regions with high amounts of BC in snow due to the vicinity of the measurement sites to industrialized areas, but also remote regions with typically low BC in snow content are covered, which allows in addition an evaluation of the long-range BC aerosol transport of the ECHAM6 model. The simulated BC concentrations in snow are compared to the BC in snow contents measured in surface snow from all studies.

Simulated present-day values for the BC concentrations in snow are calculated corresponding to the particular month of the year when the measurements were performed. The BC concentrations in snow are averaged for the grid box covering the sample site over ten simulation years (2000-2009). Figure 3.4 in the top panel shows, that the model captures the different orders of magnitude of the measured BC concentrations in snow. Although, in some regions the model underestimates as well as overestimates measured BC concentration in snow. Particularly the simulated BC concentrations in snow located in the surroundings of strong anthropogenic emission sources, e.g. for the measurement sites in China (Wang et al., 2013; Ye et al., 2012) are in good agreement with the measurements. For other regions, differences in simulated compared to measured BC concentrations in snow can reach up to two orders of magnitude. Figure

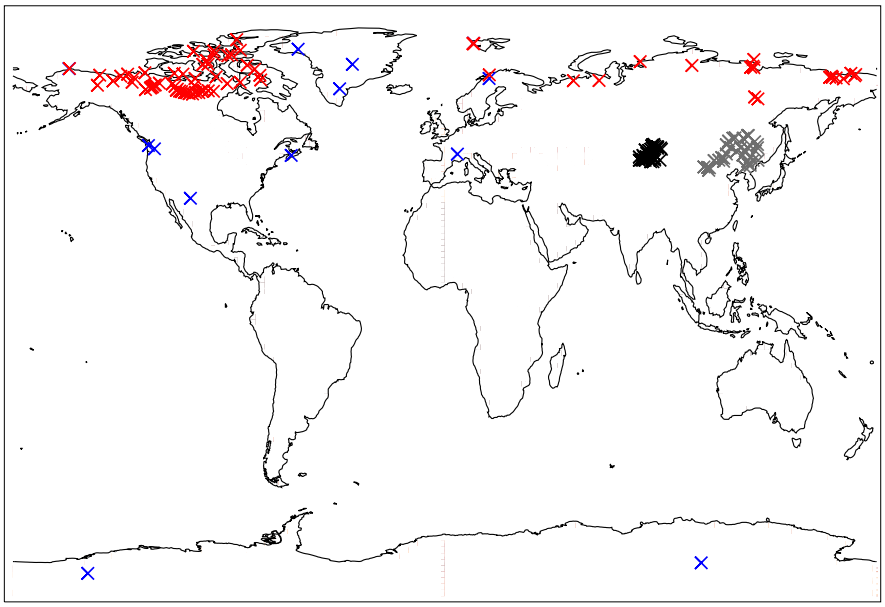

Figure 3.3: Measurement locations of BC concentrations in snow of the evaluation data set used in the present study. Data from the different studies are colour coded: Ye et al. (2012) in black, Wang et al. (2013) in grey, Doherty et al. (2010) in red, Flanner et al. (2007) in blue.

3.4 in the bottom panel shows the same simulated and measured BC concentrations in snow as shown in the top panel now plotted against the respective latitudes. While there is in general a good agreement between the model and the measurements for the latitudes between 35° and 70°N, the model underestimates BC concentrations in snow for latitudes north of 70°N. This underestimation can be attributed to the too weak long-range transport of BC aerosols into the northern high-latitudes, which has been discussed in section 2.2.

The measurement evaluation data set of BC concentrations in snow compiled for this study comprises an adequate widespread geographically distribution to evaluate the model. Overall, the simulated BC concentrations in snow show a reasonable agreement with the measurements given that localized and time specific measurements are compared to coarse scale monthly averaged model data. The spatial as well as the temporal resolution of the measurements is not suitable to investigate the BC concentrations in snow at all times of the year. The BC aerosol transport has a high interannual variability which is not captured by a comparison to climatological mean model output. In addition, the question remains whether the analysed samples of BC concentrations in snow are representative for a broad region.

Simulated BC concentrations in snow were also compared to other modelling studies. Flanner et al. (2007) applied the standard version of the snow radiative SNICAR model (Flanner and Zender, 2005) coupled to the National Center for Atmospheric Research (NCAR) Community Atmosphere Model, version 3 (CAM3) (e.g. Collins et al., 2004). The BC concentrations in snow reported by Flanner et al. (2007) and BC concentrations in snow simulated with the implemented snow-albedo-scheme in ECHAM6 are shown for comparison in Figure 3.5. In the present study, only BC

concentrations in snow where the snow layer exceeds 1 mm are considered. In general, the simulated BC concentrations in snow from the snow-albedo-scheme are in good agreement with the results presented by Flanner et al. (2007). High BC concentration in snow patterns are found in China, eastern North America, and Europe in both model simulations. However, the simulated BC concentrations in snow from the snow-albedo-scheme in ECHAM6 are lower in the remote regions of the Northern Hemisphere, especially over Greenland. Note that the BC aerosol deposition fluxes

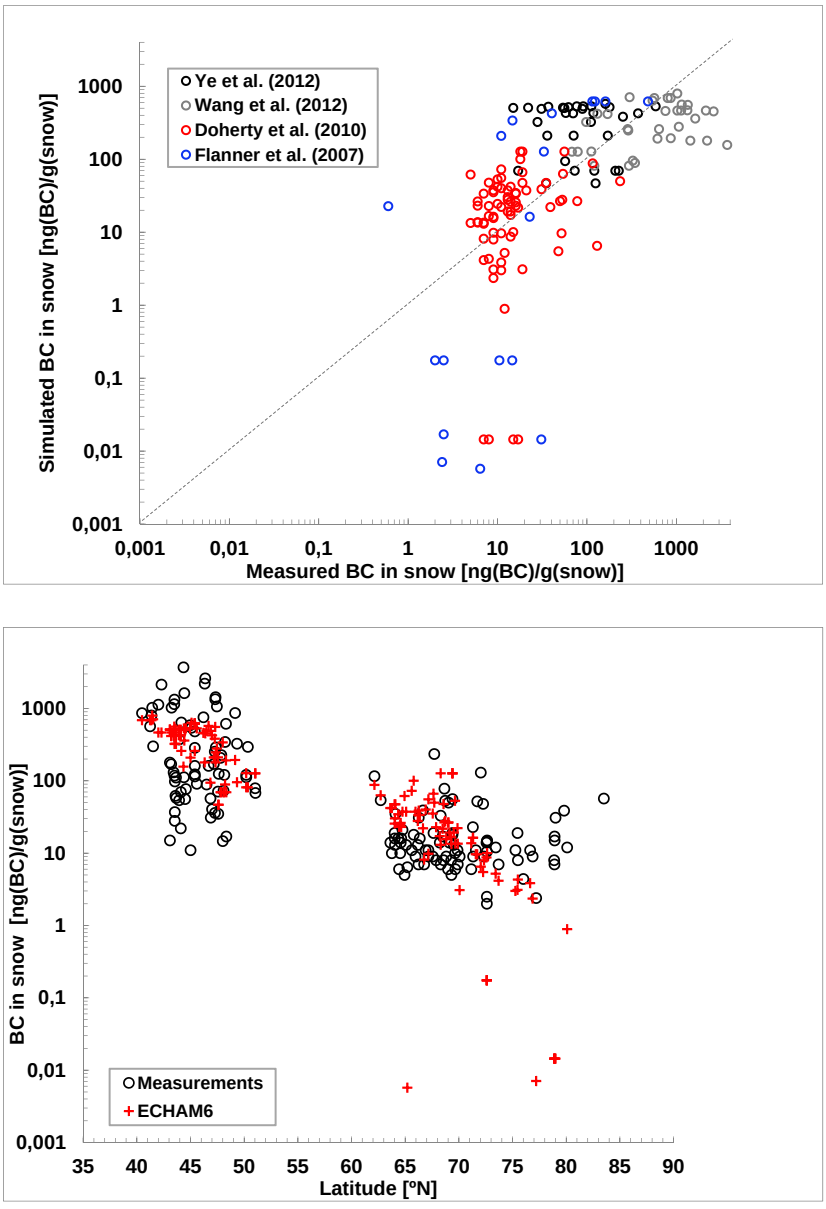

Figure 3.4: Simulated compared to measured BC concentrations in snow. Top: Present-day simulated BC concentrations in snow (ECHAM6) compared to measured BC concentrations in snow [ng(BC)g(snow)$^{-1}$] taken from the studies Ye et al. (2012) in black, Wang et al. (2013) in grey, Doherty et al. (2010) in red, and Flanner et al. (2007) in blue. Right: Simulated BC concentrations in snow compared to the same measurements as shown on the left but plotted against the latitudes.

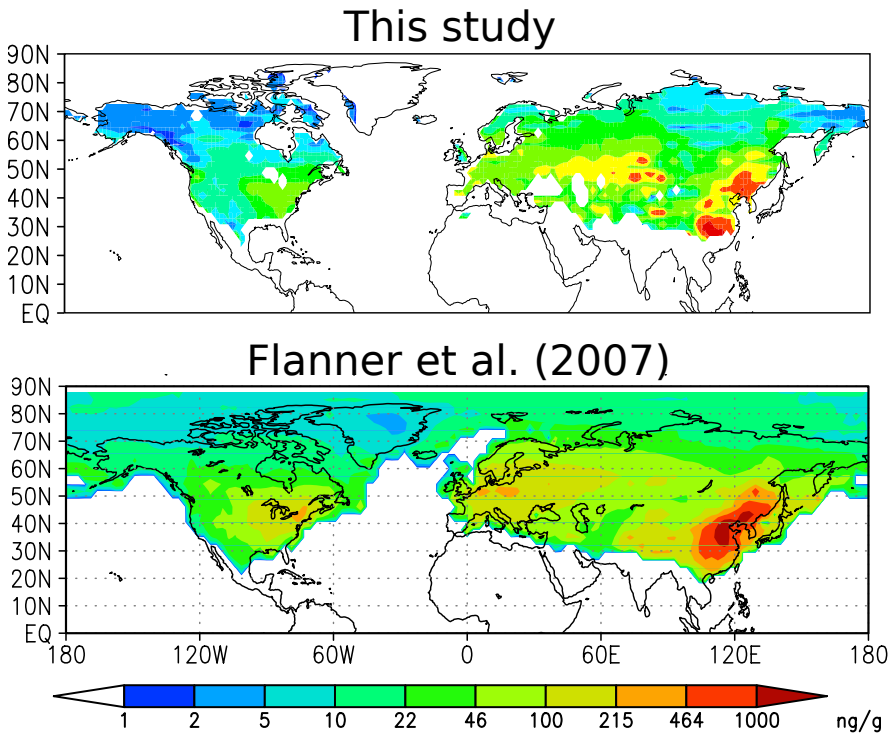

Figure 3.5: Present-day simulated BC concentrations in snow in ng(BC)g(snow)$^{-1}$. The top panel shows BC concentrations in snow as simulated with the snow-albedo-scheme in ECHAM6 averaged over ten simulation years (2000-2009) for snow depths exceeding 1 mm. The bottom panel shows simulated BC concentrations in snow taken from Flanner et al. (2007).

for the region of interest (north of 30°N) are about 20 % higher (3.5 compared to 2.8 Tgyear^{-1}) in Flanner et al. (2007) than the BC aerosol deposition fluxes used in the present study. The difference results from the fact that Flanner et al. (2007) focus on the year 1998 with relatively strong BC aerosol emissions related to fires.

In the study by Jiao et al. (2014) the spread in BC concentrations in snow simulated by the offline land and sea ice components of the Community Earth System Model (CESM) is analysed when prescribing 25 different BC aerosol deposition fields. The BC aerosol deposition fields originate from different state-of-the-art aerosol-climate models contributing to the two phases of the Aerosol Comparisons between Observations and Models (AeroCom) project. The resulting simulated BC concentrations in snow are compared to measured concentrations from the extensive field campaign by Doherty et al. (2010) which are also part of the evaluation data set applied in the present study. The study by Jiao et al. (2014) reports correlation coefficients between simulated and observed BC concentrations in snow, mean BC concentrations in snow for the different models, as well as biases between simulated and observed BC concentrations in snow for two scenarios of meltwater scavenging. The inefficient meltwater scavenging scenario applies scavenging coefficients of 0.2 and 0.03 for hydrophilic and hydrophobic BC aerosols, respectively, whereas the efficient meltwater scavenging scenario applies the factor 1.0 for both BC aerosol species. Here, only the values resulting from the inefficient meltwater scavenging are used for

the comparison as this setup corresponds to the values used in the present study (see section 2.1.2.1). The mean bias of the BC concentrations in snow for the AeroCom phase I models is -4.4 ng(BC)g(snow)$^{-1}$ ranging from -13.2 to 10.7 ng(BC)g(snow)$^{-1}$. For the phase II models the mean bias amounts to 4.1 ng(BC)g(snow)$^{-1}$ with a range from -13.0 to 21.4 ng(BC)g(snow)$^{-1}$. According to Jiao et al. (2014), the spread in the model-measurement biases reflects the different aerosol transport and removal processes and thus the long-range transport into the high latitude regions among the models. The mean biases of the AeroCom models for the two phases, former ECHAM-HAM model versions that were part of the intercomparison study by Jiao et al. (2014), and the current implementation in ECHAM6 used with prescribed ECHAM6-HAM2.2 BC aerosol deposition fields as used in the present study are summarized in Table 3.1. The present study can be best compared to the results of the AeroCom phase II models, because most of the models applied according to Myhre et al. (2013a) the ACCMIP (Lamarque et al., 2010) emission inventory similar to this study. The bias of 4.6 ng(BC)g(snow)$^{-1}$ of the current implementation in ECHAM6 is comparable to the mean bias of the AeroCom phase II models of 4.1 ng(BC)g(snow)$^{-1}$. The mean observed BC concentrations in snow as used for the bias calculation in Jiao et al. (2014) is 19.2 ng(BC)g(snow)$^{-1}$. Thus, this mean bias of 4.6 ng(BC)g(snow)$^{-1}$ corresponds to an overestimation of mean BC concentrations in snow of about 20 %. Jiao et al. (2014) reports a low correlation coefficient of $<$ 0.3 between simulated and measured BC concentrations in snow for all models. For the present ECHAM6 study the correlation coefficient is low as well (0.22). Overall, the comparison of the present ECHAM6 simulation to the study of Jiao et al. (2014) shows that the results presented here fall in the range of other model estimates.

Table 3.1: Comparison of BC concentrations in snow between models and measurements (Doherty et al., 2010) as reported in Jiao et al. (2014). Biases are the differences between the model mean minus the mean of the measurements. The correlation coefficients reflect the correlation between simulated values and measurements (Doherty et al., 2010). Here, the mean of all models as well as the values for previous ECHAM-HAM model versions as reported in Jiao et al. (2014) are compared to the values obtained from the present study.

Study		**Model**	**Correlation coefficient**	**Bias [ng(BC)g(snow)$^{-1}$]**
Jiao et al. (2014)	Phase I	Model mean	-	-4.4
		MPI-HAM	0.22	-13.2
	Phase II	Model mean	-	4.1
		ECHAM5-HAM2	0.18	-4.9
This study		ECHAM6	0.22	4.6

3.3 Albedo reductions caused by BC aerosol deposition on snow

The snow albedo reductions as well as total surface albedo reductions simulated with the current implemented snow-albedo-scheme in ECHAM6 caused by the BC contamination of snow for the present-day simulation (PD, 2000-2009) are described in the following.

Snow albedo reductions averaged over ten simulation years for the PD simulation are shown in the top panel of Figure 3.6. In general, the albedo reductions follow the patterns of the BC concentrations in snow shown in the top panel in Figure 3.5: High snow albedo reductions occur in regions with high BC concentrations in snow e.g. close to the strong anthropogenic BC aerosol emission sources like in China and eastern North America. In addition, also high snow albedo reductions are found in the Antarctic. Maximum snow albedo reductions reach a value of -0.17 with a mean snow albedo reduction of about -0.018 for the present-day period. The snow albedo reductions for the seasons DJF, MAM, JJA, SON are also shown in Figure 3.6. Here, the strongest snow albedo reductions for the different seasons are found in DJF with a mean reduction in the snow albedo of -0.019. Similar snow albedo reductions are found for the autumn season SON (-0.017). In spring (MAM), the strongest snow albedo reductions are found in more southerly regions at the margins of the seasonal snow cover of the Northern Hemisphere where the snow cover is sparse and only occurs in winter time. Locally, the smallest snow albedo reductions occur in the summer season (JJA). Maximum snow albedo reductions range from -0.078 for the summer season JJA up to -0.23 for SON.

Table 3.2 summarizes snow albedo reductions and averaged BC concentrations in snow for different BC concentration in snow intervals for the PD simulation. Here, averages over ten simulation years for snow depths in excess of 1 mm are shown. The lowest BC concentration in snow interval covering 0-10 ng(BC)g(snow)$^{-1}$ shows

Table 3.2: Global BC concentrations in snow ng(BC)g(snow)$^{-1}$ and snow albedo changes[/] resulting from the implemented snow-albedo-scheme averaged over ten simulation years for specific BC concentration in snow intervals. Shown are the averages for the PD-simulation.

BC concentration in snow interval [ng(BC)g(snow)$^{-1}$]	**Snow albedo change [/]**	**Average BC concentration in snow [ng(BC)g(snow)$^{-1}$]**
0 – 10	-0.0012871	2.7236
10 – 50	-0.011978	24.435
50 – 100	-0.035892	68.653
100 – 500	-0.071941	162.99
500 – 1000	-0.16632	628.50
1000 – 1500	-0.22622	1184.9
Global mean	-0.017617	44.98

average BC concentrations in snow of about 2.7 ng(BC)g(snow)$^{-1}$ leading to averaged snow albedo reductions of about -0.0013. An average snow albedo reduction of -0.23 is induced by an average BC concentration in snow of 1184.9 ng(BC)g(snow)$^{-1}$ resulting from the 1000-1500 ng(BC)g(snow)$^{-1}$ BC concentration in snow interval. The global

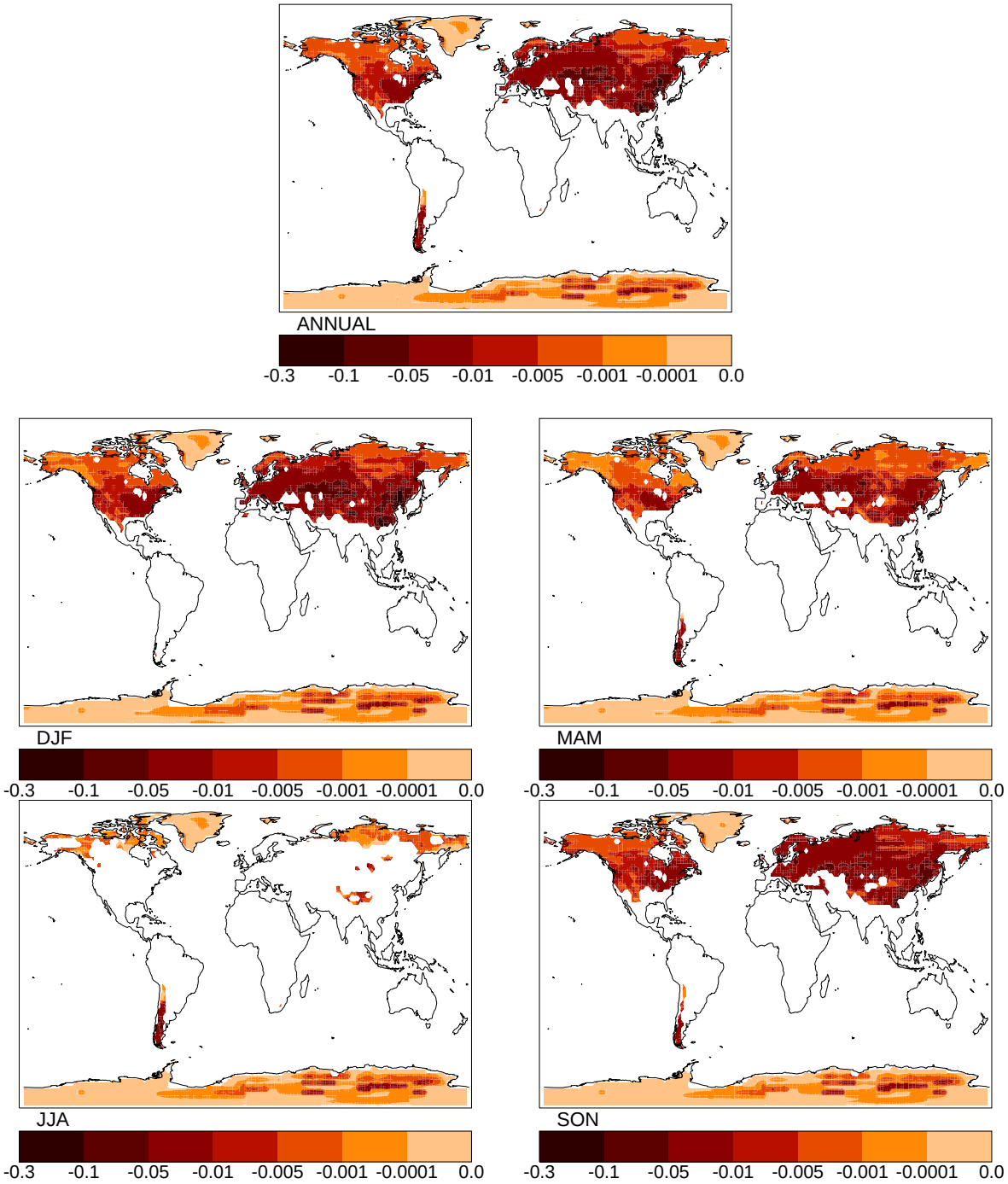

Figure 3.6: Present-day snow albedo changes [/] resulting from the implemented snow-albedo-scheme in ECHAM6. Albedo values are averaged over ten simulation years. The top panel shows the annual average, whereas the other panels show the averages over the different seasons DJF, MAM, JJA, and SON.

mean BC concentration in snow of 44.98 ng(BC)g(snow)$^{-1}$ leads to an average snow albedo reduction of about -0.018. These snow albedo reductions are in line with other modelling and measurement studies: Flanner et al. (2007) report a simulated albedo reduction for BC concentrations in snow in excess of 1000 ng(BC)g(snow)$^{-1}$ of more than -0.13 and for annual mean BC concentrations in snow exceeding 100 ng(BC)g(snow)$^{-1}$ a snow albedo reduction of more than -0.03. Conway et al. (1996) conducted field experiments measuring albedo values of snow surfaces treated with known amounts of aerosols like ash and soot as well as albedo values of untreated natural snow under the same meteorological conditions. With this experimental setup the long-term reduction of the snow albedo conditioned by the particle contamination is assessed. Here, the residual BC concentrations of about 500 ng(BC)g(snow)$^{-1}$ remaining on the surface of the snowpack cause snow albedo reductions of about -0.12 compared to natural snow after several weeks.

The total surface albedo α in ECHAM6 consists of four albedos: the albedo of surface covered by green leaves α_{leaf}, the albedo of snow covered soil α_{snow}, the albedo of snow covered forest canopy $\alpha_{\text{snow,c}}$, and the albedo of other soils α_{soil}. The previously described snow albedo reductions $\Delta\alpha_{\text{snow}}$ resulting from the implemented snow-albedo-scheme affect only the albedo of snow covered soil α_{snow} in ECHAM6. The influence of the snow albedo reductions on the total surface albedo is illustrated in Figure 2.1. As the snow albedo reductions only affect a part of the total surface albedo smaller total surface albedo reductions compared to the snow albedo reductions are expected which is confirmed in Figure 3.7. Here, zonally averaged snow albedo as well as total surface albedo reductions for the different latitudes (-90°S-90°N) are shown, averaged over ten simulation years only where snow is present. On average, the total surface albedo is reduced by -0.00039. High total surface albedo reductions

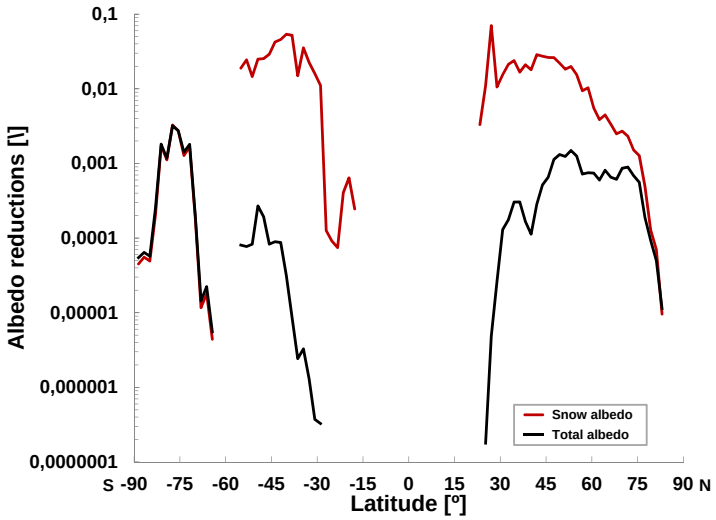

Figure 3.7: Present-day albedo reductions [/] resulting from the implemented snow-albedo-scheme in ECHAM6 zonally averaged for the different latitudes. Albedo values are averaged over ten simulation years. The snow albedo reductions in red result from snow depths exceeding 1 mm. The total surface albedo reductions in black are significant on a 95 % confidence interval based on a Student t-test.

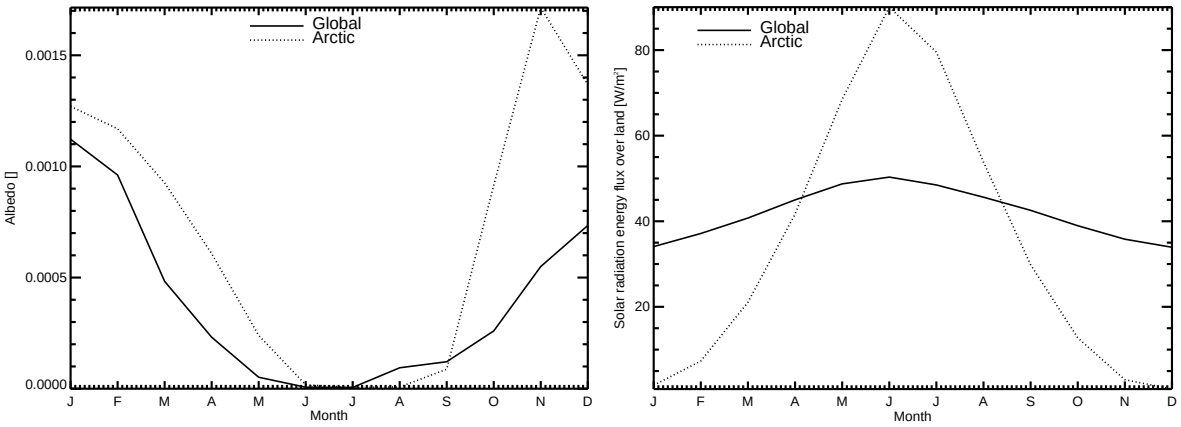

Figure 3.8: Present-day monthly mean differences in the total surface albedo [/] reductions between with and without BC aerosol deposition on snow and solar energy flux over land [Wm^{-2}] as simulated in ECHAM6. Left: Monthly mean differences in the total surface albedo between with and without BC aerosol deposition on snow averaged over ten simulation years globally as well as for the Arctic region (60°N - 90°N). Right: Monthly mean solar energy flux over land [Wm^{-2}] averaged over ten simulation years under present-day conditions, globally as well as for the Arctic (60°N-90°N).

are found in regions of the Northern Hemisphere which are closely located to the strong anthropogenic BC emission sources and in mountainous regions (30°N-70°N) as well as in the Antarctic (-90°S to -60°S). In the high latitudes, where the snow cover persists over a long time period throughout the year, the snow albedo reduction has a large influence on the total surface albedo reductions (e.g. north of 70°N). In regions where the snow cover occurs only in wintertime, the effect of the snow albedo reductions on the total surface albedo reductions is less, even though the snow albedo reductions are larger in those regions due to the vicinity of the strong anthropogenic BC emission sources (e.g. 25°N-30°N). In general, the total surface albedo reductions simulated with the current implemented snow-albedo-scheme in ECHAM6 are very small.

Monthly mean differences in the total surface albedo caused by the contamination of snow by BC aerosols are shown in Figure 3.8 on the left, globally as well as for the Arctic (60°N - 90°N). Increasing global total surface albedo reductions are found from August to a maximum in January on a global scale, followed by a decrease until June. Minimum total surface albedo reductions are found in June and July. Generally, the total surface albedo reductions are larger in the Arctic, compared to the global scale. Here, the total surface albedo reductions increase from August to a peak in November, followed by a decline until June. In June and July the minimum total surface albedo reductions are found in the Arctic region as well. In addition to the BC concentrations in snow the solar incoming radiation plays a key role regarding the strength of the effect of BC aerosol deposition on snow as well. The solar energy flux over land globally as well as for the Arctic region averaged over ten simulation years is shown in Figure 3.8 on the right. Even if the largest differences in the total surface albedo in the Arctic occur in November, the effect on the radiation balance in the autumn season (SON)

is supposed to be smaller compared to the spring season, since the incoming solar radiation over land is small due to the absence of sunlight at that time of the year in the Arctic.

3.4 Instantaneous radiative forcing resulting from BC aerosol deposition on snow

Finally, the effect of the present-day deposition of BC aerosols on land-based snow on the radiation balance is assessed. For this, the instantaneous radiative forcing within the performed present-day simulation (PD, 2000-2009) is determined as described in the following.

The effect of present-day BC aerosol deposition on land-based snowpack on the radiation is investigated in terms of instantaneous radiative forcing as defined in the Fifth Assessment Report (AR5) of the Intergovernmental Panel on Climate Change (IPCC; Myhre et al., 2013b). For this purpose, the radiative transfer scheme in ECHAM6 is run twice within one simulation, once with and once without snow albedo reductions resulting from the contamination of snow due to the deposition of BC aerosols. With this setup, the change in the net flux, under fixed temperature conditions everywhere, at the top of the atmosphere and at the surface is derived. A similar method has also been applied in other modelling studies, e.g. Goldenson et al. (2012). Determining the instantaneous radiative forcing in this way allows to put the instantaneous radiative forcing on a par with the radiative forcing allowing for stratospheric temperatures to adjust since the impact of the snow albedo reductions due to the deposition of BC aerosols on the stratospheric temperatures is projected to be small.

Locally, the effect of the deposition of BC aerosols on snow is strong. Figure 3.9 shows global maps of the mean present-day TOA instantaneous radiative forcing averaged over ten simulation years for the total time period in the top panel as well as for the different seasons DJF, MAM, JJA, and SON, respectively. Here, radiative forcing values in excess of 1 Wm^{-2} are found e.g. in the regions which are close to the strong anthropogenic BC aerosol emission sources like in China or mountainous regions like the Tibetan Plateau. A strong signal can also be found in eastern North America and in some regions in the Antarctic as well as on Greenland. Regarding the different seasons, the strongest signal is found in the mid-latitudes and the Antarctic in the winter season DJF. In the northern high latitudes the radiative forcing is most pronounced in spring (MAM) when most of the region is still covered by snow and in addition more sunlight is available compared to the winter season. In the summer season JJA a radiative forcing signal is only found in areas covered permanently with snow throughout the year like in Greenland or the Antarctic. In autumn (SON) the strongest signals can be found in mid-latitude regions.

The instantaneous radiative forcing caused by the deposition of BC aerosols on

snow has a large impact on a local scale. However, the instantaneous radiative forcing globally is comparatively small. The global as well as Arctic (60°N-90°N)

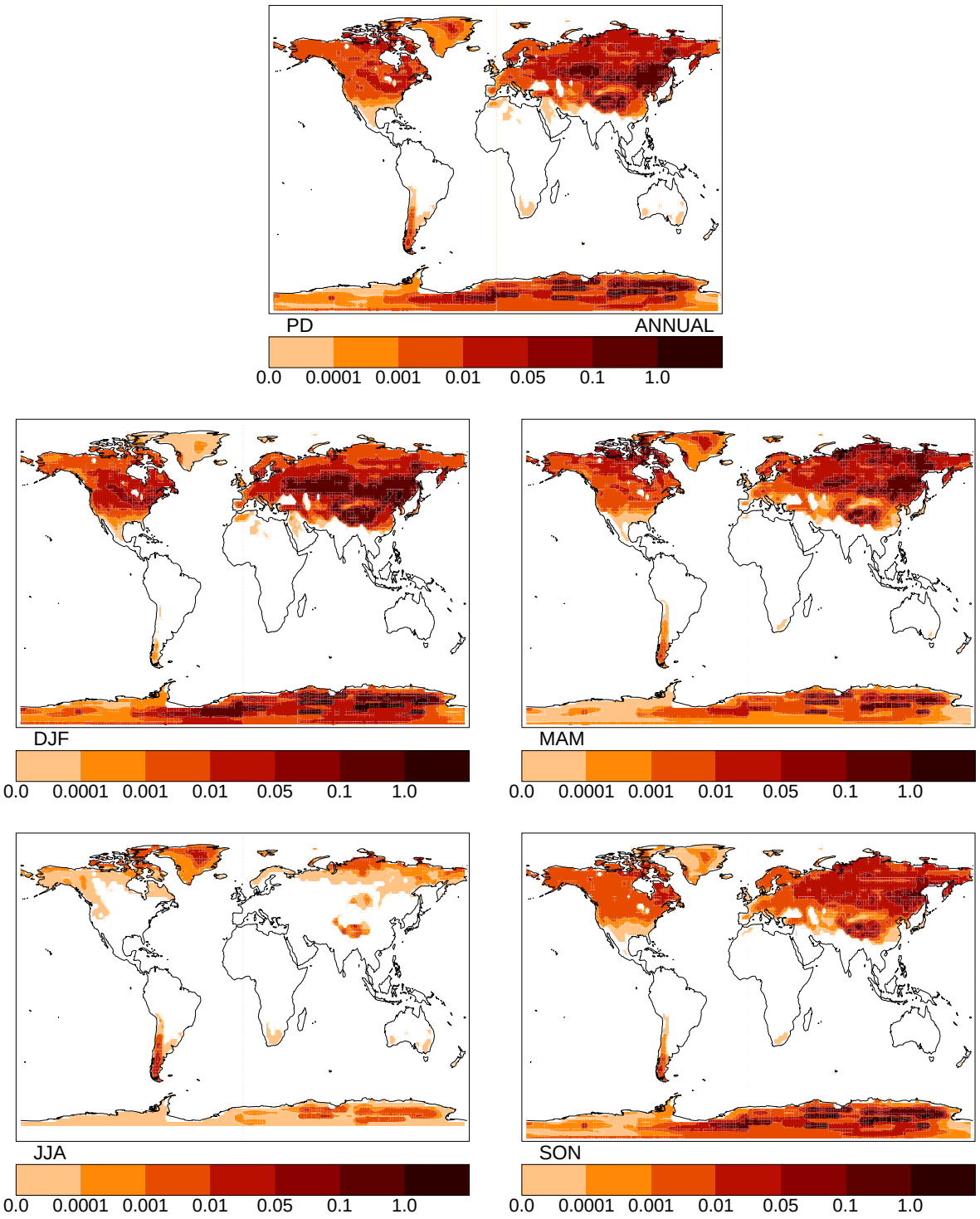

Figure 3.9: Instantaneous radiative forcing in Wm^{-2} for the present-day period (2000-2009) averaged over ten simulation years for total-sky conditions at TOA. The top panel shows the annual average, whereas the other panels show the average over the different seasons DJF, MAM, JJA, and SON, respectively.

instantaneous radiative forcing for the top of the atmosphere (TOA) and the surface (SUR) under total-sky conditions averaged over ten simulation years for the performed PD simulation is summarized in Table 3.3. Here, averages over the total time period (ANNUAL) as well as for the different seasons (DJF, MAM, JJA, SON, respectively) are shown. The instantaneous radiative forcing for the different seasons is estimated for TOA. $\text{ANNUAL}_{\text{snow}}$ represents averages only over the land-based snowpack.

On a global scale, the present-day instantaneous radiative forcing amounts to about 7 mWm^{-2}, showing little differences between the TOA and the SUR instantaneous radiative forcing (6.69 compared to 7.00 mWm^{-2}). Regarding the different seasons, the strongest forcing is found in the winter time (DJF) accounting for about 16.90 mWm^{-2}. In contrast, the lowest forcing occurs in the summer season (JJA) with about 0.12 mWm^{-2}. Averaging only over the land-based snowpack results in an about a factor of 16 stronger instantaneous radiative forcing of about 110 mWm^{-2} compared to the global instantaneous radiative forcing.

Restricting the region to the Arctic, a stronger radiative forcing compared to the global scale due to an increase in the ratio of areas covered by snow compared to areas where snow is absent is expected. This is confirmed for the averages of the instantaneous radiative forcing leading to a about 30 % higher instantaneous radiative forcing of about 9.25 compared to 6.69 mWm^{-2}. Regarding the different seasons, the strongest instantaneous radiative forcing caused by the deposition of BC aerosols on snow is found in the spring season MAM with about 23.88 mWm^{-2} for the PD simulation. In MAM the snow cover has accumulated to the highest amount over the snow season and more sunlight is available compared e.g. to the winter season DJF. In addition, higher BC aerosol deposition fluxes are available in the Arctic region in MAM compared to DJF (0.21 compared to 0.15 Tgyear^{-1}). The minimum instantaneous radiative forcing occurs in the summer season (JJA) showing a value of about 0.66 mWm^{-2}. Averaging only over the land-based Arctic snowpack over the

Table 3.3: Global and Arctic (60°N-90°N) present-day instantaneous radiative forcing and standard deviations in mWm^{-2} for total sky conditions resulting from the deposition of BC on land-based snow, averaged over ten simulation years (PD, 2000-2009). Shown are annual (ANNUAL) averages for the surface (SUR) as well as for the top of the atmosphere (TOA). DJF, MAM, JJA, and SON values are averages over the respective seasons for TOA. $\text{ANNUAL}_{\text{snow}}$ shows annual averages over the land-based snowpack.

RF [mWm^{-2}]	**Global**	**Arctic**
ANNUAL (SUR)	7.00 ± 3.25	9.76 ± 1.86
ANNUAL (TOA)	6.69 ± 3.14	9.25 ± 1.76
DJF	16.90 ± 9.16	5.52 ± 4.92
MAM	5.25 ± 4.45	23.88 ± 8.18
JJA	0.12 ± 0.09	0.66 ± 0.87
SON	4.68 ± 5.21	6.82 ± 3.82
$\text{ANNUAL}_{\text{snow}}$ (SUR)	110.05 ± 36.62	43.84 ± 7.73
$\text{ANNUAL}_{\text{snow}}$ (TOA)	105.96 ± 35.35	41.97 ± 7.37

total time period reaches a value of the instantaneous radiative forcing of about 40 mWm^{-2} which is about 60 % lower compared to the global scale (about 110 mWm^{-2}). This is in line with the simulated total surface albedo reductions as shown in section 3.3. The total surface albedo reductions show a pronounced poleward decrease from about 70°N given that the large anthropogenic BC aerosol emission sources are located southerly of the Arctic region. Thus, the effect on the radiation in the Arctic snowpack is expected to be lower compared to the snowpack located in the mid-latitudes.

The IPCC AR5 summarizes global modelling studies quantifying present-day radiative forcing resulting from snow contaminated with BC aerosols leading to a value of about 0.04 Wm^{-2}. Here, the spread in the radiative forcing in the considered studies ranges from 0.01 to 0.08 Wm^{-2} (Boucher et al., 2013). These studies differ as e.g. different BC aerosol emission inventories and atmospheric aerosol representations are applied as well as different combinations of land-based snow, snow on sea ice and sea ice are included in the radiative forcing estimates. Thus, it is a challenging task to compare the different studies to the radiative forcing estimated in the present study. However, in the following different studies are selected for the comparison: Flanner et al. (2007) provide global annual mean instantaneous surface radiative forcing over land and sea ice ranging from 0.007 to 0.13 Wm^{-2} for low to high fossil fuel and bio fuel emission estimates for a strong boreal fire year (1998) and from 0.007 to 0.12 Wm^{-2} for a weak boreal fire year (2001). The emissions used in the present study are about 20 % lower compared to the emissions used for the central estimate of the study by Flanner et al. (2007), there leading to radiative forcing values of 0.054 and 0.049 Wm^{-2} acting over land and sea ice, and a radiative forcing of 0.044 and 0.041 Wm^{-2} acting only over land. The radiative forcing values acting only over land are about a factor of 6 larger compared to the radiative forcing of 0.007 Wm^{-2} estimated in the present study. The instantaneous radiative forcing values averaged only over land snowpack in the present study is about a factor of 5 (0.11 compared to 0.55 Wm^{-2}) to 6 (0.11 compared to 0.60 Wm^{-2}) lower compared to Flanner et al. (2007). In another study, Flanner et al. (2009) present a global annual mean TOA radiative forcing caused by BC in snow of 0.057 Wm^{-2} and annual mean surface radiative forcing averaged only over snow of 0.70 Wm^{-2}. These radiative forcing values are about a factor of 8 (0.057 compared to 0.00669 Wm^{-2}) to 9 (0.70 compared to 0.11 Wm^{-2}) higher compared to the forcing estimated in the present study. Lawrence et al. (2012) also estimated a global annual mean surface radiative forcing from BC aerosols in land-based snowpack for the present-day period of 0.037 Wm^{-2}. This is lower compared to the estimates of Flanner et al. (2007) and Flanner et al. (2009). Another study by Goldenson et al. (2012) estimated a global annual mean TOA forcing of BC on land and sea ice of 0.039 Wm^{-2}, which is also lower than the estimate by Flanner et al. (2007) and Flanner et al. (2009). Assuming a contribution of 80 % of the land-based snow to the total instantaneous radiative forcing (as given in Flanner et al. (2007)), the instantaneous radiative forcing by Goldenson et al. (2012) is a factor of 5 higher compared to the present study.
Overall, the instantaneous radiative forcing resulting from this study with 6.69 mWm^{-2} is at the lower bound of other modelling studies. ECHAM6 has the tendency to underestimate the snow cover especially in the spring season and additionally has

a too weak BC aerosol transport towards the northern high latitudes (section 3.1.2, section 2.2), which might cause the low radiative forcing estimated in the present study compared to other studies.

Flanner et al. (2007), for example, showed that differences in BC aerosol emissions can lead to a strong non-linear response in the resulting instantaneous radiative forcing. In their study they found that a difference of a factor of 2.5 from the low to the central estimate for regions north of 30°N for the year 1998 (1.4 compared to 3.5 Tgyear^{-1}), do not lead to a radiative forcing which increases by about a factor of 2.5, but shows an increase by about a factor of 8 (0.007 compared to 0.054 Wm^{-2}). This highlights the non-linear response of the radiative forcing to the BC aerosol deposition. Thus, a strong impact from a too weak long-range BC aerosol transport into the high latitudes can be expected.

Chapter 4

Impact of pre-industrial and future BC aerosol deposition on BC concentrations in snow, albedo, and radiation

This chapter summarizes the impact of pre-industrial (PI, 1880-1889) and projected future (RCP85, 2090-2099) BC aerosol deposition fluxes on BC concentrations in land-based snow, albedo and radiation and compares it to present-day (PD, 2000-2009) conditions which were presented in the previous chapter. Considered are BC aerosol deposition fluxes originating from all sources, anthropogenic as well as natural. Projected future climate and BC aerosol conditions follow the RCP8.5 scenario. Section 4.1 presents the differences in pre-industrial and future BC aerosol deposition fluxes, snow cover, and BC concentrations in snow compared to present-day conditions. The albedo reductions caused by pre-industrial and projected future BC aerosol deposition fluxes on snow are described in Section 4.2. The impact of the albedo reductions due to the BC contamination of snow on the radiation is estimated in terms of instantaneous radiative forcing in section 4.3.

4.1 Pre-industrial and future BC aerosol deposition fluxes, snow cover, and BC concentrations in snow compared to present-day conditions

Figure 4.1 shows differences in simulated pre-industrial (left) and future (right) BC aerosol deposition fluxes (top), snow cover (middle), and BC concentrations in snow (bottom) compared to present-day conditions. Here, averages over the particular time periods are shown.
For pre-industrial times the global total BC aerosol deposition fluxes were about 47 % lower compared to present-day conditions (3.90 compared to 7.41 Tgyear^{-1}). For the future, the BC aerosol deposition fluxes are about 40 % lower compared to present-day conditions (4.45 compared to 7.41 Tgyear^{-1}).
Lower BC aerosol deposition fluxes in pre-industrial times compared to the present-day time period are found especially over China, South America and Africa as shown in the top panel of Figure 4.1 on the left-hand side. Higher BC aerosol deposition fluxes are found in eastern North America, Scandinavia, Greenland, and over the Arctic Ocean,

because the PI time period as defined in the present study covers the end of the 19th century when the industrial revolution was already well underway. The differences in pre-industrial and present-day snow cover (Figure 4.1, middle (left)) show more snow cover in the pre-industrial time period. Only a few regions e.g. in the North Siberian Plain, in some places in Mongolia, and Alaska show less snow cover in the pre-industrial time period. In general, the resulting pre-industrial BC concentrations in snow (Figure 4.1, bottom (left)) follow the patterns in the BC aerosol deposition differences: In eastern North America and Scandinavia higher pre-industrial BC aerosol deposition fluxes result in higher BC concentrations in snow. For the North Siberian Plain, however, lower pre-industrial BC aerosol deposition fluxes and less snow cover actually result in higher BC concentration in snow, which relates to the non-linear dependency of BC concentrations in snow on the snowfall. Global averaged BC concentrations in snow, only considering snow depths higher than 1 mm where snow is present, are about 63 % lower for the pre-industrial time period compared to present-day conditions (16.84 compared to 44.98 ng(BC)g(snow)$^{-1}$).

Comparing projected future und present-day BC aerosol deposition fluxes (Figure 4.1, top (right)), also leads to lower future BC aerosol deposition fluxes almost over all continents compared to present-day. Exceptions are the southern part of Africa, northern parts of Alaska and Canada, the western part of Greenland as well as mountainous regions around the Tibetan Plateau where higher BC aerosol deposition fluxes are found. Some spots of higher future BC aerosol deposition fluxes are also in the Antarctic. Comparing the future snow cover to present-day conditions (Figure 4.1, middle (right)), the differences show an overall reduction in the future snow cover. In general, less future snow cover combined with lower BC aerosol deposition fluxes causes lower BC concentrations in snow compared to present-day conditions (Figure 4.1, bottom (right)). To quantify this with numbers, the BC concentrations in snow for the projected future time period are reduced by about 83 % in contrast to present-day conditions (7.59 compared to 44.98 ng(BC)g(snow)$^{-1}$). Although the total reduction of the BC aerosol deposition fluxes is similar for pre-industrial and projected future conditions, compared to present-day, the reduction in the BC concentrations in snow is stronger for the future. This is a result of the spatial distribution in the differences of the BC aerosol deposition fluxes, which shows a stronger reduction in the projected future BC aerosol deposition fluxes over the snow covered regions compared to pre-industrial times (Figure 4.1, top).

4.2 Albedo reductions due to pre-industrial and future BC aerosol deposition on snow

The simulated albedo reductions caused by the deposition of BC aerosols on snow for pre-industrial (PI, 1880-1889) and projected future (RCP85, 2090-2099) conditions are described in the following and are compared to albedo reductions due to BC aerosol deposition on snow for present-day (PD, 2000-2009) conditions.

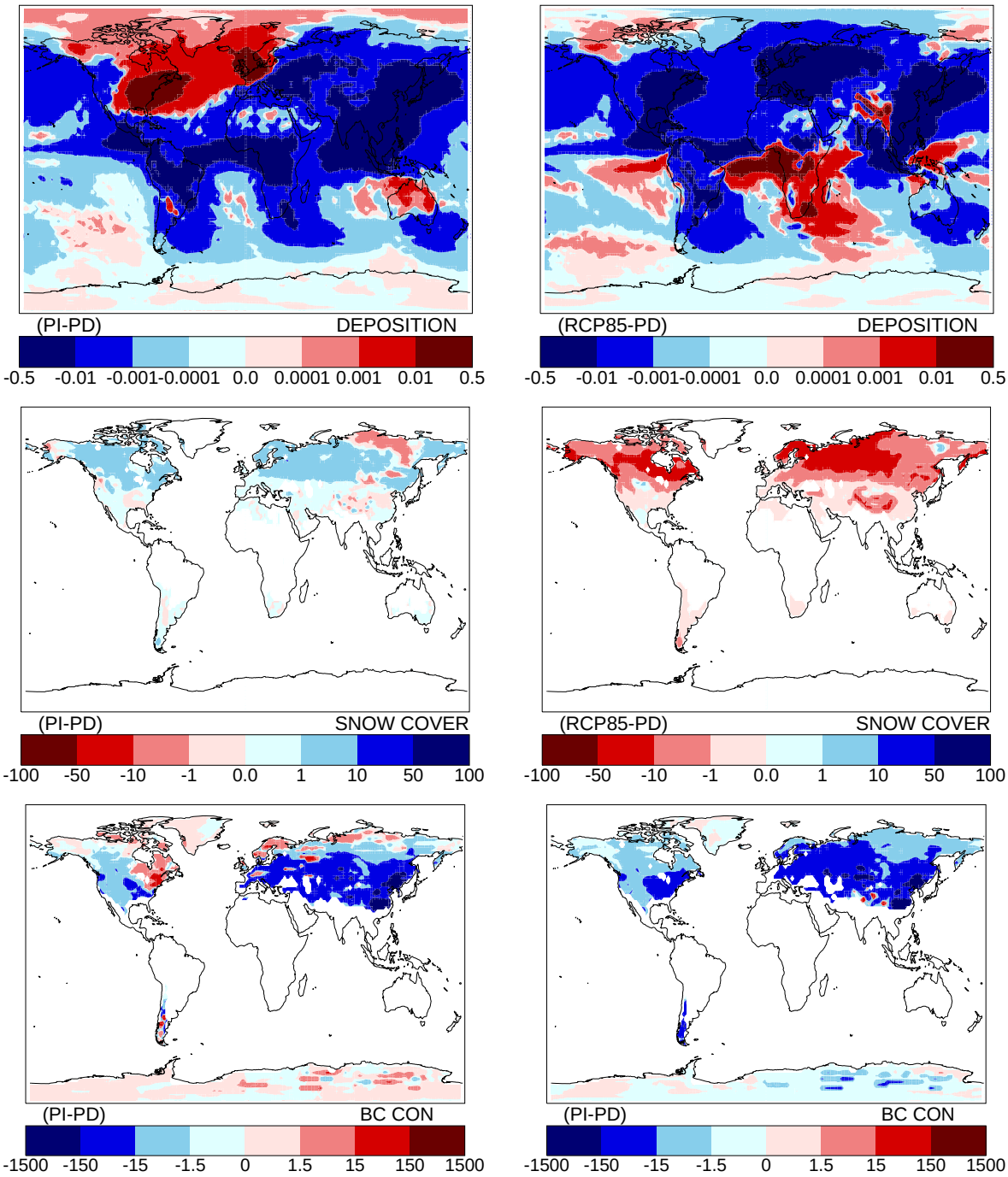

Figure 4.1: Differences in simulated BC aerosol deposition fluxes (top), BC concentrations in snow (middle), and snow cover (bottom), averaged over ten simulation years. Top: Differences between simulated pre-industrial and present-day (left) and between future and present-day BC aerosol deposition fluxes (right) in $gm^{-2}year^{-1}$. Middle: Differences between simulated pre-industrial and present-day (left) and between future and present-day snow cover (right) in %. Bottom: Differences between simulated pre-industrial and present-day (left) and between future and present-day BC concentrations in snow (right) in $ng(BC)g(snow)^{-1}$.

Figure 4.2 on the left shows zonally averaged snow albedo reductions for the different latitudes (-90°S-90°N), averaged over ten simulation years for pre-industrial (PI) and the projected future (RCP85) conditions compared to present-day (PD) conditions, respectively. In general, smaller snow albedo reductions are found for the pre-industrial time period compared to present-day conditions. The smallest snow albedo reductions occur for the future time period, which was expected due to decreased BC aerosol deposition fluxes and decreasing snow cover compared to present-day conditions. Considering different regions, the snow albedo reductions for the pre-industrial time period are very similar for the Antarctic compared to present-day conditions, but somewhat smaller for the future time period. In the region between -30°S and -15°S, a retreat in the snow cover extent from the pre-industrial to the future time period results in a shift of snow albedo reductions to more southern latitudes. In the Arctic region from 60°N northward, the snow albedo reductions are similar for pre-industrial times compared to the present-day period. Here, also the global total amount of the BC aerosols deposited on snow are similar for the two time periods with about 0.22 Tgyear^{-1} (see section 2.2). The snow albedo reductions for the future time period are smaller compared to present-day conditions, which was expected given that about 50 % less BC aerosols are deposited on snow in the Arctic region (0.10 compared to 0.22 Tgyear^{-1}). In general, the snow albedo reductions decrease northward from about 50°N for all three simulations, showing similar snow albedo reductions north of 75°N.

The zonally averaged total surface albedo reductions averaged over ten simulation years for the three time periods, respectively, are shown in Figure 4.2 on the right. The reductions in the total surface albedo are obtained by subtracting total surface albedo values including and excluding BC aerosol deposition on snow which are calculated within one simulation (see section 2.3). As shown before (see section 3.3), the total surface albedo reductions are much smaller than the snow albedo

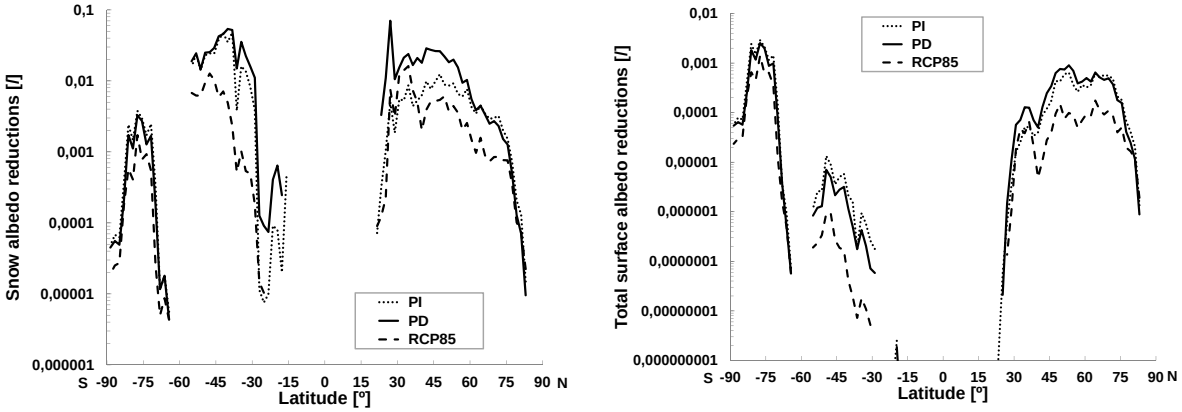

Figure 4.2: Pre-industrial (PI, 1880-1889), present-day (PD, 2000-2009) and projected future (RCP85, 2090-2099) snow albedo (left) as well as total surface (right) albedo [/] reductions resulting from the implemented snow-albedo-scheme in ECHAM6 zonally averaged for the different latitudes. Albedo values are averaged over ten simulation years, respectively. Left: Snow albedo reductions considering only grid boxes with a snow depth exceeding 1mm. Right: The total surface albedo reductions are only shown in grid boxes that are significant on a 95 % confidence interval based on a Student t-test.

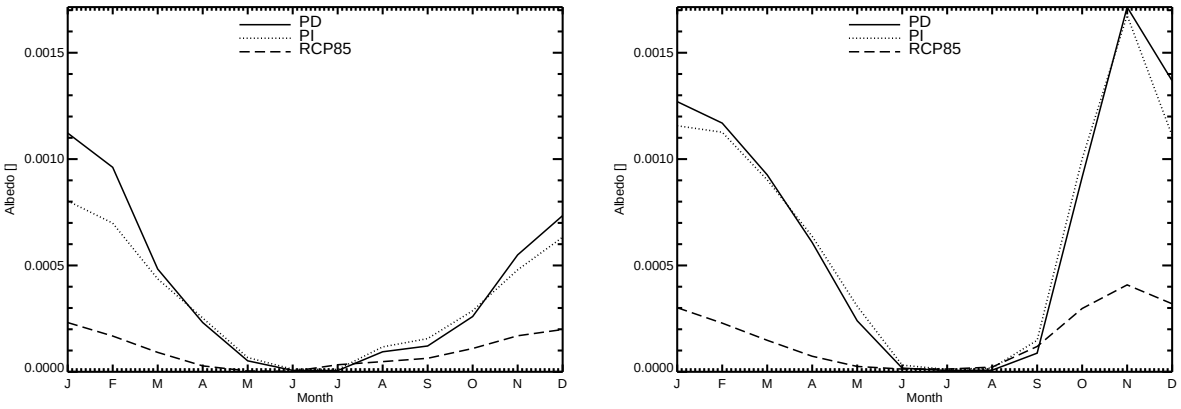

Figure 4.3: Monthly mean differences in the total surface albedo [/] reductions between with and without BC aerosol deposition on snow averaged over ten simulation years for pre-industrial (PI, 1880-1889), present-day (PD, 2000-2009) and projected future (RCP85, 2090-2099) conditions globally (left) as well as for the Arctic region (60°N - 90°N, right).

reductions alone. Overall, the reductions in the total surface albedo are highest for the present-day period, followed by the pre-industrial time period, while the projected future time period shows the smallest total surface albedo reductions. This is in line with the changes in the snow albedo for the different time periods considered. In addition, highest total surface albedo reductions are not found in the regions where also highest snow albedo reductions occur, but in regions where the snow cover persists over a longer time period over the year and not only persists during winter time. In addition, larger snow albedo reductions are found for pre-industrial times between 30°N and 75°N compared to present-day, however, the changes in the total surface albedo are almost equal for two time periods, which reveals the influence of the changing snow cover. Overall, the total surface albedo reductions are about 14 % lower for pre-industrial conditions versus present-day conditions (-0.00033 compared to -0.00039) and about 76 % lower for the projected future conditions compared to the present-day time period (-0.000094 compared to -0.00039).

The monthly mean differences in the total surface albedo due to the deposition of BC aerosols on snow for the three performed simulations for the pre-industrial (PI), present-day (PD), and the future (RCP85) time period are shown in Figure 4.3. Here, globally averaged (left) as well as total surface albedo reductions for the Arctic region (60°N - 90°N, right) are presented separately.
The global total surface albedo reductions of the three simulations show the same seasonal behaviour with increasing albedo differences from August to a maximum in January followed by a decrease until June. Minimum values in the global total surface albedo reductions are found in June and July. The largest total surface albedo reductions occur for the PD simulation, followed by the PI simulation. The smallest total surface albedo differences are found for the future RCP85 simulation. Generally, the total surface albedo reductions for the Arctic region (60°N - 90°N) are higher compared to the reductions on a global scale but the relative changes for all simulations are comparable. The peak in the total surface albedo reductions in the Arctic region is found in November for all three simulations. As described in section 3.3, the largest

effect on the radiative forcing for the Arctic region is expected in spring (MAM) due to higher incoming solar radiation over land compared to the autumn season (SON), even if the largest reductions in the total surface albedo occur in November.

4.3 Pre-industrial and future instantaneous radiative forcing from BC aerosol deposition on snow

In the following, the effect of pre-industrial (PI, 1880-1889) and future (RCP85, 2090-2099) deposition of BC aerosols on land-based snowpack on the radiation balance is estimated in terms of the instantaneous radiative forcing. The results are also compared to present-day (PD, 2000-2009) conditions. The calculation of the instantaneous radiative forcing is described in section 3.4.

The distribution of the instantaneous radiative forcing averaged over the pre-industrial (PI), present-day (PD), and the projected future (RCP85) time period, respectively, are summarized in Figure 4.4. The regional patterns of the instantaneous radiative forcing are very similar for the PI, PD, and the RCP85 simulations. Locally, the instantaneous radiative forcing can reach high values, showing values of more than 1 Wm^{-2} in regions close to the strong anthropogenic emission sources e.g. China, in mountainous regions as well as in the Antarctic. The instantaneous radiative forcing values are thereby highest for the PD simulation followed by the PI simulation. For the projected RCP85 conditions the lowest instantaneous radiative forcing is simulated.

The global and Arctic (60°N-90°N) instantaneous radiative forcing for the top of the atmosphere (TOA) and the surface (SUR) under total-sky conditions averaged over ten simulation years for the three performed simulations (PI, PD, and RCP85, respectively) are summarized in Table 4.1. The instantaneous radiative forcing values are shown as annual means (ANNUAL) as well as seasonal averages (DJF, MAM, JJA, and SON) for TOA. $ANNUAL_{snow}$ instantaneous radiative forcing values represent annual averages, only considering snow covered land regions.

The global annual mean instantaneous radiative forcing for TOA total-sky conditions for pre-industrial times is about 15 % lower with 5.70 mWm^{-2}, the future simulation shows about 72 % lower radiative forcing with 1.85 mWm^{-2} compared to the present-day conditions (6.69 mWm^{-2}). The instantaneous radiative forcing at the surface is very similar compared to the TOA forcing for all three simulations.
Regarding the seasonal variations of the instantaneous radiative forcing, for all three time periods the highest instantaneous radiative forcing is found in the winter season DJF. The lowest instantaneous radiative forcing for all simulation occurs in the summer season JJA with instantaneous radiative forcing values less than 0.25 mWm^{-2}. These seasonal variations follow in general the total surface albedo reductions as shown in Figure 4.5 on the left as monthly mean instantaneous radiative forcing averaged globally over ten simulation years. The instantaneous radiative forcing in DJF is thereby about 20 % lower for pre-industrial times compared to present-day

conditions (13.46 compared to 16.90 mWm^{-2}), the projected future instantaneous radiative forcing is reduced by about 71 % in DJF compared to present-day conditions (4.87 compared to 16.90 mWm^{-2}). Similar reductions are found for the land-based snowpack. The instantaneous radiative forcing averaged only over snow covered regions for the pre-industrial times is about 15 % lower compared to present-day conditions (82.06 compared to 110.05 mWm^{-2}). The RCP85 simulation results in an about 71 % lower instantaneous radiative forcing compared to the present-day period (31.61 compared to 110.05 mWm^{-2}).

In contrast to the global scale, the instantaneous radiative forcing for the PI simulation exceeds the forcing for the present-day time period (9.67 compared to 9.25 mWm^{-2}) for the Arctic region (60°N - 90°N). In addition, the Arctic instantaneous radiative forcing of about 1.76 mWm^{-2} for the projected future RCP8.5 scenario is even about 5 % lower compared to the forcing on the global scale with 1.85 mWm^{-2}. This is also reflected in the seasonal cycle of the monthly mean instantaneous radiative forcing for the Arctic shown in Figure 4.5 on the right. The seasonal behaviour for the

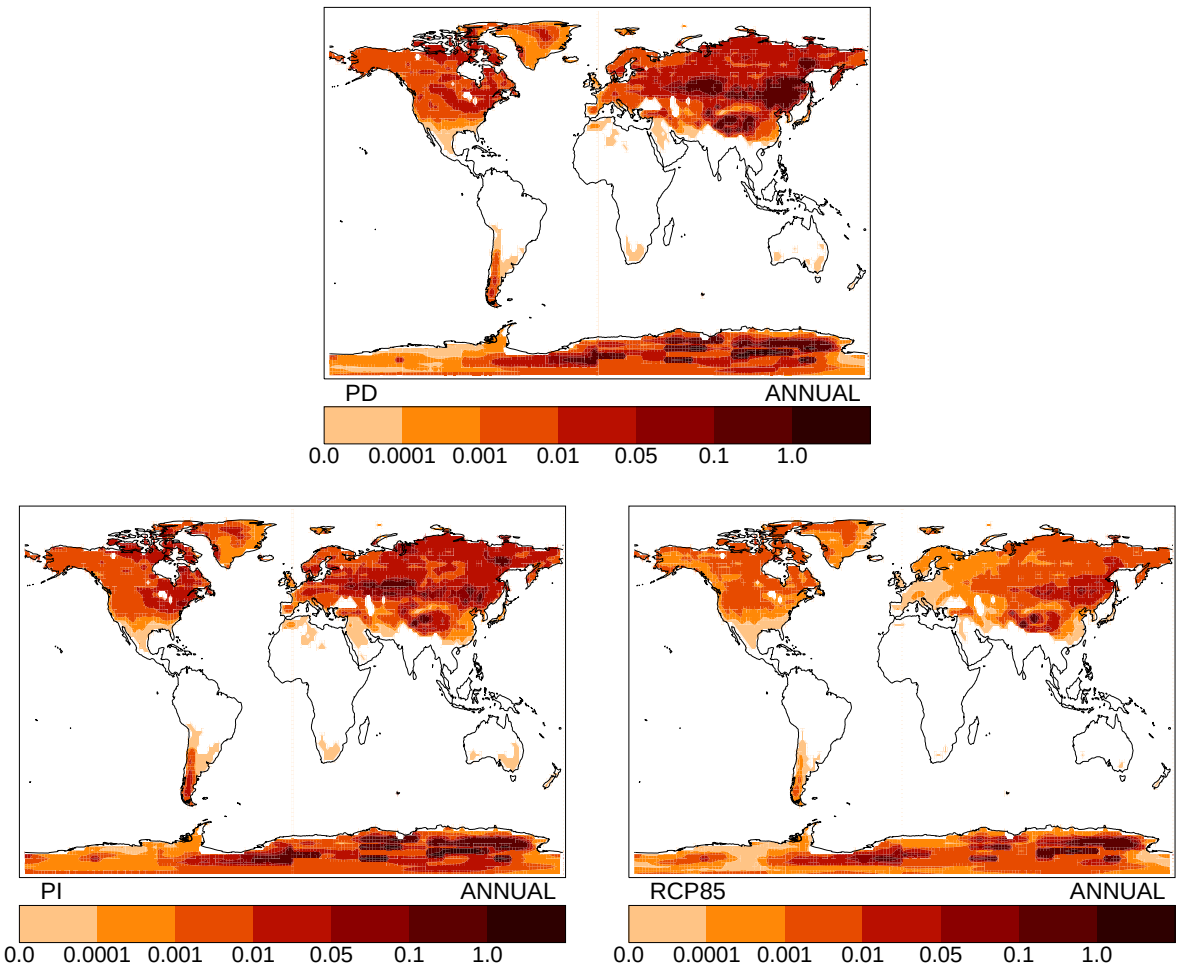

Figure 4.4: Instantaneous radiative forcing (total-sky, TOA, Wm^{-2}) averaged over ten simulation years for the present-day (PD, 2000-2009, top), pre-industrial (PI, 1880-1889, bottom left), and projected future (RCP85, 2090-2099, bottom right) conditions.

Table 4.1: Global and Arctic (60°N-90°N) pre-industrial (PI, 1880-1889), present-day (PD, 2000-2009), and projected future (RCP85, 2090-2099) instantaneous radiative forcing and standard deviations in mWm^{-2} for total-sky conditions resulting from the deposition of BC aerosols on land-based snow, averaged over ten simulation years, respectively. ANNUAL represents annual means and is shown for the surface (SUR) as well as for the top of the atmosphere (TOA). DJF, MAM, JJA, and SON values are averages over the respective seasons for TOA. $ANNUAL_{snow}$ shows annual averages only over the land-based snowpack.

RF [$\mathbf{mWm^{-2}}$]	**Global**		
	PI	PD	RCP85
ANNUAL (SUR)	5.97 ± 3.87	7.00 ± 3.25	1.94 ± 1.74
ANNUAL (TOA)	5.70 ± 3.72	6.69 ± 3.14	1.85 ± 1.67
DJF	13.46 ± 9.80	16.90 ± 9.16	4.87 ± 4.48
MAM	4.46 ± 3.46	5.25 ± 4.45	1.00 ± 1.11
JJA	0.21 ± 0.15	0.12 ± 0.09	0.06 ± 0.08
SON	4.83 ± 5.96	4.68 ± 5.21	1.54 ± 2.41
$ANNUAL_{snow}$ (SUR)	82.06 ± 39.95	110.05 ± 36.62	31.61 ± 20.49
$ANNUAL_{snow}$ (TOA)	79.03 ± 38.39	105.96 ± 35.35	30.36 ± 19.70
	Arctic		
	PI	PD	RCP85
ANNUAL (SUR)	10.20 ± 0.84	9.76 ± 1.86	1.87 ± 0.64
ANNUAL (TOA)	9.67 ± 0.80	9.25 ± 1.76	1.76 ± 0.60
DJF	4.54 ± 4.10	5.52 ± 4.92	1.12 ± 0.93
MAM	25.22 ± 5.64	23.88 ± 8.18	4.07 ± 1.84
JJA	1.31 ± 1.68	0.66 ± 0.87	0.64 ± 1.02
SON	7.45 ± 3.71	6.82 ± 3.82	1.19 ± 0.63
$ANNUAL_{snow}$ (SUR)	43.90 ± 3.67	43.84 ± 7.73	9.25 ± 2.10
$ANNUAL_{snow}$ (TOA)	41.96 ± 3.85	41.97 ± 7.37	8.82 ± 1.98

PI and the RCP85 simulation is similar compared to the PD simulation. In general, the instantaneous radiative forcing in the Arctic region is most pronounced in the spring season MAM for all three simulations, reaching values ranging from 4.07 mWm^{-2} for the future RCP85 simulation and up to 25.22 mWm^{-2} for pre-industrial conditions (see Table 4.1). A stronger instantaneous radiative forcing is shown for pre-industrial times for the seasons MAM, JJA, and SON compared to present-day conditions. Only in DJF the instantaneous radiative forcing is strongest for present-day conditions. The lowest instantaneous radiative forcing occurs in the summer season JJA for all three simulations and in general for the RCP85 simulation.

The Arctic region is by far most sensitive to the deposition of BC aerosols on snow in the spring season in all three simulations, even if this time of the year does not provide the highest amount of BC aerosol deposition fluxes transported to the Arctic (see section 2.2) and does not provide the strongest changes in the total surface albedo (see section 3.3). However, not only the differences in the total surface albedo due to the contamination by BC aerosols in snow are a key parameter for the radiative forcing but also the solar incoming radiation which is available (see section 3.3).

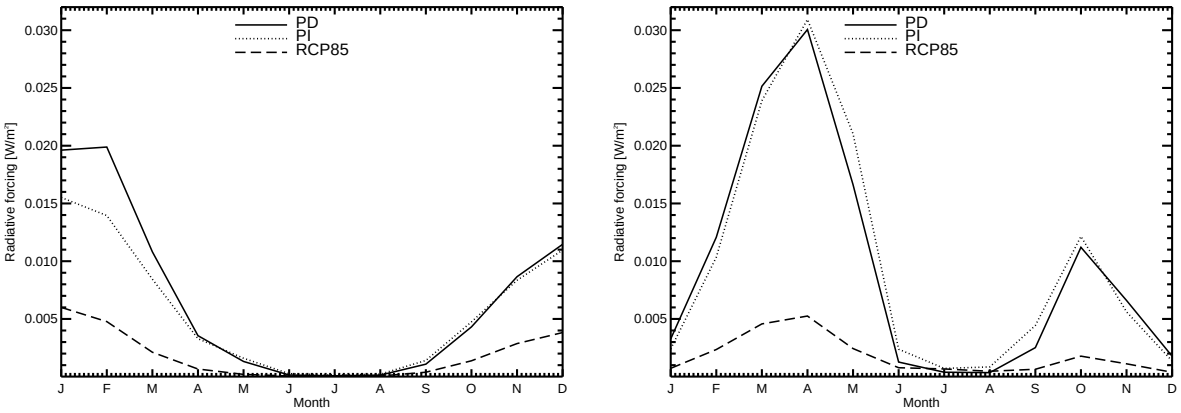

Figure 4.5: Monthly mean instantaneous radiative forcing [Wm^{-2}] averaged over ten simulation years for the PI, PD, and RCP85 simulations, showing global averages on the left and averages over the Arctic region (60°N-90°N) on the right.

Averaging the instantaneous radiative forcing for the PI and the RCP85 simulation only over snow covered land regions for the Arctic, leads to a similar instantaneous radiative forcing for the PI compared to the PD simulation (41.96 compared to 41.96 mWm^{-2}), and to a about 79 % lower instantaneous radiative forcing for the RCP85 simulation compared to present-day conditions (8.82 compared to 41.96 mWm^{-2}).
In general, the global instantaneous radiative forcing resulting from the deposition of BC aerosols on snow is simulated to decline in the projected future conditions due to less snow cover and lower BC aerosol deposition fluxes in the RCP85 simulation compared to present-day conditions. This future decline is even more pronounced when only accounting for the Arctic region in the RCP85 simulation. Between pre-industrial and present-day times this study shows an increase in the instantaneous radiative forcing by about 15 %. This is about a factor of 2.5 lower than the 38 % decrease estimated in a modelling study by Lawrence et al. (2012) for changes between pre-industrial (1850-1869) and present-day (1986-2005) conditions (0.023 compared to 0.037 Wm^{-2}). To our knowledge, no other study estimated the change in the radiative forcing between pre-industrial and present-day times. This is the first study to assess the change in the instantaneous radiative forcing related to the deposition of black carbon aerosols on snow covered land regions between present-day and future.

Chapter 5

Climate or BC aerosol deposition: What controls changes in the radiative forcing from BC aerosol deposition on snow between present-day and projected future climate conditions?

Changes in the instantaneous radiative forcing between pre-industrial (PI) and present-day (PD) as well as present-day and projected future conditions (RCP85) are controlled by changes in snow cover and by changes in BC aerosol deposition fluxes. How much of the total changes in the instantaneous radiative forcing can be attributed to these two controlling factors is further analysed. The analysis is thereby limited to the difference between present-day and projected future conditions. For this, a factor separation following Stein and Alpert (1993) is applied, as described in section 5.1. The resulting contributions assigned to climate and BC aerosol deposition fluxes as well as the synergies are summarized in section 5.2.

5.1 Factor separation technique

To separate the contributions of changes in snow cover which are linked to climate and BC aerosol deposition fluxes on the total changes of the instantaneous radiative forcing, a factor separation analysis introduced by Stein and Alpert (1993) is applied. This factor separation analysis allows to investigate the single contribution of the controlling factors as well as the synergies between them. This factor separation analysis has been applied in other studies as well (e.g. Alpert and Sholokhman, 2011; Claussen et al., 2013).
To follow the factor separation, 2^n simulations are needed, where n represents the number of the controlling factors in the analysis. Thus, for the present study four simulations are needed for the contribution of the climate and the BC aerosol deposition ($n = 2$), which are described in the following:

(1) The **PD** simulation (described in detail in chapter 3) considers present-day climate as well as present-day BC aerosol deposition fluxes.

(2) The **RCP85** simulation (described in detail in chapter 4) considers projected future climate following the RCP8.5 scenario as well as projected future BC aerosol deposition fluxes following the RCP8.5 as well.

(3) The **cPD_dRCP85** simulation applies present-day climate combined with BC aerosol deposition fluxes as projected for the projected future RCP8.5 scenario.

(4) The **cRCP85_dPD** simulation applies projected future climate conditions following the RCP8.5 scenario and present-day BC aerosol deposition fluxes.

The setup for the single simulations is described in section 2.3.

The contribution of the climate to the total changes in the instantaneous radiative forcing f_C (using PD conditions as a reference state) is given by the difference of the instantaneous radiative forcing simulated in the cRCP85_dPD and the PD simulation

$$f_C = cRCP85\_dPD - PD. \tag{5.1a}$$

The contribution of changes in the BC aerosol deposition fluxes to the total changes in the instantaneous radiative forcing f_D, respectively, is given by

$$f_D = cPD\_dRCP85 - PD. \tag{5.1b}$$

If the contributions f_C and f_D do not add up to the total change in the instantaneous radiative forcing between the present-day and the projected future time period, the system constitutes synergies which are defined as

$$f_{CD} = RCP85 - PD - f_C - f_D. \tag{5.1c}$$

Alternatively, Equations 5.1a and 5.1b, can use the RCP85 simulation as a reference state. In this case Equations f_C and f_D will change, but qualitatively the same processes will be described, only from a different point of view, so that no new information is obtained by a separate investigation with a different reference state (Claussen et al., 2013). Thus, the analysis is restricted to the PD state as a reference.

5.2 Results

The resulting global and Arctic (60°N-90°N) instantaneous radiative forcing values for all four simulations (PD, RCP85, cPD_dRCP85, and cRCP85_dPD) are summarized in Table 5.1.

Table 5.1: Global and Arctic (60°N-90°N) instantaneous radiative forcing and standard deviations in mWm^{-2} for total sky conditions resulting from the deposition of BC aerosols on land-based snow, averaged over ten simulation years. ANNUAL represents annual averages and is shown for the surface (SUR) as well as for the top of the atmosphere (TOA). DJF, MAM, JJA, and SON values are averages over the four seasons for TOA. Shown are the present-day (PD, 2000-2009) and future (RCP85, 2090-2099) simulations, as well as the two sensitivity simulations (cPD_dRCP85 and cRCP85_dPD).

RF [mWm^{-2}]	**Global**			
	PD	RCP85	cPD_dRCP85	cRCP85_dPD
ANNUAL (SUR)	7.00 ± 3.25	1.94 ± 1.74	3.71 ± 1.66	3.24 ± 2.68
ANNUAL (TOA)	6.69 ± 3.14	1.85 ± 1.67	3.55 ± 1.60	3.09 ± 2.57
DJF	16.90 ± 9.16	4.87 ± 4.48	8.63 ± 4.38	8.27 ± 7.21
MAM	5.25 ± 4.45	1.00 ± 1.11	2.77 ± 2.25	1.80 ± 1.91
JJA	0.12 ± 0.09	0.06 ± 0.08	0.08 ± 0.06	0.09 ± 0.13
SON	4.68 ± 5.21	1.54 ± 2.41	2.97 ± 3.35	2.28 ± 3.52
	Arctic			
	PD	RCP85	cPD_dRCP85	cRCP85_dPD
ANNUAL (SUR)	9.76 ± 1.86	1.87 ± 6.36	5.15 ± 1.66	4.17 ± 0.94
ANNUAL (TOA)	9.25 ± 1.76	1.76 ± 5.99	4.89 ± 1.60	3.93 ± 0.89
DJF	5.52 ± 4.92	1.12 ± 0.93	2.17 ± 4.38	3.32 ± 2.72
MAM	23.88 ± 8.18	4.07 ± 1.83	12.35 ± 2.25	9.05 ± 4.67
JJA	0.66 ± 0.87	0.64 ± 1.02	0.58 ± 0.06	1.03 ± 1.54
SON	6.82 ± 3.82	1.19 ± 0.63	4.29 ± 3.35	2.29 ± 1.47

On a global scale, the cPD_dRCP85 simulation performed with present-day climate conditions and projected future BC aerosol deposition fluxes shows about 47 % lower instantaneous radiative forcing with 3.55 mWm^{-2} compared to the PD simulation with 6.69 mWm^{-2}. Projected future climate and present-day BC aerosol deposition fluxes combined in the cRCP85_dPD simulation result in an about 54 % lower instantaneous radiative forcing with 3.09 mWm^{-2} compared to the PD simulation.
Similar ratios in the reductions of the instantaneous radiative forcing are also found for the Arctic region. Here, the cPD_dRCP85 simulation shows about 47 % lower instantaneous radiative forcing values (4.89 compared to 9.25 mWm^{-2}), the cRCP85_dPD simulation shows about 54 % lower instantaneous radiative forcing values compared to present-day conditions (3.93 compared to 9.25 mWm^{-2}). In general, also for the two sensitivity simulations, the instantaneous radiative forcing is higher in the Arctic than compared to the global values.

Figure 5.1 summarizes the total change in the instantaneous radiative forcing from present-day to projected future conditions (RCP85-PD), the contribution from the effect of the climate (Climate) f_C, the contribution of BC aerosol deposition (Deposition) f_D and the synergy (Synergy) f_{CD} of both processes for the global mean

as well as for the Arctic region (60°N-90°N).

Here, f_C and f_D contribute about equally to the total reduction of the instantaneous radiative forcing from present-day to projected future conditions (-3.60 and -3.14 mWm^{-2} globally; -5.32 and -4.36 mWm^{-2} for the Arctic). Or in other words the reduction in instantaneous radiative forcing in the future projection is to almost equally controlled by changes in climate leading e.g. to changes in snowfall and reduced snow cover and through changes in BC aerosol deposition fluxes. The positive synergies amount to about 1.90 mWm^{-2} on a global scale and to about 2.19 mWm^{-2} for the Artic region, which is about half as strong as the respective pure climate and BC aerosol contributions.

Similar to the analysis in Claussen et al. (2013), Equation 5.1c for the synergy f_{CD} can be reformulated to

$$\begin{aligned} f_{CD} &= RCP85 - PD - (cRCP85\_dPD - PD) - (cPD\_dRCP85 - PD) \\ &= (PD - cPD\_dRCP85) - (cRCP85\_dPD - RCP85). \end{aligned} \tag{5.2}$$

As such the synergy can be interpreted as the difference in the impact of BC aerosol deposition flux changes between PD and RCP85 under (i) present-day climate conditions (first bracket) and (ii) projected future RCP8.5 climate conditions (second bracket). Alternatively, Equation 5.2 can be reformulated to

$$f_{CD} = (PD - cRCP85\_dPD) - (cPD\_dRCP85 - RCP85). \tag{5.3}$$

In this case the synergy can be interpreted as the difference in changing the climate from PD to RCP85 with (i) present-day BC aerosol deposition fluxes present (first bracket) and (ii) with projected future RCP8.5 deposition fluxes present (second bracket).

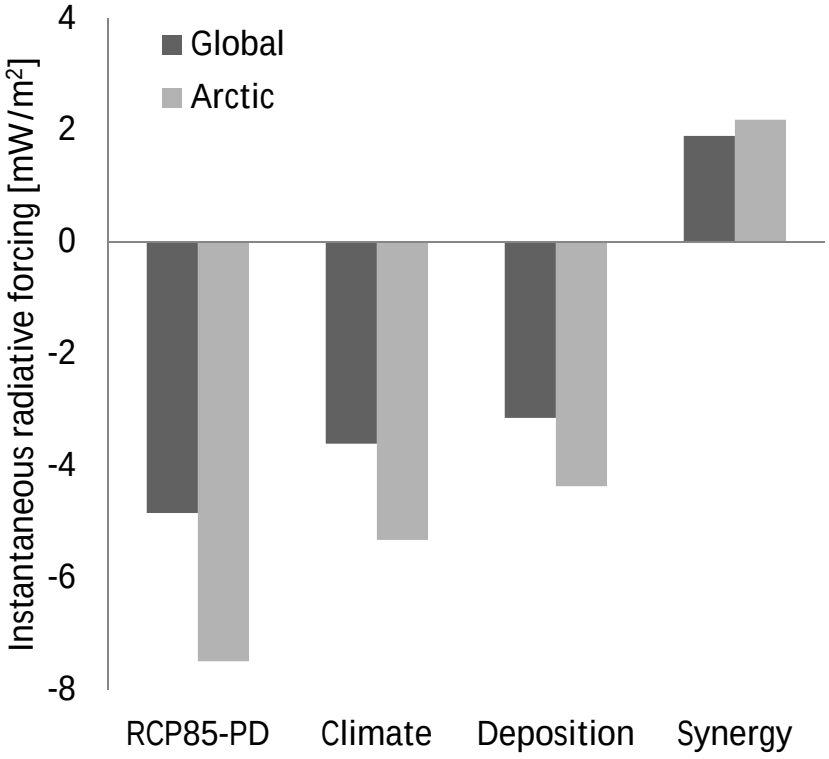

Figure 5.1: Differences in instantaneous radiative forcing globally as well as for the Arctic region (60°N-90°N). The climate effect (Climate) accounts for differences in varying climate conditions between the present-day and the future time period. The deposition effect (Deposition) considers differences in present-day and future BC aerosol deposition fluxes. Synergies (Synergy) result from the non-linear interaction between present-day and projected future changes in climate and BC aerosol deposition fluxes.

Chapter 6

Impact of present-day and future BC aerosols related to wildfires deposited on snow on BC concentrations in snow, snow cover, albedo, and radiation

Wildfires have a significant impact on the overall BC aerosol emissions globally contributing about 40 % to the total BC aerosol emissions (about 2.8 out of 7.5 Tgyear^{-1}; Bond et al., 2013). In addition, wildfires are strongly controlled by climate so that fire regimes are likely to change in a warmer future climate (Flannigan et al., 2009). The deposition of wildfire released BC aerosols on snow is potentially one important aspect in the overall role of fire within the Earth system. The present study gives a first estimate of the contribution of wildfire-related BC aerosol deposition on snow for present-day as well as projected future conditions, following the RCP8.5 for the end of the 21st century. In the following, the BC aerosol emission and deposition fluxes applied in the present study are summarized in section 6.1. The simulation setup is described in section 6.2. While in section 6.3 the impact of present-day wildfire related BC aerosols deposited on snow is described, section 6.4 summarizes the projected future impact and the changes compared to present-day conditions. The radiative forcing resulting from the darkening of snow through wildfire-related BC aerosol deposition is analysed in section 6.5 for present-day and projected future conditions. The contribution of changes in climate to the projected future instantaneous radiative forcing of the BC aerosol deposition on snow is analysed in section 6.6. In the end, section 6.7 describes the impact of changes in anthropogenic BC aerosol deposition fluxes from present-day to projected future conditions on the radiative forcing caused by the BC aerosol deposition on snow.

6.1 Simulating present-day and future wildfire BC aerosol emission and resulting deposition fluxes

The effect of the deposition of BC aerosols on snow emitted from wildfires is simulated in ECHAM6 by prescribing BC aerosol deposition fluxes which were precalculated in ECHAM6-HAM2 simulations (Veira et al., 2015b) for present-day and projected

future conditions (end of the 21st century). The effect of wildfires was thereby isolated from a simulation accounting for all BC aerosol emission sources and a simulation in which wildfire BC aerosol emissions were excluded. As the focus of the present study lies specifically on how the wildfire impact by the deposition of BC aerosols on snow will change in a changing climate, wildfire BC aerosol emissions are calculated within a process-based fire model. Here, the process-based fire model JSBACH-SPITFIRE (Lasslop et al., 2014) is applied to simulate wildfire BC aerosol emission fluxes for present-day and projected future conditions. The global circulation model ECHAM6 (Stevens et al., 2013) including the aerosol module HAM2 (Stier et al., 2005) uses these BC aerosol emission fluxes as boundary conditions to simulate the subsequent BC aerosol deposition fluxes. In the following, the JSBACH-SPITFIRE model is described in section 6.1.1 as well as the model setup to obtain the resulting BC aerosol deposition fluxes from ECHAM6-HAM2 simulations in section 6.1.2. This model setup is named the *SPITFIRE-setup* in the following.

6.1.1 The process-based fire model JSBACH-SPITFIRE and resulting wildfire emissions

The process-based fire model SPITFIRE (Thonicke et al., 2010) has been originally developed for the application in the LPJ (Sitch et al., 2003) Dynamic Global Vegetation Model (DGVM). In the following the main features of the model are briefly summarized. The model takes into account that fire is controlled by meteorological conditions (e.g. precipitation, minimum and maximum temperature, wind speed, soil moisture), the composition of the vegetation, as well as the fuel amount and the fuel characteristics. The SPITFIRE model explicitly accounts for ignition rates and distinguishes between ignition events caused by lightning or humans (depending on the population density). If specific conditions (based on several fire indices) for fuel availability and fuel moisture are met a fire can potentially be ignited. The fire spread is calculated after Rothermel (1972) as a function of wind speed and fuel moisture content. The model explicitly simulates the combustion of fuel and the intensity produced through fuel combustion. In addition, the post-fire mortality is taken into account through crown scorch and cambial death of trees. In the end, the fire-related emissions are derived by applying emission factors from Akagi et al. (2011). A complete description of the SPITFIRE model is given in Thonicke et al. (2010).

For the present study, the SPITFIRE model implemented in JSBACH (JSBACH-SPITFIRE; Lasslop et al., 2014) is applied. JSBACH (Brovkin et al., 2013; Reick et al., 2013; Schneck et al., 2013) is the land surface component of the Max Planck Institute for Meteorology Earth System Model (MPI-ESM; Giorgetta et al., 2013). For the implementation in JSBACH several modifications had to be applied: Two additional shrub types in JSBACH had to be considered as they were not included in LPJ. The vegetation height had to be included in JSBACH influencing the post-fire mortality of trees. Several parameters had to be adjusted (e.g. concerning human ignitions and fule moisture). Moreover, the influence of wind speed on the role of

the rate of spread was modified. A detailed description of the modifications and the evaluation of the performance of JSBACH-SPITFIRE are summarized in Lasslop et al. (2014).

In the present study simulations performed to obtain the wildfire emissions with JSBACH-SPITFIRE are used covering the time period 1850 to 2100 as described in detail in Veira et al. (2015b), based on the simulations performed in Lasslop et al. (2014). The emissions for present-day conditions are based on a transient simulation covering the time period 1850-2005 as described in Lasslop et al. (2014), with the exception that model output from MPI-ESM resulting from the CMIP5 (Giorgetta et al., 2013) model intercomparison project is used instead of reanalysis data. For the projected future time period covering 2006-2100, model output from the MPI-ESM for the RCP scenario RCP8.5 (van Vuuren et al., 2011) is used. The population density from 1850-2005 is based on the HYDE data base (Goldewijk, 2001; Klein Goldewijk and Verburg, 2013), while for the future time period (2006-2100) the data set has been extended by population density predictions following Shared Socio-economic Pathways (SSPs). Here, the RCP8.5 scenario is combined with the SSP3 according to van Vuuren and Carter (2014). The land use change is based on Hurtt et al. (2011). Focusing only on the emissions of BC aerosols, the emission factors used to identify the fraction of carbon which is emitted as BC aerosols are based on Akagi et al. (2011). Due to an observed discrepancy between bottom-up compared to top-down fire aerosol emission estimates, multiple studies (Huijnen et al., 2012; Kaiser et al., 2012; von Hardenberg et al., 2012) suggest a global correction factor of 3.4 for BC and OC emissions from wildfires. The inconsistency with bottom-up estimates might be induced by an inaccurate representation of aerosols or optical properties of smoke in the models, errors in the estimates of biomass combustion, or inaccuracies in the emission factors. Also in the present study a correction factor of 3.4 has been applied. The resulting BC aerosol emissions for present-day conditions thereby compare reasonably well to other biomass burning estimates as shown in detail in Veira et al. (2015b).

The wildfire BC aerosol emission fluxes resulting from the JSBACH-SPITFIRE model applied with the model setup described in the previous section are shown in Figure 6.1. For the analysis, ten simulation years are used covering 1996-2005 for the present-day period and from 2090-2099 for the projected future time period. In the top panel of Figure 6.1 on the left, wildfire BC aerosol emission fluxes are shown for present-day conditions, the top panel on the right shows the wildfire BC aerosol emission fluxes for future conditions projected for the RCP8.5 scenario. For present-day as well as for the projected future, the spatial distribution of the large wildfire BC emission sources is similar: Large wildfire BC aerosol emission sources are found in the central part of Eurasia, southern Europe, the southern part of North America and Africa, as well as in South America and along the eastern coast of Australia. No sources of wildfire BC aerosol emissions are found in glaciated areas like the Greenland Ice Sheet, the Antarctic and mountainous regions like the Tibetan Plateau, but also in the northern part of Canada as well as in desert regions. The global total BC aerosol emission fluxes from wildfires for the present-day time period

sum up to about 7.43 Tgyear^{-1}. For the projected future RCP8.5 scenario, the global total wildfire BC aerosol emission fluxes show about 5 % higher BC aerosol emissions compared to present-day conditions summing up to about 7.84 Tgyear^{-1}. Overall, a pronounced decrease between present-day and projected future wildfire BC aerosol emission fluxes is found in most of the tropical regions, while an increase in future wildfire BC aerosol emission fluxes is found in the extratropics, which is considerably pronounced in the boreal regions in the Northern Hemisphere as shown in the bottom panel of Figure 6.1. The decrease in the tropics is thereby related to increases in agricultural areas and population. In the extratropics, the increase is related to changes in climate, which lead to a lengthening of the fire season (Veira et al., 2015b). In the Arctic region (60°N-90°N) the increase in the wildfire BC aerosol emissions from present-day to projected future conditions is more pronounced compared to the global scale. Here, the total wildfire BC aerosol emissions increase by about a factor of 3 from the present-day to projected future times (0.025 compared to 0.071 Tgyear^{-1}).

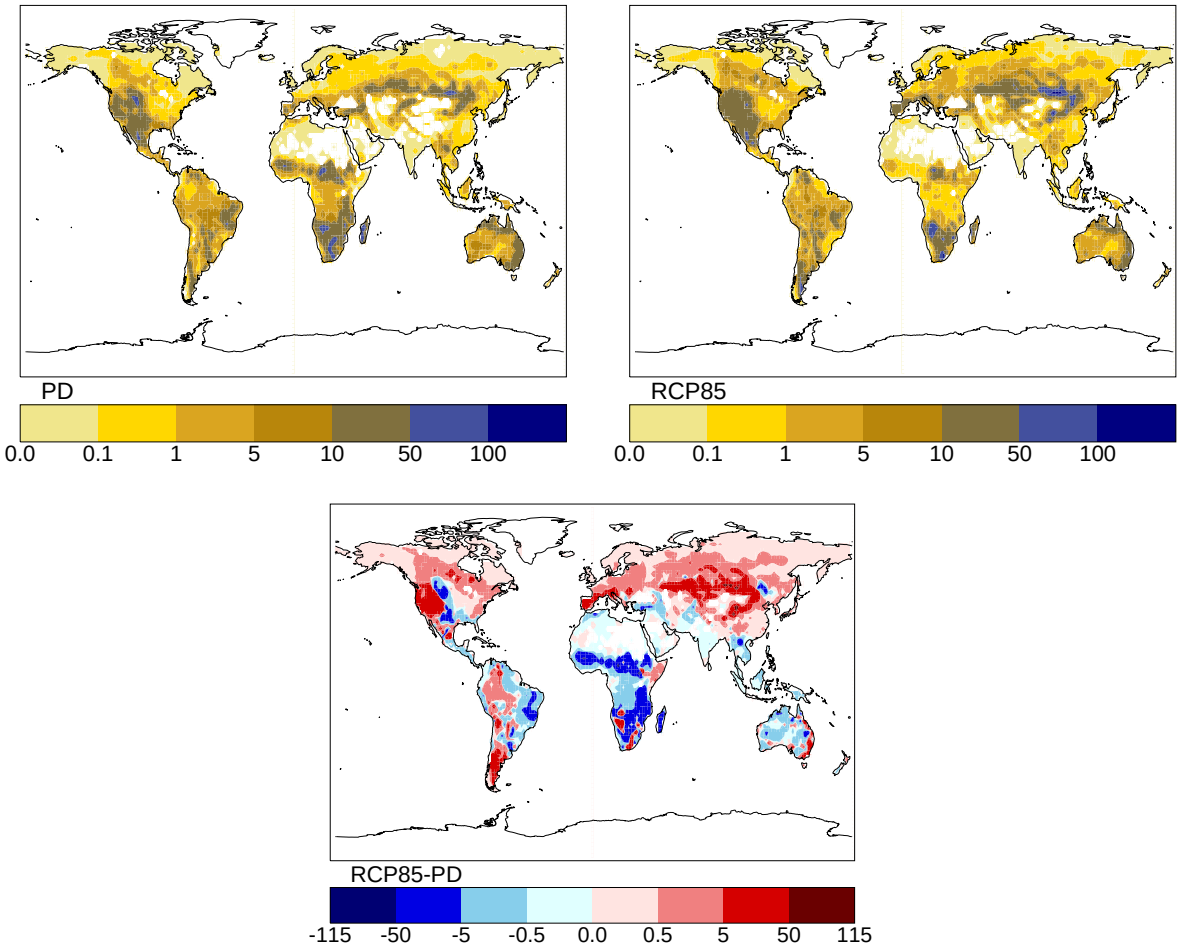

Figure 6.1: BC aerosols emitted from wildfires in mgm^{-2}year^{-1} for present-day (PD, top, left) and projected future (RCP85, top, right) conditions following the RCP8.5 scenario. The bottom panel shows the differences of projected future minus present-day BC aerosol emission fluxes caused by wildfires.

6.1.2 BC aerosol deposition fluxes resulting from wildfires simulated with ECHAM6-HAM2.2

The wildfire BC aerosol emissions simulated with JSBACH-SPITFIRE serve as input data for the atmospheric general circulation model ECHAM6 (Stevens et al., 2013) including the aerosol module HAM2.2 (Stier et al., 2005; Zhang et al., 2012) to simulate BC aerosol deposition fluxes from wildfires. The model setup is described in detail in Veira et al. (2015b). Both the model version and the model setup slightly differ from the ACCMIP-setup based on Lamarque et al. (2010) used for the simulations described in section 2.3. The differences are outlined in the following:

- The ECHAM6-HAM2.2 model has been extended by a semi-empirical plume height parameterization to account for wildfire emission heights. Here, wildfire plume heights depend among other parameters on the fire radiative power (FRP) and wildfire emissions are vertically distributed with constant mass mixing ratios ranging from the surface to the top of the plume. For a detailed description of the wildfire emission height parameterization see Veira et al. (2015a). The changes in the emission height parameterization influence the vertical atmospheric distribution of the BC aerosols, in turn influencing the spatial distribution of the BC aerosol deposition fluxes. Veira et al. (2015b) has shown that the semi-empirical plume height parameterization increases the BC aerosol lifetime compared to the ECHAM6-HAM2 standard model and increases slightly the deposition fluxes north of 30°N.
- Anthropogenic and biogenic BC aerosol emissions are prescribed according to the emission inventory AeroCom phase II, which are based on Lamarque et al. (2010) as in the ACCMIP-setup (section 2.2). The wildfire BC aerosol emissions are instead taken from the JSBACH-SPITFIRE simulations as described in section 6.1.1. As these wildfire BC aerosol emissions were multiplied with a correction factor of 3.4, these emissions are with 7.43 Tgyear^{-1} significantly higher than the BC aerosol emissions used in AeroCom phase II.

For the simulations ECHAM6-HAM2.2 was used in the horizontal resolution T63 (1.875° x 1.875°) with 47 vertical layers (spanning from the surface up to 0.01 hPa) and a time step of 10 minutes, which is the same model setup used for the simulations with the ACCMIP-setup as described in section 2.2.

The present-day and projected future BC aerosol deposition fluxes which were simulated with ECHAM6-HAM2.2 in various settings are described in the following and are summarized in Table 6.1. Note that the experiments are named differently in Veira et al. (2015b).

- The BC aerosol deposition fluxes $\mathbf{DEP\_PD}_{fire}$ result from ECHAM6-HAM2.2 simulations accounting for present-day climate conditions, present-day anthropogenic as well as present-day wildfire BC aerosol emissions. The BC aerosol deposition fluxes $\mathbf{DEP\_PD}_{nofire}$ result from the same setup, but excluding BC aerosol emissions from wildfires.

- The BC aerosol deposition fluxes **DEP_RCP85**$_{fire}$ result from ECHAM6-HAM2.2 simulations accounting for projected future climate conditions, present-day anthropogenic as well as projected future wildfire BC aerosol emissions. The BC aerosol deposition fluxes **DEP_RCP85**$_{nofire}$ result from the same setup, but excluding BC aerosol emissions from wildfires. Projected future conditions follow the RCP8.5 scenario.

- The BC aerosol deposition fluxes **DEP_aRCP85**$_{fire}$ result from ECHAM6-HAM2.2 simulations accounting for projected future climate conditions, projected future anthropogenic as well as projected future wildfire BC aerosol emissions. The BC aerosol deposition fluxes **DEP_aRCP85**$_{nofire}$ result from the same setup, but excluding BC aerosol emissions from wildfires. Projected future conditions follow the RCP8.5 scenario.

The wildfire BC aerosol deposition fluxes equal the differences of the DEP$_{fire}$ and the DEP$_{nofire}$ BC aerosol deposition fluxes and are given in Table 6.1 as **DEP_PD**$_{wildfire}$ for present-day and **DEP_RCP85**$_{wildfire}$ for projected future conditions.

On a global scale, the resulting present-day BC aerosol deposition fluxes including wildfire emissions (DEP_PD$_{fire}$) sum up to about 12.65 Tgyear^{-1} yielding about 59 % higher BC aerosol deposition fluxes compared to the BC aerosol deposition fluxes from the simulation excluding wildfires (DEP_PD$_{nofire}$) which sum up to about 5.22 Tgyear^{-1}. The difference in these deposition fluxes represents the contribution of wildfires to the global total BC aerosol deposition accounting for about 7.43 Tgyear^{-1} (DEP_PD$_{wildfire}$) for present-day conditions. In the Arctic region (60°N-90°N), the wildfire BC aerosol deposition accounts for about 0.22 Tgyear^{-1} for the present-day period.
Assuming projected future climate and future JSBACH-SPITFIRE BC aerosol emission fluxes following the RCP8.5 scenario combined with present-day anthropogenic BC aerosol emissions (DEP_RCP85$_{fire}$) results in about 13.10 Tgyear^{-1} global total BC aerosol deposition. Compared to present-day conditions (DEP_PD$_{fire}$), the projected future BC aerosol deposition fluxes are about 4 % higher (13.10 compared to 12.65 Tgyear^{-1}). The difference of the DEP_RCP85$_{fire}$ and DEP_RCP85$_{nofire}$ the BC aerosol deposition fluxes provides the global total BC aerosol deposition caused by wildfires for projected future conditions, summing up to about 7.87 Tgyear^{-1} (DEP_RCP85$_{wildfire}$). The global total wildfire BC aerosol deposition fluxes increase by about 6 % from present-day to projected future conditions. For the Arctic region, the global total BC aerosol deposition fluxes induced by wildfires increase even by about 91 % from present-day to projected future conditions (0.22 compared to 0.42 Tgyear^{-1}).
Considering projected future climate and wildfire BC aerosol emission fluxes following the RCP8.5 scenario and in addition accounting also for projected future anthropogenic BC aerosol emission fluxes following the RCP8.5 scenario (DEP_aRCP85$_{fire}$), the global total BC aerosol deposition adds up to about 10.36 Tgyear^{-1}. The decrease of about 21 % in the global total BC aerosol deposition from 13.10 Tgyear^{-1} (DEP_RCP85$_{fire}$) to 10.36 Tgyear^{-1} (DEP_aRCP85$_{fire}$) is the difference in the anthropogenic emissions for present-day and projected future conditions (5.22 compared

Table 6.1: Global total (left) as well as total Arctic (60°N-90°N, right) BC aerosol deposition fluxes and standard deviations in Tgyear^{-1} as simulated in different experiments for present-day and projected future conditions. Projected future conditions follow the RCP8.5 scenario. Shown are averages over ten simulation years. The *wildfire* contribution equals the difference of the *fire* and the *nofire* BC aerosol deposition fluxes. The setup of the single experiments is described in detail in the main text (section 6.1.2).

Deposition	**Total BC aerosol deposition [Tgyear^{-1}]**	
	Global	**Arctic**
DEP_PD$_{fire}$	12.65 ± 0.32	0.38 ± 0.03
DEP_PD$_{nofire}$	5.22 ± 0.01	0.16 ± 0.01
DEP_PD$_{wildfire}$	7.43	0.22
DEP_RCP85$_{fire}$	13.10 ± 0.44	0.59 ± 0.06
DEP_RCP85$_{nofire}$	5.23 ± 0.01	0.17 ± 0.01
DEP_aRCP85$_{fire}$	10.36 ± 0.01	0.45 ± 0.00
DEP_aRCP85$_{nofire}$	2.49 ± 0.44	0.03 ± 0.04
DEP_RCP85$_{wildfire}$	7.87	0.42

to 2.49 Tgyear^{-1}). The difference of the DEP_aRCP85$_{fire}$ and DEP_aRCP85$_{nofire}$ BC aerosol deposition fluxes equals DEP_RCP85$_{wildfire}$, as the same projected future wildfire deposition fluxes were taken into account.

6.2 Experimental design

This section summarizes the performed simulations to assess the effect of the deposition of wildfire-related BC aerosols on land covered snow surfaces for present-day and projected future conditions following the RCP8.5 for the end of the 21st century.

To isolate the effect of BC aerosol contamination of snow related to wildfires on climate for present-day and projected future conditions, the simulations summarized in Table 6.2 were performed with ECHAM6 including the implemented snow-albedo-scheme as described in section 2.3. Note that BC aerosol deposition fluxes resulting from wildfires are taken from the SPITFIRE-setup (section 6.1.2).

In the present analysis the impact of BC aerosols deposited on snow related to wildfire BC aerosol emissions is derived from the difference of a simulation in which the deposition fluxes caused by all BC aerosol emission sources are taken into account and a simulation in which wildfire BC aerosol emissions were excluded. Alternatively, the impact of BC aerosol deposition related to wildfire emissions could have been derived from single simulations forced by the BC aerosol deposition flux caused by wildfires, which equals the difference of the BC aerosol deposition fluxes with and without accounting for wildfire BC aerosol emissions. As the mixing of BC aerosols into snow is, however, a non-linear process depending on the snowfall and BC aerosol deposition fluxes, the design of the simulations was chosen with minimum deviations from the

Table 6.2: Setup of the single ECHAM6 simulations to isolate the effect of BC aerosol contamination of snow caused by wildfire BC aerosol emissions on climate. Here, the climate and BC aerosol deposition fluxes (anthropogenic as well as from wildfires) are prescribed as boundary conditions for present-day (PD, 2000-2009) and projected future conditions following the Representative Concentration Pathway 8.5 (RCP85, 2090-2099) in different combinations. Wildfire BC aerosol emissions are taken from former JSBACH-SPITFIRE simulations.

Experiment	**Climate**	**BC aerosol deposition**		**Time period**
		anthropogenic	**wildfire**	
PD_{fire}	PD	PD	SPITFIRE PD	1996-2005
PD_{nofire}	PD	PD	off	1996-2005
$RCP85_{fire}$	RCP8.5	PD	SPITFIRE RCP8.5	2090-2099
$RCP85_{nofire}$	RCP8.5	PD	off	2090-2099
$aRCP85_{fire}$	RCP8.5	RCP8.5	SPITFIRE RCP8.5	2090-2099
$aRCP85_{nofire}$	RCP8.5	RCP8.5	off	2090-2099
$Climate_{only}$	RCP8.5	PD	SPITFIRE PD	2090-2099

real state. For the present study this is achieved by taking the difference between a simulation using deposition with and without wildfires, rather than isolating the wildfire impact already for the BC aerosol deposition fields.

For the present-day period covering 1996-2005, two simulations accounting for present-day climate as well as present-day anthropogenic BC aerosol deposition fluxes are performed: The PD_{fire} simulation also includes prescribed BC aerosol deposition fluxes induced by wildfires. The PD_{nofire} simulation does not consider wildfire BC aerosol deposition. The effect of the darkening of the snow by wildfire-related BC aerosols deposited on snow for present-day conditions is determined by the difference of both simulations (PD_{fire}-PD_{nofire}).
The same proceeding is conducted for the projected future time period (2090-2099): Accounting for present-day anthropogenic BC aerosol deposition fluxes as well, but projected future climate conditions following the RCP8.5, the $RCP85_{fire}$ simulation is performed with prescribed projected future wildfire BC aerosol deposition fluxes following the RCP8.5. In contrast, the $RCP85_{nofire}$ simulation does not account for wildfire BC aerosol deposition fluxes. The difference of the two simulations ($RCP85_{fire}$-$RCP85_{nofire}$) results in the effect of the contamination of snow by projected future wildfire BC aerosol deposition fluxes combined with projected future climate.
To further assess the contribution of future anthropogenic BC aerosol emissions following the RCP8.5 on the effect of the darkening due to BC contamination of snow for projected future conditions, two additional simulations were performed: The $aRCP85_{fire}$ simulation also accounts for projected future climate conditions and projected future wildfire deposition fluxes following the RCP8.5 like the $RCP85_{fire}$ simulation, but accounts in addition for projected future anthropogenic BC aerosol deposition fluxes following the RCP8.5. The same setup is used for the $aRCP85_{nofire}$ simulation, but excluding wildfire BC aerosol deposition fluxes. The difference of the $aRCP85_{fire}$ and the $aRCP85_{nofire}$ simulations quantifies the effect of the deposition

of BC aerosols on snow related to wildfires accounting for projected future changes in climate, in wildfire BC aerosol deposition fluxes, as well as in anthropogenic BC aerosol deposition fluxes.
In addition, the Climate$_{only}$ simulation is performed, to disentangle the changes on the effect of snow darkening by the deposition of wildfire-related BC aerosols only arising from changes in climate when compared to the PD$_{fire}$ simulation. Here, projected future climate following the RCP8.5 scenario is combined with both present-day anthropogenic and wildfire BC aerosol deposition fluxes.

6.3 Impact of present-day wildfire BC aerosols deposited on snow

This section summarizes the effect of present-day (1996-2005) BC aerosol deposition fluxes related to wildfires on BC concentrations in snow as well as the corresponding changes in the total surface albedo. The model setup used to investigate the effect of wildfire related BC aerosol deposition fluxes on snow differs from the model setup used to investigate the effect of BC contamination of snow including all BC aerosol emission sources described in chapter 3. In order to be able to relate the results of the different model setups, first, BC aerosol deposition fluxes and BC concentrations in snow resulting from all BC aerosol emission sources applied in the two different model setups are compared, before the wildfire impact is analysed in more detail. The model setup applied in chapter 3 is referred to as the ACCMIP-setup and the model setup used to investigate the effect of wildfire BC aerosol emissions as the SPITFIRE-setup.

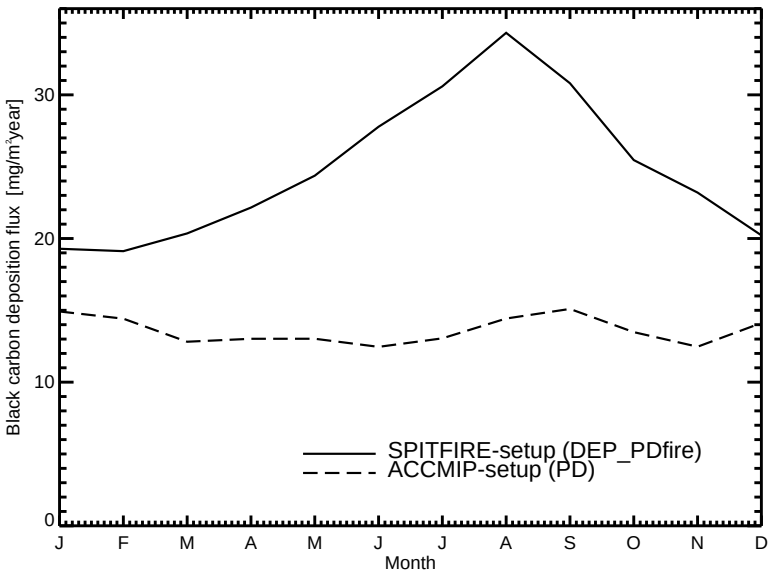

Figure 6.2: Present-day global monthly mean BC aerosol deposition fluxes in mgm^{-2}year^{-1} averaged over ten simulation years. Shown are the present-day BC aerosol deposition fluxes including all BC emission sources for the ACCMIP-setup (PD) as well as for the SPITFIRE-setup (DEP_PD$_{fire}$), respectively.

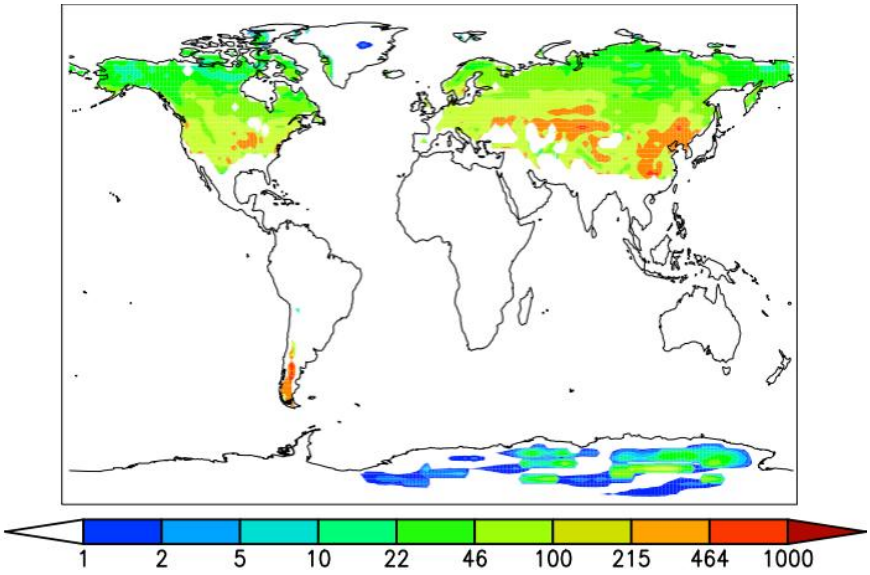

Figure 6.3: Present-day BC concentrations in snow resulting from all emission sources including wildfires in ng(BC)g(snow)$^{-1}$ as simulated with ECHAM6 with prescribed ECHAM6-HAM2.2 BC aerosol deposition fields from the SPITFIRE-setup. Shown are BC concentrations in snow for snow depths exceeding 1 mm averaged over ten simulation years.

Present-day BC aerosol deposition fluxes applied in the SPITFIRE-setup (DEP_PD$_{fire}$) lead to about 71 % higher global total BC aerosol deposition fluxes when compared to the ACCMIP-setup (12.65 compared to 7.41 Tgyear^{-1}). Higher BC aerosol deposition fluxes in the SPITFIRE-setup are a result of higher wildfire BC aerosol emissions, which were multiplied by a correction factor of 3.4 to better match observational data (see section 6.1.1). The seasonal cycle differs between the two model setups as shown in Figure 6.2. The solid line simulated with the SPITFIRE-setup accounting for all emission sources shows a pronounced seasonal cycle of the BC aerosol deposition fluxes with increasing BC aerosol deposition fluxes over the spring and the summer season peaking in August and decreasing in autumn showing lowest BC aerosol deposition fluxes in the winter season. In contrast, the seasonal cycle as simulated with the ACCMIP setup (dashed line) shows a more smooth development with little variations of the monthly mean BC aerosol deposition fluxes. The stronger seasonality in the wildfire setup is thereby a direct response to the higher wildfire BC aerosol emissions, which exhibit a strong seasonal cycle.

The distribution of the BC concentrations in snow resulting from the BC aerosol deposition fluxes as simulated in the SPITFIRE-setup (PD$_{fire}$) is shown in Figure 6.3. Compared to the present-day simulation (PD, top panel of Figure 3.5 in chapter 3) obtained with the ACCMIP-setup, the resulting BC concentrations in snow show very similar patterns of BC concentrations in snow. As a direct consequence of higher BC aerosol deposition fluxes, the BC concentrations in snow are higher for the SPITFIRE-setup. The global mean BC concentrations in snow averaged only for snow depths exceeding 1 mm almost double (100.87 compared to 44.98 ng(BC)g(snow)$^{-1}$ between the SPITFIRE-setup and the ACCMIP-setup. Compared to the BC concentrations in

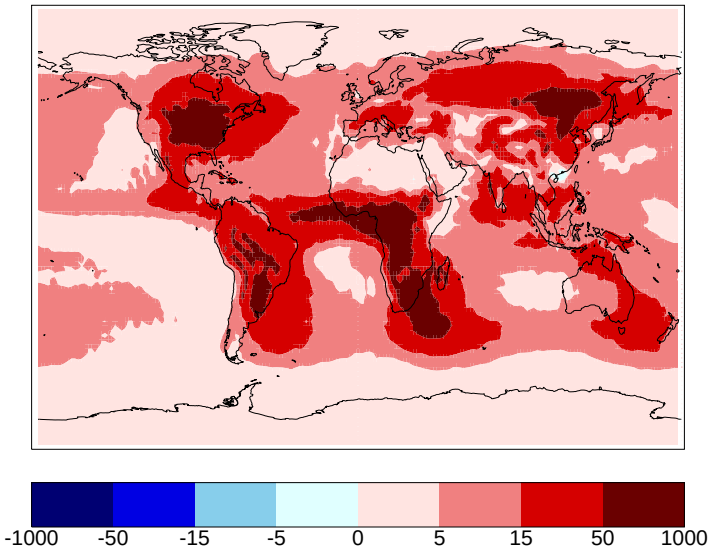

Figure 6.4: Present-day wildfire BC aerosol deposition fluxes in $mgm^{-2}year^{-1}$ as simulated with ECHAM6-HAM2.2 from the SPITFIRE-setup averaged over ten simulation years. Wildfire BC aerosol deposition fluxes are shown as the difference of BC aerosol deposition fluxes from a simulation accounting for all BC aerosol emission sources (PD_{fire}) minus a simulation excluding wildfire BC aerosol emissions (PD_{nofire}).

snow as simulated in Flanner et al. (2007) (chapter 3, bottom panel in Figure 3.5), the higher BC concentrations in snow as simulated with the SPITFIRE-setup are in better agreement with the ACCMIP-setup.
Regarding the resulting reductions in the total surface albedo due to the BC concentrations in snow, the PD_{fire} simulation of the SPITFIRE-setup for the present-day time period shows global averaged total surface albedo reductions of about -0.000598. These albedo reductions are about a factor 5 higher compared to the total surface albedo reductions of -0.00011 resulting from the PD simulation obtained with the ACCMIP-setup which are described in detail in section 3.3.

Figure 6.4 shows present-day wildfire related BC aerosol deposition fluxes averaged over ten simulation years in $mgm^{-2}year^{-1}$ resulting from the SPITFIRE-setup. The wildfire BC aerosol deposition fluxes result from differences between the simulation including all sources of BC aerosols also accounting for wildfires (PD_{fire}) and the simulation PD_{nofire} including all BC aerosol sources as well but neglecting emissions from wildfires which are described in section 6.1.2. On the global annual mean these wildfire BC aerosol deposition fluxes amount to about 7.43 $Tgyear^{-1}$. High wildfire BC aerosol deposition fluxes are found close to the major wildfire BC aerosol sources in the Southern Hemisphere in the tropical regions e.g. all over the southern part of Africa as well as South America. In the Northern Hemisphere, patterns of high wildfire BC aerosol deposition fluxes are found in the south-eastern part of Russia and in Mongolia, as well as in the Eastern part of North America. Note here that BC aerosol deposition fluxes can potentially be reduced even though wildfire BC aerosol emissions are increasing. For the simulations analysed reduced BC aerosol deposition fluxes are found in a small region in the south-eastern part of China. This can be explained by non-linear interactions of different aerosol types in the aerosol microphysical scheme

HAM, in which for example the BC aerosol deposition fluxes depend on coagulation with other aerosols or the condensation of sulphate on existing aerosols.
The BC concentrations in snow related to wildfires obtained from the difference of the PD_{fire} minus the PD_{nofire} simulation sum up to about 13.32 ng(BC)g(snow)$^{-1}$ for present-day conditions.

The present-day reductions in the total surface albedo resulting from the BC concentrations in snow that can be attributed to wildfires are shown in the top panel in Figure 6.5. The total surface albedo reductions equal the differences in the total surface albedo between the PD_{fire} (-0.000598) minus the PD_{nofire} (-0.000311) simulation. On the global annual mean the total surface albedo is reduced by about -0.000287 due to wildfires. The total surface albedo reductions exhibit a strong seasonal cycle, with lowest total surface albedo reductions in the summer months June and July, followed by an increase in the total surface albedo reductions until the maximum total surface albedo reductions are reached in November, and decreasing in the spring season. Note that the total surface albedo reductions caused by wildfires drop in December. Re-

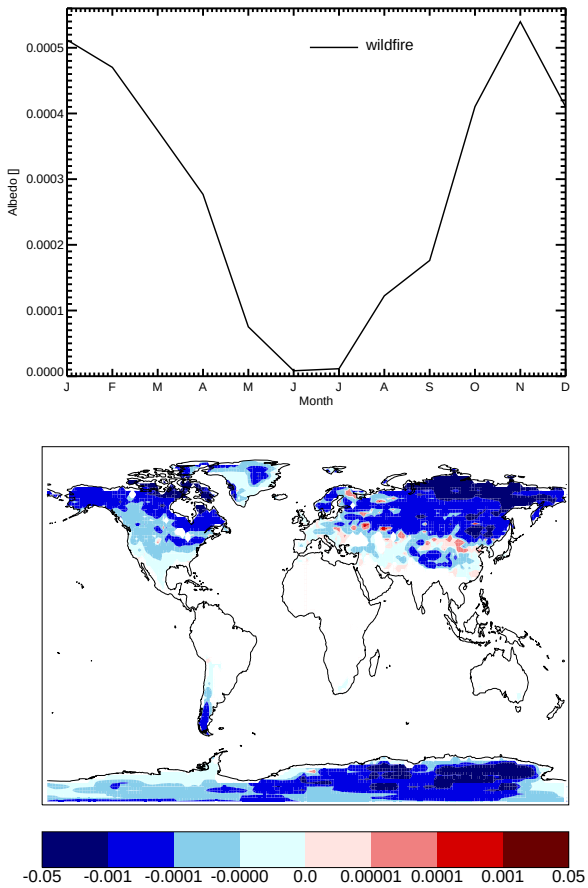

Figure 6.5: Present-day total surface albedo changes resulting from BC contamination of snow related to wildfires as a difference of the simulations PD_{fire}-PD_{nofire} Top: Monthly mean of the total surface albedo reductions averaged over ten simulation years. Bottom: Global distribution of the differences in the total surface albedo between the PD_{fire} and the PD_{nofire} simulation, providing total surface albedo changes caused by wildfires.

garding the spatial distribution in the total surface albedo reductions in Figure 6.5 in the bottom panel, a decrease in the total surface albedo is found especially in the northern parts of Siberia and Canada, the eastern parts of Mongolia and the Antarctic. However, in some smaller regions the wildfire BC aerosol deposition fluxes cause an increase in the total surface albedo e.g. around China and eastern Europe. Overall, the present-day total surface albedo is most sensitive to BC aerosol deposition on snow resulting from wildfires in the northern high latitudes and the Antarctic.

6.4 Differences in present-day and future wildfire BC aerosol deposition on BC concentrations in snow and albedo changes

In the following is analysed, how wildfire BC aerosols deposited on snow impact BC concentrations in snow and the total surface albedo for present-day and projected future conditions. Here, the focus lies on future conditions following the RCP8.5 projection.

The global total annual mean wildfire BC aerosol deposition fluxes for the projected future time period following the RCP8.5 scenario are about 6 % higher than compared to the BC aerosol deposition fluxes for present-day conditions (7.87 compared 7.43 Tgyear^{-1}). Although the global total amount of BC aerosol deposition fluxes does not differ considerably between the two time periods, the global distribution of the differences between future and present-day BC aerosol deposition fluxes is shifted strongly (Figure 6.6 a, b). While the projected future BC aerosol deposition fluxes show a pronounced decrease in the tropical and subtropical regions, e.g. in Africa, the northern part of South America, over India as well as Australia, an increase in the BC aerosol deposition fluxes is found, especially over North America as well as in the boreal regions over Eurasia and the southern part of South America. The differences in the BC aerosol deposition fluxes, thereby, closely follow the differences in wildfire BC aerosol emission fluxes (see section 6.1.1).
The simulated future snow cover following the RCP8.5 projection shows a retreat towards the northern regions compared to present-day conditions. Less snow cover is found almost all over the globe for projected future conditions compared to present-day. The decrease in the future snow cover is especially pronounced in the north-western part of Eurasia, the eastern coast of North America as well as in the region around the Tibetan Plateau. Also shown are some small-area patterns of increasing future snow cover compared to present-day conditions in north-eastern Siberia, around the Tibetan Plateau and in the southern part of North America (Figure 6.6 c, d).
The resulting projected BC concentrations in snow related to wildfires and the differences to present-day conditions are shown in Figure 6.6 (e, f). Wildfire BC concentrations in snow are obtained from the differences of the RCP85$_{fire}$ and the RCP85$_{nofire}$ simulations. The projected future BC concentrations in snow resulting from wildfires show high concentrations in the boreal regions e.g. in Mongolia and

eastern parts of Russia as well as in North America. The BC concentrations in snow related only to wildfires sum up to about 13.59 ng(BC)g(snow)$^{-1}$, leading to about 2 % higher BC concentrations in snow compared to present-day conditions (13.59 compared to 13.32 ng(BC)g(snow)$^{-1}$). However, also lower BC concentrations in snow are found e.g. in China due to the non-linear dependency of the BC concentrations in snow on the snowfall, as well as changes in the BC aerosol long-range transport due to different BC aerosol concentrations in the atmosphere between the RCP85$_{fire}$ and the RCP85$_{nofire}$ simulation. The global distribution of the differences between projected future and present-day BC concentrations in snow show a non-linear behaviour as a result of combined changes in the snow cover and changes in the BC aerosol deposition fluxes between the two time periods. Higher BC concentrations in snow for the projected future time period are shown e.g. in the western part of North America and in Russia.

Regarding the changes in the projected future total surface albedo due to wildfires, which are obtained from the differences of the RCP85$_{fire}$ and the RCP85$_{nofire}$ simulations, as shown in Figure 6.6 (g, h), in general reductions in the total surface albedo are found. These total surface albedo reductions are especially pronounced in the northern part of Eurasia and northern North America as well as in the Antarctic. Compared to present-day conditions, the total surface albedo reductions related to wildfires are higher for projected future conditions in large parts of Eurasia, especially around the Taymyr Peninsula, and the eastern part of North America as well as in some parts in the Antarctic.

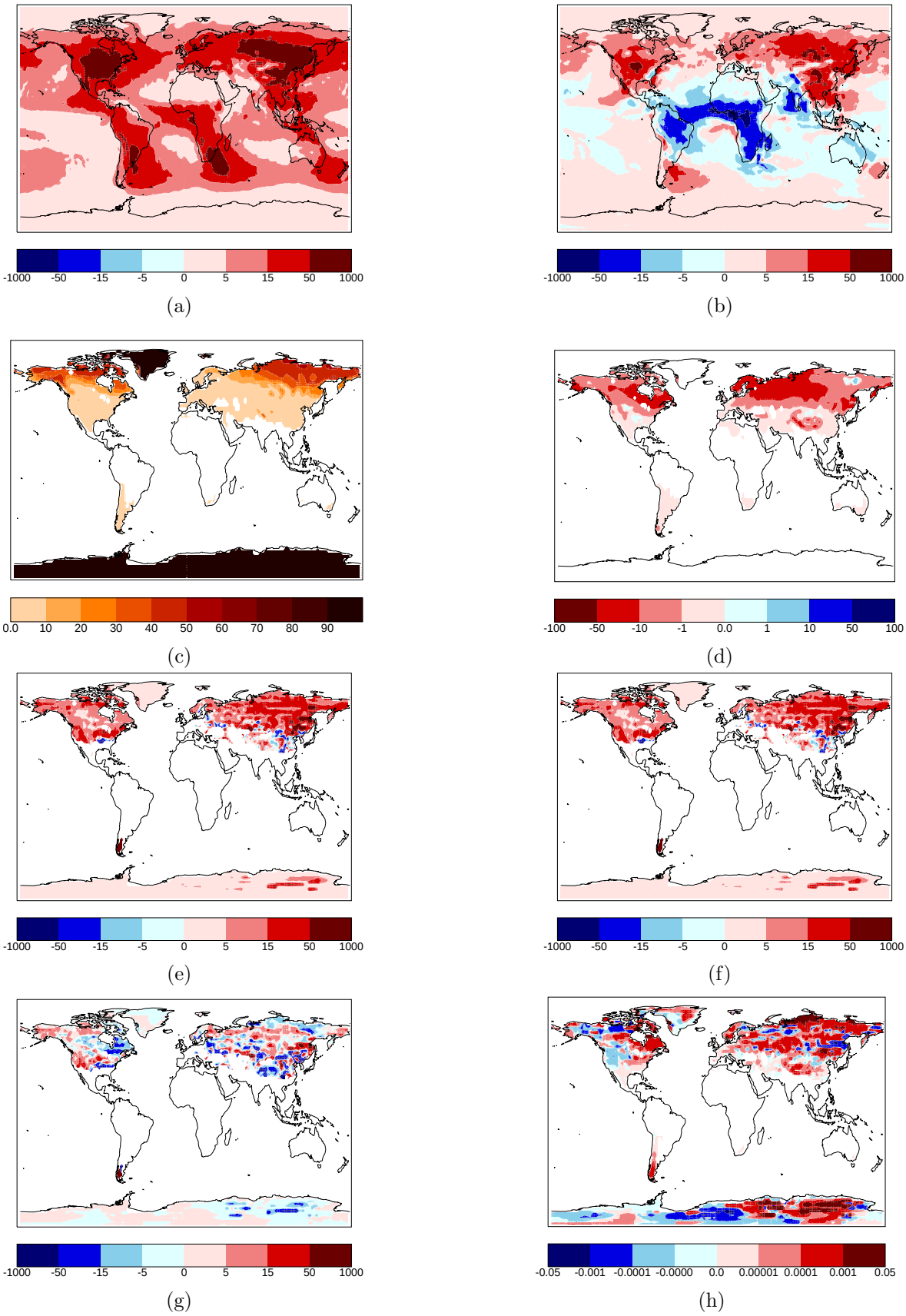

Figure 6.6: BC aerosol deposition fluxes [$mgm^{-2}year^{-1}$] (a, b), snow cover [%] (c, d), BC concentrations in snow [$ng(BC)g(snow)^{-1}$] (e, f), and total surface albedo changes [/] (g, h) related to wildfires for projected future conditions following the RCP8.5 scenario (left) as well as the differences of future minus present-day conditions (right).

6.5 Impact of present-day and future BC aerosols deposited on snow emitted from wildfires on the radiation

This section summarizes the effect of present-day and projected future wildfire related BC aerosols deposited on land-based snow on the radiative forcing. For this purpose, the instantaneous radiative forcing is determined following the definition of the Fifth Assessment Report of the Intergovernmental Panel on Climate Change (Myhre et al., 2013b) as described in section 3.4.

Figure 6.7 summarizes the instantaneous radiative forcing for the top of the atmosphere (TOA) and total-sky conditions induced by BC aerosol deposition on land-based snow for present-day conditions on the left and projected future conditions on the right following the RCP8.5 scenario for the end of the 21st century.
Regarding the present-day period, the patterns of high instantaneous radiative forcing are similar for the PD$_{nofire}$ and the PD$_{fire}$ simulation which are located in the eastern part of North America, northern China and Mongolia, the Tibetan Plateau, Russia and the Antarctic (Figure 6.7 (left)). For the PD$_{fire}$ simulation including wildfire BC aerosol emissions, the patterns are even more pronounced for the northern part of Eurasia, especially in Siberia, as well as over Greenland and the Antarctic compared to the PD$_{nofire}$ simulation. Local instantaneous radiative forcing reaches maximum values of up to 1.86 Wm^{-2} for the PD$_{nofire}$ simulation and even up to 5.76 Wm^{-2} for the PD$_{fire}$ simulation.
The instantaneous radiative forcing resulting from wildfires is shown as the difference of the PD$_{fire}$ simulation minus the PD$_{nofire}$ simulation in the bottom panel on the left in Figure 6.7. Overall, a positive instantaneous radiative forcing of wildfire related BC aerosol deposition on snow is found for the present-day period. The wildfire instantaneous radiative forcing is especially pronounced in the Antarctic and in the northern parts of Canada as well as in the boreal regions in north-eastern Siberia. In addition, the instantaneous radiative forcing from wildfires is also pronounced in mountainous regions like the Tibetan Plateau. Locally, the instantaneous radiative forcing from wildfires reaches maximum values of up to 3.91 Wm^{-2}. Some spots of negative instantaneous radiative forcing are found for wildfire related BC aerosol emissions e.g. around China and in southern Europe. The negative instantaneous radiative forcing values coincide with reduced BC aerosol deposition fluxes introduced by altered wildfire emissions, which are related to non-linear interactions in the aerosol microphysical scheme (see section 6.3).

For the projected future time period following the RCP8.5 scenario (Figure 6.7, right), the spatial patterns of high instantaneous radiative forcing are distributed similarly compared to the patterns resulting from the present-day simulations. In general, the instantaneous radiative forcing for the projected future conditions is lower compared to the present-day forcing reaching local maximum values of about 1.18 Wm^{-2} for the RCP85$_{nofire}$ simulation and about 3.34 Wm^{-2} for the RCP85$_{fire}$ simulation. The instantaneous radiative forcing increases e.g. in north-eastern Siberia,

northern Canada, Greenland and the Antarctic from the RCP85$_{nofire}$ to the RCP85$_{fire}$ simulation.
The same patterns of the projected future instantaneous radiative forcing are also shown for the instantaneous radiative forcing related to projected future wildfires. For projected future conditions, the instantaneous radiative forcing from wildfires is most pronounced in north-eastern Siberia, northern Canada and the Antarctic. On a local scale, the instantaneous radiative forcing resulting from wildfires for projected future conditions reaches a maximum value of about 2.30 Wm^{-2}.

The global mean instantaneous radiative forcing for the single experiments are summarized in Table 6.3 as annual (ANNUAL) and seasonal means (DJF, MAM, JJA, SON), respectively.
The instantaneous radiative forcing as simulated in the SPITFIRE-setup for the present-day time period considering all BC aerosol emission sources (PD$_{fire}$) is about 60 % higher compared to the present-day forcing simulated with the ACCMIP-setup (PD) described in section 3.4 (10.74 compared to 6.69 mWm^{-2}). The higher instantaneous radiative forcing applying the SPITFIRE-setup results from the tuning of the wildfire emissions against observational data by a correction factor as described in section 6.1.1, leading to increased wildfire BC aerosol emissions and thus total BC aerosol emissions.

The instantaneous radiative forcing caused by wildfire BC aerosols deposited on snow is about 5.46 mWm^{-2} for present-day conditions and decreases by about 42 % to 3.14 mWm^{-2} for projected future conditions. For both time periods, the instantaneous radiative forcing related to wildfire BC aerosol emissions is largest in the winter season DJF (11.48 mWm^{-2} for present-day and 7.07 mWm^{-2} for projected future conditions). The lower instantaneous radiative forcing for the projected future conditions following the RCP8.5 compared to present-day results from a combination of changes in wildfire BC aerosol deposition fluxes and changes in snow cover. The increase in wildfire BC aerosol deposition fluxes in the extratropical regions is thereby outweighed by a decrease in snow covered land areas under RCP8.5 conditions, leading overall to a reduction of the projected future instantaneous radiative forcing. Compared to the instantaneous radiative forcing caused by all BC aerosol emission sources (PD$_{fire}$ and RCP85$_{fire}$, respectively) wildfires contribute about 50 % for present-day conditions and about 57 % for projected future RCP8.5 conditions. The contribution of wildfires to the overall instantaneous radiative forcing is thereby highest in autumn (SON) with about 64 % for present-day conditions and about 67 % for projected future conditions. That wildfires contribute stronger to the total radiative forcing in the projected future following the RCP8.5 conditions is a direct consequence of higher BC aerosol deposition fluxes in the extratropics. The lowest instantaneous radiative forcing related to wildfire BC aerosol deposition on snow covered surfaces occurs in the summer season JJA for present-day (0.21 mWm^{-2}) as well as projected future conditions (0.19 mWm^{-2}).

Table 6.4 summarizes the instantaneous radiative forcing of snow darkening caused by the deposition of BC aerosols on snow for the Arctic region (60°N-90°N) for

present-day as well as projected future conditions. Compared to the global scale, the Arctic instantaneous radiative forcing accounting for all BC aerosol emission sources almost doubles for present-day (10.74 compared to 19.74 mWm^{-2}) and projected future (5.53 compared to 9.68 mWm^{-2}) conditions. For the Arctic, the present-day instantaneous radiative forcing caused by wildfire BC aerosol deposition on snow is about 12.55 mWm^{-2}, decreasing for projected future conditions by about 56 % to 7.07 mWm^{-2}. The contribution of wildfires to the total Arctic instantaneous radiative forcing is higher than on the global scale. For present-day conditions, wildfire emissions account for about 64 % of the Arctic radiative forcing, whereas the contribution to the projected future Arctic total instantaneous radiative forcing resulting from wildfires increases compared to present-day conditions to about 73 %. Overall, the contribution to the total Arctic instantaneous radiative forcing from wildfires is larger for all seasons than the contribution of anthropogenic BC aerosol emissions for present-day as well as for the projected future conditions. Here, the largest contribution to the total Arctic instantaneous radiative forcing from wildfires is found in the autumn season SON where present-day wildfires contribute to about 70 % and the projected future wildfires contribute even to about 81 %. In general, the largest instantaneous radiative forcing resulting from the deposition of BC aerosols in Arctic snow is found in the spring season with present-day wildfire emissions only accounting for about 30.96 mWm^{-2} and projected future wildfire emissions add to about 16.17 mWm^{-2}.

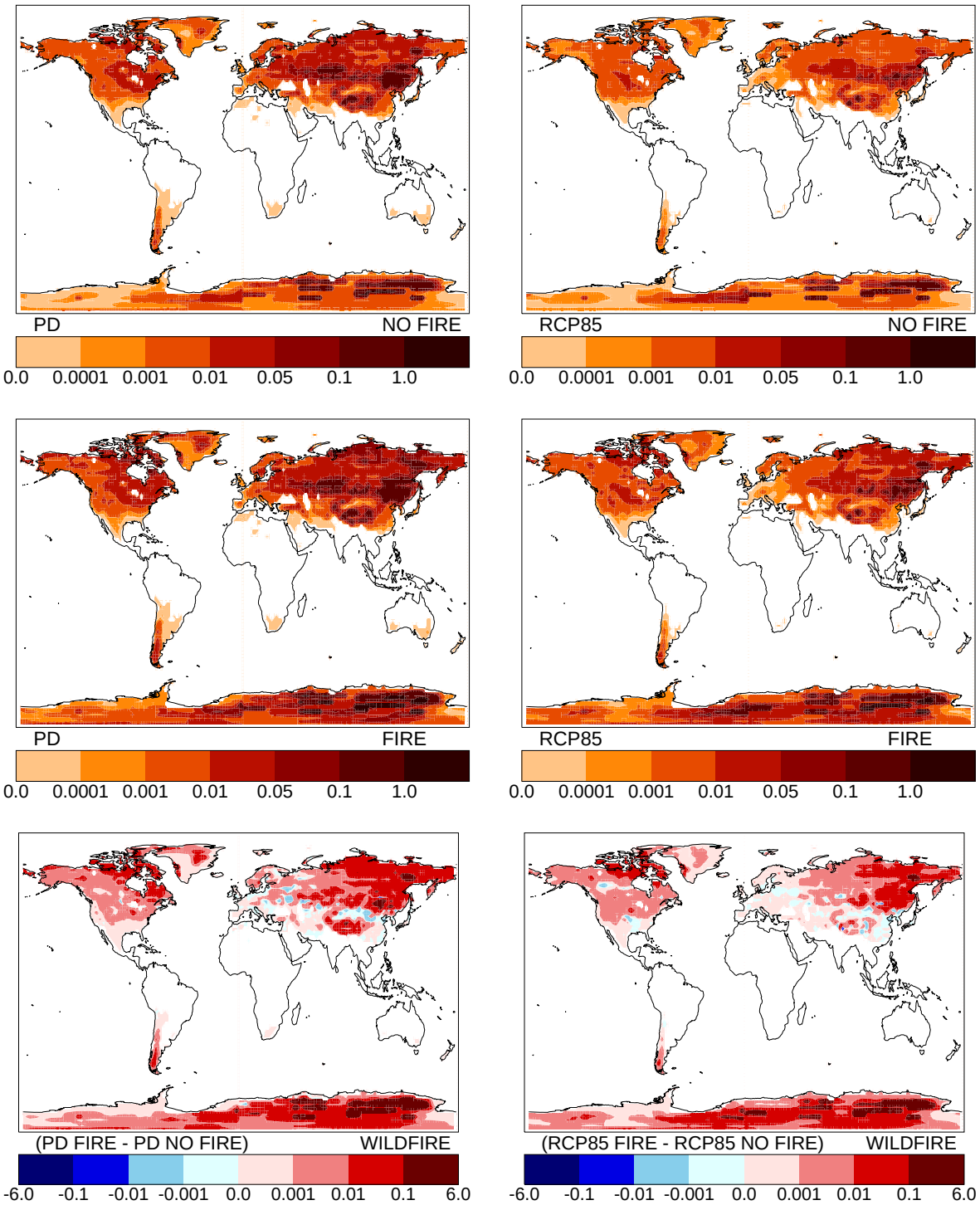

Figure 6.7: Present-day (left) and projected future (right) instantaneous radiative forcing averaged over ten simulation years [mWm^{-2}]. The top panels show the instantaneous radiative forcing of BC aerosol contamination of snow for the simulations including all BC aerosol emission sources except wildfires (PD$_{nofire}$, RCP85$_{nofire}$), the panels in the middle show the simulations including all sources of BC aerosols accounting for SPITFIRE wildfire emissions (PD$_{fire}$, RCP85$_{fire}$), the bottom panels show the differences of the simulations including and excluding wildfire BC emissions providing the instantaneous radiative forcing resulting from wildfires only (PD$_{fire}$ - PD$_{nofire}$, RCP85$_{fire}$ - RCP85$_{nofire}$).

Table 6.3: Global present-day (PD, 1996-2005), and projected future (RCP85, 2090-2099) instantaneous radiative forcing and standard deviations in mWm^{-2} (total-sky) from the deposition of BC aerosols on land-based snow from all BC aerosol emission sources except wildfires (PD_{nofire}, $RCP85_{nofire}$) and from all emission sources including SPITFIRE wildfire emissions (PD_{fire}, $RCP85_{fire}$). The contribution from wildfires (PD_{WF}, $RCP85_{WF}$) is the difference of PD_{fire}-PD_{nofire} and $RCP85_{fire}$-$RCP85_{nofire}$, respectively. Shown are averages over ten simulation years, as annual (ANNUAL) and seasonal means (DJF, MAM, JJA, and SON) for the surface (SUR) as well as for the top of the atmosphere (TOA).

RF [$\mathbf{mWm^{-2}}$]	**Global**		
	PD_{fire}	PD_{nofire}	PD_{WF}
ANNUAL (SUR)	11.22 ± 7.01	5.53 ± 2.59	5.68 ± 4.55
ANNUAL (TOA)	10.74 ± 6.77	5.28 ± 2.50	5.46 ± 4.39
DJF	24.75 ± 16.42	13.27 ± 6.14	11.48 ± 10.68
MAM	8.47 ± 2.66	4.41 ± 1.43	4.06 ± 1.54
JJA	0.31 ± 0.23	0.10 ± 0.08	0.21 ± 0.16
SON	9.45 ± 8.04	3.37 ± 2.74	6.08 ± 5.31
	$RCP85_{fire}$	$RCP85_{nofire}$	$RCP85_{WF}$
ANNUAL (SUR)	5.80 ± 5.26	2.51 ± 1.86	3.29 ± 3.40
ANNUAL (TOA)	5.53 ± 5.04	2.40 ± 1.78	3.14 ± 3.26
DJF	13.68 ± 12.57	6.61 ± 4.62	7.07 ± 7.96
MAM	3.33 ± 1.75	1.32 ± 0.60	2.02 ± 1.18
JJA	0.25 ± 0.27	0.06 ± 0.08	0.19 ± 0.19
SON	4.87 ± 5.62	1.59 ± 1.87	3.28 ± 3.75

Table 6.4: Arctic (60°N-90°N) present-day (PD, 1996-2005), and projected future (RCP85, 2090-2099) instantaneous radiative forcing and standard deviations in mWm^{-2} (total-sky) from the deposition of BC aerosols on land-based snow from all BC aerosol emission sources except wildfires (PD_{nofire}, $RCP85_{nofire}$) and from all emission sources including SPITFIRE wildfire emissions (PD_{fire}, $RCP85_{fire}$). The contribution from wildfires (PD_{WF}, $RCP85_{WF}$) is the difference of PD_{fire}-PD_{nofire} and $RCP85_{fire}$-$RCP85_{nofire}$, respectively. Shown are averages over ten simulation years, as annual (ANNUAL) and seasonal means (DJF, MAM, JJA, and SON) for the surface (SUR) as well as for the top of the atmosphere (TOA).

RF [$\mathbf{mWm^{-2}}$]	**Arctic**		
	PD_{fire}	PD_{nofire}	PD_{WF}
ANNUAL (SUR)	20.80 ± 3.92	7.58 ± 1.60	13.22 ± 3.28
ANNUAL (TOA)	19.74 ± 3.72	7.19 ± 1.52	12.55 ± 3.11
DJF	9.43 ± 2.13	4.11 ± 0.79	5.33 ± 1.85
MAM	49.67 ± 10.63	18.71 ± 4.66	30.96 ± 8.68
JJA	1.96 ± 2.41	0.57 ± 0.79	1.39 ± 1.63
SON	17.90 ± 3.34	5.37 ± 1.34	12.53 ± 3.39
	$RCP85_{fire}$	$RCP85_{nofire}$	$RCP85_{WF}$
ANNUAL (SUR)	10.26 ± 2.87	2.77 ± 0.50	7.50 ± 2.61
ANNUAL (TOA)	9.68 ± 2.70	2.61 ± 0.47	7.07 ± 2.45
DJF	6.55 ± 1.61	2.31 ± 0.57	4.24 ± 1.53
MAM	22.28 ± 6.59	6.12 ± 1.45	16.17 ± 6.03
JJA	2.83 ± 3.31	0.66 ± 0.94	2.17 ± 2.39
SON	7.07 ± 1.48	1.36 ± 0.15	5.71 ± 1.49

6.6 Impact of changes in climate on the effect of BC aerosols deposition on snow

Differences between present-day and projected future wildfire effects on the instantaneous radiative forcing caused by wildfire related deposition of BC aerosols on snow covered land surfaces are caused by a combination of changes in BC aerosol depositions fluxes as well as changes in climate conditions.

To isolate the effect of changes in climate from present-day to projected future conditions following the RCP8.5 scenario, two simulations are compared. First, the PD_{fire} simulation accounting for present-day climate as well as for both present-day anthropogenic and wildfire BC aerosol deposition fluxes. Second, the $Climate_{only}$ simulation considering projected future climate following the RCP8.5 scenario combined with both present-day anthropogenic and wildfire BC aerosol deposition fluxes. A description of the simulations is found in the experimental design in section 6.2. The difference of the simulations ($Climate_{only}$ - PD_{fire}) provides the changes from present-day to projected future climate conditions on the effect of snow contamination by BC aerosols. The global instantaneous radiative forcing values of the two simulations (PD_{fire}, $Climate_{only}$) and the differences showing the impact of changes in the climate conditions (Δ Climate) are summarized in Table 6.5. Compared to the PD_{fire} simulation, the $Climate_{only}$ simulation shows a global instantaneous radiative forcing which is about 54 % lower (10.74 compared to 4.92 mWm^{-2}). This reduction of the global instantaneous radiative forcing of about -5.82 mWm^{-2} can be attributed to the general reduction in the snow cover occurring from present-day to projected future conditions which is described in section 6.4 and illustrated in Figure 6.6. The reduction in the instantaneous radiative forcing due to changes in climate conditions is particularly pronounced in the spring season MAM where the changes in climate lead to an about 70 % reduced projected future instantaneous radiative forcing (-5.92 compared to 2.54 mWm^{-2}). For the winter (DJF) and the autumn (SON) seasons, the changes in climate conditions lead to an about 50 % reduction in the future instantaneous radiative forcing. The lowest impact on the reduction of the future instantaneous radiative forcing by changes in climate conditions is found for the summer season JJA showing a reduction of about 42 %.

The global distribution of the changes in the instantaneous radiative forcing caused by the deposition of BC aerosols on land-based snow due to changes in climate from present-day to projected future conditions is shown in Figure 6.8. Overall, a decrease of the instantaneous radiative forcing by changes in climate conditions is shown which is especially pronounced over the north-eastern part of North America, Greenland, north-eastern China, mountainous regions like the Tibetan Plateau, Siberia and the Antarctic. However, also regions of increasing instantaneous radiative forcing are found for the changing climate conditions e.g. in the Antarctic, Greenland, and North America. The increase in the radiative forcing might be caused by changes in the timing of the snowfall and snow amount differing for present-day and projected future climate conditions. Overall, the reduced instantaneous radiative forcing caused by the

Table 6.5: Global instantaneous radiative forcing and standard deviations in mWm^{-2} for total-sky conditions resulting from the deposition of BC aerosols from all emission sources including wildfires on land-based snow. The PD_{fire} simulation considers present-day climate, anthropogenic and wildfire emissions, while the $Climate_{only}$ simulation accounts for present-day anthropogenic and wildfire emissions as well, but projected future climate conditions following the RCP8.5 scenario. Δ Climate shows the difference of the two simulations (PD_{fire}-$Climate_{only}$) isolating the contribution of the climate on the global instantaneous radiative forcing. Shown are averages over ten simulation years, respectively. Annual (ANNUAL) averages are shown for the surface (SUR) as well as for the top of the atmosphere (TOA). DJF, MAM, JJA, and SON are seasonal averages for TOA.

RF [mWm^{-2}]	**PD_{fire}**	**$Climate_{only}$**	**Δ Climate**
ANNUAL (SUR)	11.22 ± 7.01	5.15 ± 5.06	-6.07 ± 2.13
ANNUAL (TOA)	10.74 ± 6.77	4.92 ± 4.85	-5.82 ± 2.08
DJF	24.75 ± 16.42	12.55 ± 12.27	-12.19 ± 4.71
MAM	8.47 ± 2.66	2.54 ± 1.52	-5.92 ± 1.52
JJA	0.31 ± 0.23	0.18 ± 0.19	-0.13 ± 0.10
SON	9.45 ± 8.04	4.39 ± 5.46	-5.05 ± 2.70

land-based snow contamination through BC aerosols due to changes in climate from present-day to projected future conditions dominates globally.

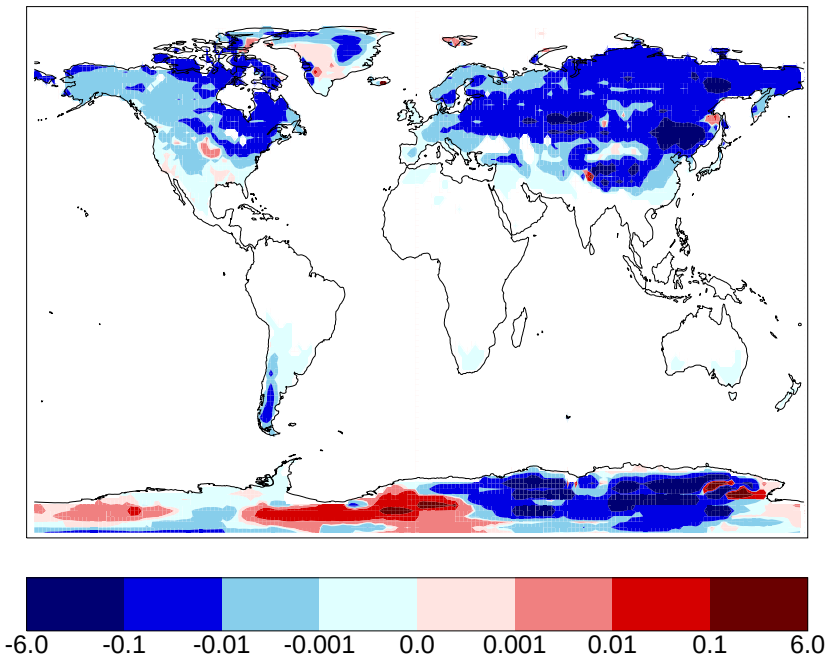

Figure 6.8: Instantaneous radiative forcing in Wm^{-2} (TOA, total-sky conditions) caused by changes from present-day to projected future climate conditions following the RCP8.5 scenario. Shown are differences of the simulations $Climate_{only}$ minus PD_{fire}, only differing in the prescribed climate conditions, averaged over ten simulation years.

6.7 Impact of changes in future anthropogenic BC aerosol deposition on snow

So far the wildfire contribution to the total instantaneous radiative forcing was assessed assuming that the remaining BC aerosol emission sources stay constant. Anthropogenic BC aerosol emission sources, however, will be strongly reduced in the future as a measure to control air quality as projected in the RCP8.5 scenario (van Vuuren et al., 2011). Here, one more set of simulations is analysed in which also anthropogenic BC aerosol emissions are altered according to the RCP8.5 projection.

Comparing present-day and projected future anthropogenic BC aerosol deposition fluxes following the RCP8.5 scenario, shows a decline of the projected future BC aerosol deposition fluxes towards the end of the 21st century due to enforced air quality legislation of about 50 % as summarized in Table 6.1 in section 6.1.1 (5.23 (DEP_RCP85$_{nofire}$) compared to 2.49 Tgyear^{-1} (DEP_aRCP85$_{nofire}$)).

The global instantaneous radiative forcing in mWm^{-2} for total-sky conditions resulting from the deposition of BC aerosols on land-based snow for the set of simulations used

Table 6.6: Global present-day (PD, 1996-2005), and projected future (RCP85, 2090-2099) instantaneous radiative forcing and standard deviations in mWm^{-2} for total-sky conditions resulting from the deposition of BC aerosols on land-based snow resulting from all BC aerosol emission sources except wildfires (PD$_{nofire}$, RCP85$_{nofire}$) and from all emission sources including SPITFIRE wildfire emissions (PD$_{fire}$, RCP85$_{fire}$). The contribution from wildfires only (PD$_{WF}$, RCP85$_{WF}$) is the difference of PD$_{fire}$-PD$_{nofire}$ and RCP85$_{fire}$-RCP85$_{nofire}$, respectively. Shown are averages over ten simulation years, as annual (ANNUAL) and seasonal means (DJF, MAM, JJA, and SON) for the surface (SUR) as well as for the top of the atmosphere (TOA).

RF [mWm^{-2}]	**Global**		
	RCP85$_{fire}$	RCP85$_{nofire}$	RCP85$_{WF}$
ANNUAL (SUR)	5.80 ± 5.26	2.51 ± 1.86	3.29 ± 3.40
ANNUAL (TOA)	5.53 ± 5.04	2.40 ± 1.78	3.14 ± 3.26
DJF	13.68 ± 12.57	6.61 ± 4.62	7.07 ± 7.96
MAM	3.33 ± 1.75	1.32 ± 0.60	2.02 ± 1.18
JJA	0.25 ± 0.27	0.06 ± 0.08	0.19 ± 0.19
SON	4.87 ± 5.62	1.59 ± 1.87	3.28 ± 3.75
	aRCP85$_{fire}$	aRCP85$_{nofire}$	aRCP85$_{WF}$
ANNUAL (SUR)	6.61 ± 7.19	0.83 ± 0.39	5.78 ± 6.81
ANNUAL (TOA)	6.32 ± 6.89	0.79 ± 0.38	5.54 ± 6.52
DJF	15.13 ± 17.04	2.23 ± 1.03	12.90 ± 16.07
MAM	3.09 ± 2.81	0.48 ± 0.17	2.60 ± 2.04
JJA	0.28 ± 0.29	0.02 ± 0.02	0.27 ± 0.27
SON	6.79 ± 8.13	0.42 ± 0.34	6.37 ± 7.79

is summarized in Table 6.6. The reduction in anthropogenic BC aerosol emissions results in a decrease in the instantaneous radiative forcing for present-day to projected future anthropogenic related BC aerosol deposition fluxes in the case wildfire emissions are excluded (2.40 (RCP85$_{nofire}$) compared to 0.79 (aRCP85$_{nofire}$) mWm^{-2}) of about 67 %. Accounting in addition for projected future BC aerosol deposition fluxes related to wildfires combined with present-day (RCP85$_{fire}$) and projected future (aRCP85$_{fire}$) anthropogenic BC aerosol deposition fluxes, a decrease in the instantaneous radiative forcing including future anthropogenic BC aerosol deposition fluxes is expected as well, as the future wildfire aerosol deposition fluxes remain unchanged between the two simulations. Surprisingly, the instantaneous radiative forcing combining projected future wildfire and anthropogenic BC aerosol deposition fluxes is about 14 % higher for the aRCP85$_{fire}$ simulation compared to the RCP85$_{fire}$ simulation (6.32 compared to 5.53 mWm^{-2}).

The potential reason of the unexpected increase in the future instantaneous radiative forcing from present-day to projected future anthropogenic BC aerosol deposition fluxes is further analysed in the following. Figure 6.9 shows the differences between the present-day and projected future BC aerosol deposition fluxes of the simulations excluding wildfire BC aerosol emissions (RCP85$_{nofire}$-aRCP85$_{nofire}$) on the left, and for the simulations accounting for wildfires (RCP85$_{fire}$-aRCP85$_{fire}$) on the right. Here, the patterns of the BC aerosol deposition fluxes show clear differences: The deposition fluxes including wildfire BC aerosol emissions show a more widespread response. This is related to a potentially higher impact on the BC aerosol transport in the atmosphere caused by the reduction of the anthropogenic BC aerosols, as BC aerosol concentrations in the atmosphere are high when wildfires are included compared to the simulations in which wildfire BC aerosol emissions were excluded.
These patterns of the differences in the long-range transport of the BC aerosols are also reflected in the resulting instantaneous radiative forcing. The differences in the instantaneous radiative forcing resulting from prescribed present-day and projected fu-

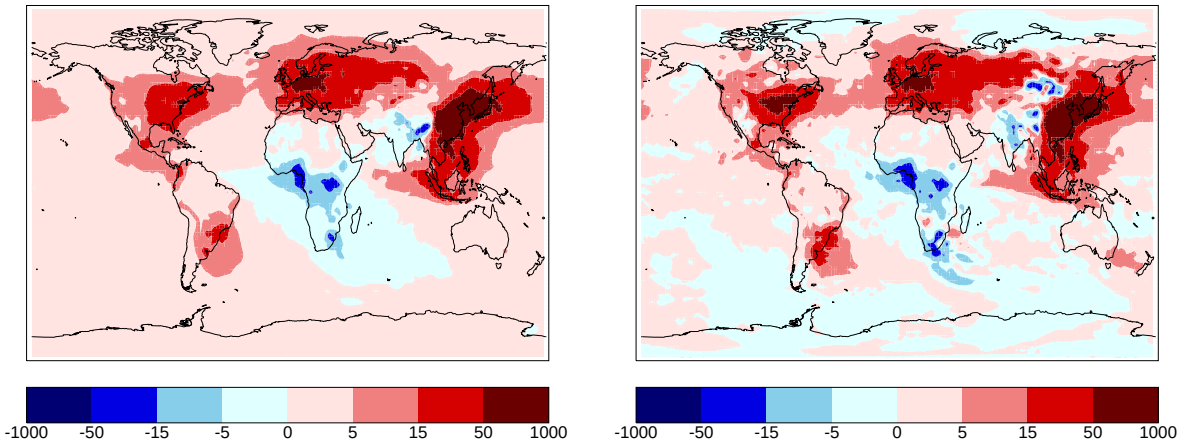

Figure 6.9: Differences in present-day and projected future anthropogenic BC aerosol deposition fluxes in mgm^{-2}year^{-1} excluding wildfire BC aerosol deposition fluxes (RCP85$_{nofire}$-aRCP85$_{nofire}$, left) and including wildfire BC aerosol deposition fluxes (RCP85$_{fire}$-aRCP85$_{fire}$, right).

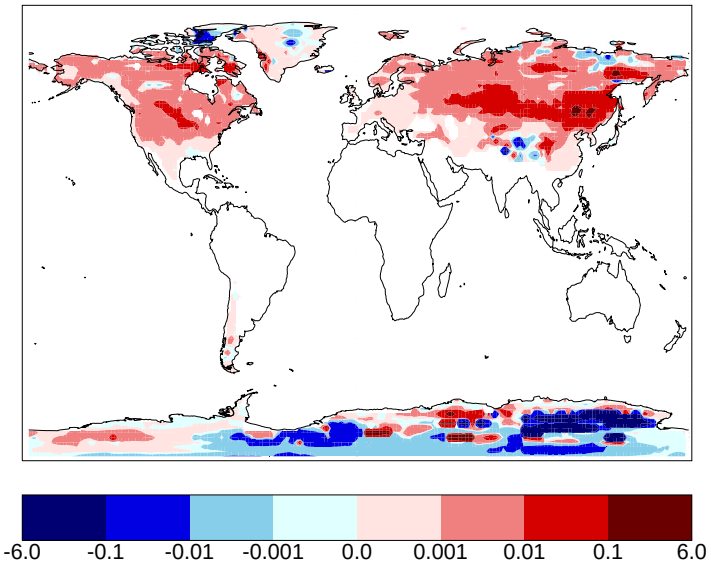

Figure 6.10: Differences in the instantaneous radiative forcing [Wm^{-2}] caused by the deposition of BC aerosols on snow (total-sky conditions, TOA) resulting from differences in present-day and projected future anthropogenic BC aerosol deposition fluxes including wildfires (RCP85$_{fire}$-aRCP85$_{fire}$).

ture BC aerosol deposition fluxes for the RCP85$_{fire}$ and the aRCP85$_{fire}$ simulations are shown in Figure 6.10. In the Northern Hemisphere, the instantaneous radiative forcing is mostly higher for the RCP85$_{fire}$ simulation. In some spots e.g. northern Siberia, Greenland and the Tibetan Plateau higher instantaneous radiative forcing is found for the aRCP85$_{fire}$ simulation accounting for lower anthropogenic BC aerosol deposition fluxes. The largest differences in the instantaneous radiative forcing between the two simulations occur in the Antarctic showing an increased instantaneous radiative forcing. Averaging the differences in the instantaneous radiative forcing between the two simulations for the Northern and the Southern Hemisphere, respectively, results in a positive radiative forcing of about 1.61 mWm^{-2} for the Northern Hemisphere and a negative instantaneous radiative forcing of about -3.19 mWm^{-2} on the Southern Hemisphere caused by the projected future anthropogenic BC aerosol deposition fluxes. Thus, the effect of the projected future anthropogenic BC aerosol deposition fluxes in the Antarctic predominates resulting in a higher global projected future instantaneous radiative forcing resulting from the aRCP85$_{fire}$ simulation.
Restricting the analysis to the Arctic region (60°N-90°N) as summarized in Table 6.7, the instantaneous radiative forcing decreases for the simulations excluding wildfire BC aerosol deposition fluxes (RCP85$_{nofire}$, aRCP85$_{nofire}$) by about 72 % (2.61 compared to 0.73 mWm^{-2}). In addition, the instantaneous radiative forcing between present-day and projected future anthropogenic BC aerosol deposition fluxes decreases for the simulations including wildfire BC aerosol deposition fluxes (RCP85$_{fire}$, aRCP85$_{fire}$) as well, lowering the instantaneous radiative forcing by about 23 % (9.68 compared to 7.47 mWm^{-2}). Thus, the resulting instantaneous radiative forcing related to wildfires (RCP85$_{WF}$, aRCP85$_{WF}$) also shows a decrease in the instantaneous radiative forcing between present-day and projected future anthropogenic BC aerosol deposition fluxes by about 5 % (7.07 compared to 6.75 mWm^{-2}). Overall, the contribution from wildfires

Table 6.7: Arctic (60°N-90°N) projected future instantaneous radiative forcing and standard deviations in mWm^{-2} for total-sky conditions resulting from the deposition of BC aerosols on land-based snow. All BC aerosol emission sources except wildfires are considered in the $RCP85_{nofire}$ and $aRCP85_{nofire}$ simulations, all emission sources including SPITFIRE wildfire emissions in the $RCP85_{fire}$ and $aRCP85_{fire}$ simulation. Projected future instantaneous radiative forcing from wildfires only are shown for $RCP85_{WF}$ ($RCP85_{fire}$-$RCP85_{nofire}$) and $aRCP85_{WF}$ ($aRCP85_{fire}$-$aRCP85_{nofire}$). The RCP85 simulations account for present-day anthropogenic BC aerosol deposition fluxes, while the aRCP85 simulations account for projected future anthropogenic BC aerosol deposition fluxes following the RCP8.5 scenario. Shown are averages over ten simulation years, respectively. Annual (ANNUAL) means are shown for the surface (SUR) as well as for the top of the atmosphere (TOA). DJF, MAM, JJA, and SON values are seasonal averages for TOA.

RF [mWm^{-2}]	**Arctic**		
	$RCP85_{fire}$	$RCP85_{nofire}$	$RCP85_{WF}$
ANNUAL (SUR)	10.26 ± 2.87	2.77 ± 0.50	7.50 ± 2.61
ANNUAL (TOA)	9.68 ± 2.70	2.61 ± 0.47	7.07 ± 2.45
DJF	6.55 ± 1.61	2.31 ± 0.57	4.24 ± 1.53
MAM	22.28 ± 6.59	6.12 ± 1.45	16.17 ± 6.03
JJA	2.83 ± 3.31	0.66 ± 0.94	2.17 ± 2.39
SON	7.07 ± 1.48	1.36 ± 0.15	5.71 ± 1.49
	$aRCP85_{fire}$	$aRCP85_{nofire}$	$aRCP85_{WF}$
ANNUAL (SUR)	7.93 ± 3.03	0.77 ± 0.18	7.16 ± 2.91
ANNUAL (TOA)	7.47 ± 2.85	0.73 ± 0.17	6.75 ± 2.74
DJF	4.09 ± 1.34	0.60 ± 0.07	3.49 ± 1.29
MAM	17.16 ± 6.77	1.73 ± 0.48	15.43 ± 6.62
JJA	3.15 ± 3.42	0.18 ± 0.26	2.96 ± 3.17
SON	5.50 ± 2.03	0.39 ± 0.09	5.11 ± 1.99

to the total instantaneous radiative forcing increases from about 73 % (7.07 compared to 9.68 mWm^{-2}) to about 90 % (6.75 compared to 7.47 mWm^{-2}) between present-day and projected future anthropogenic BC aerosol emissions, playing thereby the major role in the projected future total instantaneous radiative forcing due to the decrease in anthropogenic BC aerosol deposition fluxes. Or in other words, the decrease in anthropogenic BC aerosol emissions between present-day and the projected future will reduce the instantaneous radiative forcing by about 23 % (9.68 compared to 7.47 mWm^{-2}), which equals about 31 % of the instantaneous radiative forcing attributable to wildfire BC deposition fluxes (7.07 mWm^{-2}).

Chapter 7

Summary and Discussion

7.1 Summary

In the present study the effect of snow darkening through the deposition of black carbon aerosols on snow affecting the radiation balance for pre-industrial, present-day and projected future conditions has been estimated. In addition, the contribution of wildfire-related black carbon aerosol emissions to the overall effect has been assessed. For this, the global general circulation model ECHAM6 of the Max Planck Institute Earth System Model (MPI-ESM) has been extended by a new snow-albedo-scheme which is based on the SNICAR-online model (Flanner et al., 2007). This new modelling framework allows to account for the explicit deposition of black carbon aerosols on snow covered land surfaces, thereby improving the former ECHAM6 snow albedo representation.

An adequate representation of black carbon concentrations in snow forms the basis to assess the radiative forcing of the deposition of black carbon aerosols on snow within a climate model. An evaluation of the model performance, comparing simulated black carbon concentrations in snow to field measurements, as well as to other modelling studies, reveals a reasonable performance of the implemented snow-albedo-scheme in ECHAM6. However, too low black carbon concentrations in snow are simulated for regions in the Arctic which is partly related to a too weak long-range transport from the mid-latitudes to these regions in ECHAM6 (e.g. Bourgeois and Bey, 2011).
The simulated snow cover in ECHAM6, representing another important parameter in the assessment of the effect of the darkening of snow covered surfaces, has been evaluated against observational data sets (MODIS and IMS). Here, an underestimation of the simulated snow cover is found, especially in the spring season in the southerly regions at the margins of the seasonal snow cover in the Northern Hemisphere, in contrast to an overestimation of the snow cover in mountainous regions like in Tibet, Mongolia and China. This seems to be a general problem in other climate models as well (Brutel-Vuilmet et al., 2013) and arises from a too early snow melt at too low temperatures in ECHAM6, which is related to the treatment of the surface energy budget in the model (Räisänen et al., 2014).
Snow albedo reductions due to the deposition of black carbon aerosols on snow have been compared to field measurements yielding similar results.
The appropriate performance of this new modelling framework in terms of BC concen-

trations on snow allows to use it to answer the key research questions which have been raised in section 1.3. Note here, when projected future conditions have been assessed, these refer to the Representative Concentration Pathway 8.5 (RCP8.5) scenario for the end of the 21st century, which is characterized by the strongest changes in climate conditions, but also by a significant decrease of black carbon aerosol emissions as air quality legislation plays an important role in this scenario. The key research questions are summarized in the following.

(i) How large is the radiative forcing caused by the darkening of snow covered surfaces through the deposition of black carbon aerosols for pre-industrial, present-day and future (end of the 21st century) climate states and black carbon aerosol deposition fluxes?

Locally, the simulated instantaneous radiative forcing (total-sky conditions, top of the atmosphere) for pre-industrial, present-day and projected future (end of the 21st century) climate states and black carbon aerosol deposition fluxes can be strong, exceeding radiative forcing values of +1 Wm^{-2} for all three time periods, especially in the winter season. The global instantaneous radiative forcing is, however, rather small compared to the forcing on the local scale. For present-day conditions, the global instantaneous radiative forcing amounts to +6.69 mWm^{-2}. For pre-industrial conditions, characterized by about 47 % lower black carbon aerosol deposition fluxes and higher snow cover compared to present-day conditions, the instantaneous radiative forcing is +5.70 mWm^{-2}. The instantaneous radiative forcing for projected future conditions for the end of the 21st century results in about +1.85 mWm^{-2}, combining 40 % lower black carbon deposition fluxes and a generally lower snow cover compared to present-day conditions. Considering the Arctic region (60°N-90°N) separately, the present-day instantaneous radiative forcing results in about +9.25 mWm^{-2}. A similar instantaneous radiative forcing is found for pre-industrial times with about +9.67 mWm^{-2}. Here, the black carbon aerosols deposited in the Arctic are similar for both time periods. In contrast, about 54 % lower black carbon aerosols deposited in the Arctic under projected future conditions for the end of the 21st century lead to an instantaneous radiative forcing of about +1.76 mWm^{-2}. Thus, the effect of black carbon aerosols deposited on snow altering the snow albedo and the radiative forcing declines between pre-industrial and present-day times and is projected to decline even more considerably for future conditions, especially in the Arctic region.

(ii) How much of the change in the radiative forcing caused by the black carbon deposition fluxes on snow covered surfaces between present-day and the future (end of the 21st century) can be attributed to changes in the climate and how much to changes in the aerosol deposition fluxes?

Including two additional sensitivity experiments, a factor separation analysis following Stein and Alpert (1993) was applied to identify the particular contributions from the climate and the black carbon aerosol deposition fluxes to the decline in the instantaneous radiative forcing from present-day to projected future conditions for the end of

the 21st century. The reduction in the instantaneous radiative forcing between the two time periods amounts to -4.84 mWm^{-2} globally and is even more pronounced in the Arctic region (60°N-90°N) with about -7.49 mWm^{-2}. Here, the total reduction in the instantaneous radiative forcing for both considered regions is almost equally controlled by changes in climate (e.g. changes in snowfall and snowmelt) and through changes in black carbon aerosol deposition fluxes. Climate change alone leads to a decline of about -3.60 mWm^{-2} globally and to about -5.32 mWm^{-2} for the Arctic region, whereas changes in the BC aerosol deposition fluxes lead to a decline of about -3.14 mWm^{-2} globally and to about -4.36 mWm^{-2} in the Arctic. The synergies between the two components contributing to the decline in the total instantaneous radiative forcing for projected future conditions are positive accounting for about +1.90 mWm^{-2} globally and for about +2.19 mWm^{-2} in the Arctic region.

(iii) To what extent do black carbon aerosols released from wildfires contribute to the radiative forcing caused by snow darkening for present-day conditions and how might this contribution change with a different future (end of the 21st century) fire regime?

The contribution of the effect of the darkening by the deposition of black carbon aerosols related to wildfires on snow to the radiative forcing has been isolated from a simulation accounting for all black carbon aerosol emission sources and a simulation in which black carbon aerosol emissions from wildfires have been excluded. The present-day global instantaneous radiative forcing (total-sky conditions, TOA) related to wildfires contributes to about 50 % to the total instantaneous radiative forcing (+5.46 compared to +10.74 mWm^{-2}), showing a higher contribution in the Arctic region with about 64 % (+12.55 compared to +19.74 mWm^{-2}). In the autumn season SON wildfires contribute the most to the total instantaneous radiative forcing with about 64 % (+6.08 compared to +9.45 mWm^{-2}) globally and with about 70 % (+12.53 compared to +17.90 mWm^{-2}) in the Arctic. For projected future climate conditions, wildfire black carbon aerosol emissions increase globally from present-day to projected future conditions by about 5 % (7.43 compared to 7.84 $Tgyear^{-1}$). The small global increase results from a pronounced decrease of projected future wildfire BC aerosol emission fluxes found in most of the tropical regions and an increase in future wildfire BC aerosol emission fluxes in the extratropics, considerably pronounced in the boreal regions. However, a lower instantaneous radiative forcing of about 5.53 mWm^{-2} for projected future climate conditions and projected future wildfire black carbon aerosol emissions is found for the end of the 21st century. The increase in wildfire BC aerosol deposition fluxes in the extratropical regions is thereby outweighed by a decrease in snow covered land areas under RCP8.5 conditions, leading overall to a reduction of the projected future instantaneous radiative forcing related to wildfires. The contribution of wildfires to the total instantaneous radiative forcing, however, increases for projected future conditions compared to present-day conditions. Here, wildfires contribute about 57 % to the total instantaneous radiative forcing (+3.14 compared to +5.53 mWm^{-2}) globally and about 73 % (+7.07 compared to +9.68 mWm^{-2}) considering only the Arctic region. The contribution of wildfires to the total instantaneous radiative forcing

for projected future conditions is highest as well for the autumn season SON and increases compared to present-day conditions to about 67 % (+3.28 compared to +4.87 mWm^{-2}) globally and up to 81 % (+5.71 compared to +7.07 mWm^{-2}) for the Arctic.

7.2 Discussion

After answering the key research questions, the results of the present study are related to the overall estimates of aerosol-climate as well as wildfire-climate interactions in the following.

In the present study, the effect of the deposition of black carbon aerosols on snow leads to an instantaneous radiative forcing for present-day conditions which is with +6.69 mWm^{-2} at the lower bound of previous estimates as summarized in the IPCC AR5 (+0.01 to +0.08 Wm^{-2}; Boucher et al., 2013). The effect of black carbon aerosols deposited on snow altering the snow albedo and the radiative forcing is lower for pre-industrial times (+5.70 mWm^{-2}) compared to present-day conditions and is projected to decline even more considerably for future conditions (+1.85 mWm^{-2}), especially in the Arctic region. This reduction in the instantaneous radiative forcing from present-day to projected future conditions is caused about equally by changes in climate as well as changes in the black carbon aerosol deposition fluxes. However, compared to the overall global black carbon aerosol effect as estimated for present-day conditions in Bond et al. (2013) of about +1.1 (+0.17 to +2.1) Wm^{-2} the contribution of the radiative forcing related to the deposition of black carbon aerosols on snow is rather small and will become even smaller in the future. Note here that even if the instantaneous radiative forcing of the effect of snow darkening is small globally, the efficacy of the effect is about 1.7 to 4.5 times larger compared to other forcing agents (e.g. Hansen and Nazarenko, 2004; Flanner et al., 2007). Locally, the instantaneous radiative forcing due to the deposition of black carbon aerosols on snow, assessed in the present study, e.g. in mountainous regions like in Tibet, is high, exceeding values of +1 Wm^{-2}. This supports the large local impact of the contamination of snow due to black carbon aerosols as discussed in previous studies (e.g. Flanner et al., 2007; Kopacz et al., 2011; Ménégoz et al., 2014), likely affecting the timing of snow melt (e.g. Jacobi et al., 2015).

Wildfire emissions form a significant contribution to the BC aerosols deposited on snow covered surfaces. With a changing climate, wildfire BC aerosol emissions will change. This study provides, for the first time, an estimate of the effect of the deposition of black carbon aerosols related to wildfires on snow for present-day conditions as well as for projected future fire regimes. In the present study, wildfires contribute about 50 % for present-day and about 57 % for projected future conditions to the overall instantaneous radiative forcing of the darkening of snow. For present-day conditions, black carbon aerosols released by wildfires cause an instantaneous radiative forcing of about +5.46 mWm^{-2} which more than doubles regarding the Arctic region separately (+12.55 mWm^{-2}). However, this is a small forcing when compared to the overall negative radiative forcing of about -0.5 Wm^{-2} attributed to wildfires (Ward et al., 2012). A reduction of the instantaneous radiative forcing between present-day and projected future conditions is provided due to changes in projected future climate

conditions as well as changing projected future wildfire black carbon aerosol deposition fluxes. Here, the instantaneous radiative forcing is reduced to about +3.14 mWm^{-2}. Considering decreasing anthropogenic BC aerosol deposition fluxes as projected in the RCP8.5 scenario for the end of the 21st century, the contribution of projected future wildfires in a projected future climate on the instantaneous radiative forcing increases for the Arctic region: For present-day anthropogenic BC aerosol deposition fluxes, projected future wildfires account for about 73 % of the overall Arctic radiative forcing, whereas the contribution to the projected future Arctic total instantaneous radiative forcing resulting from wildfires increases to about 90 % when projected future anthropogenic BC aerosol deposition fluxes are taken into account. Thus, wildfires play the major role in the projected future total instantaneous radiative forcing of snow darkening due to the decrease in anthropogenic BC aerosol deposition fluxes.

The assessment of the effect of the deposition of black carbon aerosols on snow covered surfaces on the radiative forcing presented in the present study goes along with a number of uncertainties. As shown in previous studies (e.g. Räisänen et al., 2014), the snow cover in ECHAM6 is underestimated, especially in the spring season in the Northern Hemisphere at the southerly margins of the seasonal snow cover. As these regions are e.g. close to the large anthropogenic black carbon aerosol emission sources, the radiative forcing of the deposition of black carbon aerosols on snow might be underestimated. Hence, an improvement in the seasonal representation of the snow cover would be desirable for an improved assessment of the full effect of the BC aerosol deposition on snow on radiation.
In addition, the long-range transport of black carbon aerosols from the mid-latitudes to the Arctic in ECHAM6-HAM2 is too weak, which was e.g. identified by Bourgeois and Bey (2011) and is reflected in lower black carbon concentrations in snow as simulated in the present study compared to measurements for this region. These lower black carbon concentrations in snow might result in an underestimation of the instantaneous radiative forcing in these regions, however, to which extent is not clear due to the non-linear dependency of the snow-albedo-scheme on the snowfall.

Even if the performance of the implemented snow-albedo scheme is reasonable in representing black carbon concentrations in snow and snow albedo reductions compared to measurements, several processes are neglected in the implemented snow-albedo-scheme:

- The snow-albedo-scheme in the present study only affects the snow albedo of snow covered land surfaces, but does not affect the snow on sea ice. Flanner et al. (2007) estimated that about 20 % of the total radiative forcing resulting from the deposition of black carbon aerosols on snow is caused by the deposition of black carbon aerosols on snow-covered sea ice. Neglecting this process leads to an underestimation of the radiative forcing resulting from the deposition of black carbon aerosols on snow, complicating a comparison to studies including the effect over sea ice as well.

- The concentrations of black carbon aerosols and other light-absorbing impurities increase in surface snow with snow melt if their scavenging efficiency is less than 100 % (e.g. Conway et al., 1996; Doherty et al., 2013). Conway et al. (1996) treated pure snow with known impurity amounts on open fields, leading to residual concentrations of about 500 ng(BC)g(snow)$^{-1}$ after several weeks, leading to albedo reductions of about 30 % and increased melting by about 50 %. The implemented scheme does account for the scavenging of black carbon aerosols during snow melt. However, the black carbon aerosols are mixed uniformly into the available snow pack. The missing accumulation of the black carbon aerosols in the surface layer might lead to an underestimation of the radiative forcing.

Very little is known about the scavenging of black carbon aerosols during snow melt due to the low number of studies (e.g. Conway et al., 1996; Doherty et al., 2013), which are available (e.g. Flanner et al., 2007). Therefore, the uncertainty related to these observed values is large. In addition, the role of the particle size influencing the scavenging ratio is uncertain as well.

7.3 Research perspective

The implemented snow-albedo-scheme introduced in the present study can also be implemented over sea ice to assess the full effect of the deposition of black carbon aerosols on snow on the snow albedo in ECHAM6. In addition, instead of prescribing the black carbon aerosol deposition fluxes, a coupling to the aerosol module HAM2 is desirable to account also for the feedback of the deposition of black carbon aerosols on snow with the atmosphere. This would also allow to assess the timing in changes of the snow melt by the deposition of black carbon aerosols on snow (e.g. Jacobi et al., 2015) leading to an earlier exposure of the underlying darker soil triggering thereby the snow-albedo-feedback (e.g. Hansen and Nazarenko, 2004; Jacobson, 2004; Flanner et al., 2007).
In addition, the implemented snow-albedo-scheme can be extended for two more aerosol species, dust and volcanic ash, as the SNICAR-online model (Flanner et al., 2007) provides the snow albedo values depending on these specific aerosol concentrations as well. As Flanner et al. (2014) estimated a positive radiative forcing due to the deposition of ash aerosols on snow from the 2010 Eyjafjallajökull volcanic eruption and Zhao et al. (2014) estimated a positive radiative forcing of dust in snow concentrations with a similar magnitude as the forcing of BC concentrations in snow in a case study over North China, these aerosol species should be taken into account as well.
As the radiative forcing of the deposition of black carbon aerosols is large in specific regions like in the Tibetan Plateau where the population strongly depends on the water supply (Immerzeel et al., 2010), an interesting application for the new implemented snow-albedo-scheme would be a regional assessment of the deposition of black carbon aerosols on snow.
The study by Sand et al. (2013) suggests that the Arctic is five times more sensitive to black carbon aerosol emissions directly emitted in the Arctic compared to black

carbon aerosols emitted in the mid-latitudes. Thus, the question arises how changing black carbon aerosol emissions in the future e.g. from shipping emissions (e.g. Browse et al., 2013) or from other sources as gas flaring (e.g. Stohl et al., 2013), might potentially shape these regions in the future.

Appendix A

Parameters chosen to calculate snow albedo values depending on BC in snow concentrations as well as the snow age obtained by the single-layer simulator SNICAR-online (http://snow.engin.umich.edu/info.html, Flanner et al. (2007)).

1a Incident radiation: Direct

1b Solar zenith angle, if incident radiation is direct (0-89 degrees): 60 degrees

2 Surface spectral distribution:
Mid-latitude winter, clear-sky; Mid-latitude winter, cloudy;
Summit Greenland, clear-sky; Summit Greenland, cloudy

3 Snow grain effective radius (30-1500 microns): 50, 150, 500, 1000 μm

4 Snowpack thickness: 1 meters

5 Snowpack density: 200 kg/m^3

6 Albedo of underlying ground:
Visible (0.3-0.7 m): 0.2
Near-infrared (0.7-5.0 m): 0.4

7 Black carbon concentration (ppb, or nanograms of BC per gram of ice):
Uncoated: 0 ppb
Sulphate-coated: ranging from 0 to 1500 ppb with an interval width of 100 ppb
MAC scaling factor (experimental): 1.0

8 Dust concentration (ppm, or micrograms of dust per gram of ice):
Size 1 (0.1-1.0 m diameter): 0 ppm
Size 2 (1.0-2.5 m diameter): 0 ppm
Size 3 (2.5-5.0 m diameter): 0 ppm
Size 4 (5.0-10.0 m diameter): 0 ppm

9 Volcanic ash concentration (ppm, or micrograms of ash per gram of ice):
0 ppm

10 Experimental particle 1 concentration (ppb, or nanograms of particle per gram of ice): 0 ppb

Acknowledgements

First of all, I thank my supervisor Silvia Kloster for the very good support and advice during the last years. Further, I thank her for the opportunity to do my research on this interesting topic in the environment of the MPI-M, allowing to continuously improve my scientific skills.

I would like to thank Martin Claussen and Dirk Notz who were part of my Advisory Panel. The helpful comments and discussions in the regular panel meetings provided me with motivation and new ideas.

Furthermore, I also thank Quentin Bourgeois for his scientific support in the beginning of my PhD studies. Moreover, I thank Tanja Stanelle, Andreas Veira, Mark Flanner, and the Integrated Climate Data Center for providing data for my research.

I especially thank Stiig for technical support. Furthermore I thank Thomas for fruitful discussions on the albedo in the model, as well as Veronika and Reiner for answering every technical question.

Moreover, I thank the IMPRS-ESM for the opportunity to graduate in an international and interdisciplinary working environment, which I enjoyed very much. I thank Antje, Connie and Wiebke for the excellent organization and administration of the school.

I very much enjoyed being part of the IMPRS-ESM and of the Land Department. Thank you to all of you, for the friendly working environment and the inspiring lunch and coffee breaks. Thanks especially to Rika, Daniela, Andreas, Gitta, Victoria, Fabio, Matthias, Jan, Vivienne, Sylvia, and Irina. I also would like to thank my office colleagues Sabine and Rainer.

Many thanks to Thomas Kleinen, Gitta, Daniela, Gernot, Stiig, Fabio and Andreas for comments and suggestions, as well as proof-reading.

Last but not least, I especially thank my parents and friends for their continuous support in every respect, their patience and encouragement throughout the last years.

Acronyms

ACCMIP Atmospheric Chemistry and Climate Model Intercomparison Project
AeroCom Aerosol Comparisons between Observations and Models
AMIP Atmosphere Model Intercomparison Project
AR5 Fifth Assessment Report
asl active snow layer
BATS Biosphere-Atmosphere Transfer Scheme
BC black carbon
CESM Community Earth System Model
CLM Community Land Model
CMIP5 Coupled Model Intercomparison Project Phase 5
DGVM dynamic global vegetation model
ECMWF European Centre for Medium Range Weather Forecasts
ESM Earth system model
FRP fire radiative power
GCM general circulation model
ICDC Integrated Climate Data Center
IMS Interactive Multisensor Snow and Ice Mapping System
IPCC Intergovernmental Panel on Climate Change
LAI leaf area index
MODIS Moderate Resolution Imaging Spectroradiometer
MPI-ESM Max Planck Institute Earth System Model
NIR near-infrared
OC organic carbon
PD present-day
PFT plant functional type
PI pre-industrial
RCP Representative Concentration Pathway
RF radiative forcing
SIC sea ice concentration
SNICAR Snow, Ice, and Aerosol Radiation
SSP Shared Socioeconomic Pathway
SST sea surface temperature
SUR surface
SWNB Shortwave Narrowband Model
TOA top of atmosphere
VIS visible

List of Figures

List of Tables

References

Akagi, S. K., Yokelson, R. J., Wiedinmyer, C., Alvarado, M. J., Reid, J. S., Karl, T., Crounse, J. D., and Wennberg, P. O. (2011). Emission factors for open and domestic biomass burning for use in atmospheric models. *Atmospheric Chemistry and Physics*, 11(9):4039–4072.

Albrecht, B. (1989). Aerosols, cloud microphysics, and fractional cloudiness. *Science*, 245(4923):1227–1230.

Alpert, P. and Sholokhman, T. (2011). *Factor Separation in the Atmosphere*. Cambridge University Press, Cambridge.

Andreae, M. O. and Merlet, P. (2001). Emissions of trace gases and aerosols from biomass burning. *Global Biogeochemical Cycles*, 15(4):955–966.

Armstrong, R. L. and Brodzik, M. J. (2002). Northern Hemisphere EASE-Grid weekly snow cover and sea ice extent Version 2. *Boulder, CO, USA: National Snow and Ice Data Center. Digital media. CD-ROM.*

Bond, T. C. (2004). A technology-based global inventory of black and organic carbon emissions from combustion. *Journal of Geophysical Research*, 109(D14):D14203.

Bond, T. C., Bhardwaj, E., Dong, R., Jogani, R., Jung, S., Roden, C., Streets, D. G., and Trautmann, N. M. (2007). Historical emissions of black and organic carbon aerosol from energy-related combustion, 1850-2000. *Global Biogeochemical Cycles*, 21(2):n/a–n/a.

Bond, T. C., Doherty, S. J., Fahey, D. W., Forster, P. M., Berntsen, T., Deangelo, B. J., Flanner, M. G., Ghan, S., Kärcher, B., Koch, D., Kinne, S., Kondo, Y., Quinn, P. K., Sarofim, M. C., Schultz, M. G., Schulz, M., Venkataraman, C., Zhang, H., Zhang, S., Bellouin, N., Guttikunda, S. K., Hopke, P. K., Jacobson, M. Z., Kaiser, J. W., Klimont, Z., Lohmann, U., Schwarz, J. P., Shindell, D., Storelvmo, T., Warren, S. G., and Zender, C. S. (2013). Bounding the role of black carbon in the climate system: A scientific assessment. *Journal of Geophysical Research: Atmospheres*, 118(11):5380–5552.

Boucher, O., Randall, D., Artaxo, P., Bretherton, C., Feingold, G., Forster, P., Kerminen, V.-M., Kondo, Y., Liao, H., Lohmann, U., Rasch, P., Satheesh, S. K., Sherwood, S., Stevens, B., and Zhang, X. Y. (2013). 7. Clouds and Aerosols. *Climate Change 2013: The Physical Science Basis. Contribution of Working Group I to the Fifth Assessment Report of the Intergovernmental Panel on Climate Change*, pages 571–657.

Bourgeois, Q. and Bey, I. (2011). Pollution transport efficiency toward the Arctic: Sensitivity to aerosol scavenging and source regions. *Journal of Geophysical Research: Atmospheres*, 116(8).

Bowman, D. M. J. S., Balch, J. K., Artaxo, P., Bond, W. J., Carlson, J. M., Cochrane, M. A., D'Antonio, C. M., DeFries, R. S., Doyle, J. C., Harrison, S. P., Johnston, F. H., Keeley,

J. E., Krawchuk, M. A., Kull, C. A., Marston, J. B., Moritz, M. A., Prentice, I. C., Roos, C. I., Scott, A. C., Swetnam, T. W., van der Werf, G. R., and Pyne, S. J. (2009). Fire in the Earth System. *Science*, 324(5926):481–484.

Brandt, R. E., Warren, S. G., and Clarke, A. D. (2011). A controlled snowmaking experiment testing the relation between black carbon content and reduction of snow albedo. *Journal of Geophysical Research: Atmospheres*, 116(8):2–7.

Brovkin, V., Boysen, L., Raddatz, T., Gayler, V., Loew, A., and Claussen, M. (2013). Evaluation of vegetation cover and land-surface albedo in MPI-ESM CMIP5 simulations. *Journal of Advances in Modeling Earth Systems*, 5(1):48–57.

Brown, R. D. and Robinson, D. a. (2011). Northern Hemisphere spring snow cover variability and change over 1922-2010 including an assessment of uncertainty. *Cryosphere*, 5(2000):219–229.

Browse, J., Carslaw, K. S., Schmidt, A., and Corbett, J. J. (2013). Impact of future Arctic shipping on high-latitude black carbon deposition. *Geophysical Research Letters*, 40(16):4459–4463.

Brutel-Vuilmet, C., Ménégoz, M., and Krinner, G. (2013). An analysis of present and future seasonal Northern Hemisphere land snow cover simulated by CMIP5 coupled climate models. *The Cryosphere*, 7(1):67–80.

Charlson, R. J. and Pilat, M. J. (1969). Climate: The Influence of Aerosols. *Journal of Applied Meteorology*, 8(6):1001–1002.

Charlson, R. J., Schwartz, S. E., Hales, J. M., Cess, R. D., Coakley, J. a., Hansen, J. E., and Hofmann, D. J. (1992). Climate forcing by anthropogenic aerosols. *Science (New York, N.Y.)*, 117(January).

Clarke, A. D. and Noone, K. J. (1985). Soot in the Arctic snowpack: A cause for pertubations in radiative transfer. *Atmospheric Environment*, 19(12):2045–2053.

Claussen, M., Selent, K., Brovkin, V., Raddatz, T., and Gayler, V. (2013). Impact of CO2 and climate on Last Glacial maximum vegetation-a factor separation. *Biogeosciences*, 10(6):3593–3604.

Collins, W. D., Rasch, P. J., Boville, B. a., Hack, J. J., Williamson, D. L., Kiehl, J. T., Briegleb, B., Bitz, C., Lin, S.-J., Zhang, M., and Dai, Y. (2004). Description of the NCAR Community Atmosphere Model (CAM 3.0). Technical Report June, NCAR.

Conway, H., Gades, A., and Raymond, C. F. (1996). Albedo of dirty snow during conditions of melt. *Water Resources Research*.

Dickinson, R., Henderson-Sellers, A., Kennedy, P., and Wilson, M. (1986). Biosphere-atmosphere transfer scheme (BATS) for the NCAR Community Climate Model. Technical report, NCAR.

Dockery, D. W., Pope, C. A. I. I. I., Xu, X., Spengler, J. D., Ware, J. H., Fay, M. E., Ferris, B. G., and Speizer, F. E. (1993). An Association between Air Pollution and Mortality in Six U.S. Cities. *The New England Journal of Medicine*, 329:1753–1759.

Doherty, S. J., Grenfell, T. C., Forsström, S., Hegg, D. L., Brandt, R. E., and Warren, S. G. (2013). Observed vertical redistribution of black carbon and other insoluble light-absorbing particles in melting snow. *Journal of Geophysical Research: Atmospheres*, 118(11):5553–5569.

Doherty, S. J., Warren, S. G., Grenfell, T. C., Clarke, A. D., and Brandt, R. E. (2010). Light-absorbing impurities in Arctic snow. *Atmospheric Chemistry and Physics*, 10(23):11647–11680.

Dumont, M., Brun, E., Picard, G., Michou, M., Libois, Q., Petit, J.-r., Geyer, M., Morin, S., and Josse, B. (2014). Contribution of light-absorbing impurities in snow to Greenlands darkening since 2009. *Nature Geoscience*, 7(7):509–512.

Flanner, M. G., Gardner, a. S., Eckhardt, S., Stohl, A., and Perket, J. (2014). Aerosol radiative forcing from the 2010 Eyjafjallajökull volcanic eruptions. *Journal of Geophysical Research: Atmospheres*, pages 9481–9491.

Flanner, M. G. and Zender, C. S. (2005). Snowpack radiative heating: Influence on Tibetan Plateau climate. *Geophysical Research Letters*, 32(6):1–5.

Flanner, M. G. and Zender, C. S. (2006). Linking snowpack microphysics and albedo evolution. *Journal of Geophysical Research: Atmospheres*, 111(12).

Flanner, M. G., Zender, C. S., Hess, P. G., Mahowald, N. M., Painter, T. H., Ramanathan, V., and Rasch, P. J. (2009). Springtime warming and reduced snow cover from carbonaceous particles. *Atmospheric Chemistry and Physics*, 8(6):19819–19859.

Flanner, M. G., Zender, C. S., Randerson, J. T., and Rasch, P. J. (2007). Present-day climate forcing and response from black carbon in snow. *Journal of Geophysical Research*, 112(D11):D11202.

Flannigan, M., Cantin, A. S., De Groot, W. J., Wotton, M., Newbery, A., and Gowman, L. M. (2013). Global wildland fire season severity in the 21st century. *Forest Ecology and Management*, 294:54–61.

Flannigan, M. D., Krawchuk, M. A., de Groot, W. J., Wotton, B. M., and Gowman, L. M. (2009). Implications of changing climate for global wildland fire. *International Journal of Wildland Fire*, 18(5):483–507.

Giorgetta, M. A., Jungclaus, J. H., Reick, C. H., Legutke, S., Bader, J., Böttinger, M., Brovkin, V., Crueger, T., Esch, M., Fieg, K., Glushak, K., Gayler, V., Haak, H., Hollweg, H.-D., Ilyina, T., Kinne, S., Kornblueh, L., Matei, D., Mauritsen, T., Mikolajewicz, U., Mueller, W., Notz, D., Pithan, F., Raddatz, T., Rast, S., Redler, R., Roeckner, E., Schmidt, H., Schnur, R., Segschneider, J., Six, K. D., Stockhause, M., Timmreck, C., Wegner, J., Widmann, H., Wieners, K.-H., Claussen, M., Marotzke, J., and Stevens, B. (2013). Climate and carbon cycle changes from 1850 to 2100 in MPI-ESM simulations for the coupled model intercomparison project phase 5. *Journal of Advances in Modeling Earth Systems*, 5(3):572–597.

Goldenson, N., Doherty, S. J., Bitz, C. M., Holland, M. M., Light, B., and Conley, A. J. (2012). Arctic climate response to forcing from light-absorbing particles in snow and sea ice in CESM. *Atmospheric Chemistry and Physics*, 12(17):7903–7920.

Goldewijk, K. K. (2001). Estimating global land use change over the past 300 years: The HYDE Database. *Global Biogeochemical Cycles*, 15(2):417.

Hadley, O. L. and Kirchstetter, T. W. (2012). Black-carbon reduction of snow albedo. *Nature Climate Change*, 2(6):437–440.

Hall, D. K., Riggs, G. A., and Salomonson, V. V. (2006). Updated monthly. MODIS/Terra Snow cover Monthly L3 global 0.05Deg CMG V005 (March 2000 - December 2014). *Boulder, CO, National Snow and Ice Data Center. Digital Media, distributed in netCDF format by the Integrated Climate Data Center (ICDC, http://icdc.zmaw.de, University of Hamburg, Hamburg, Germany.*

Hansen, J. (2005). Earth's Energy Imbalance: Confirmation and Implications. *Science*, 308(5727):1431–1435.

Hansen, J. and Nazarenko, L. (2004). Soot climate forcing via snow and ice albedos. *Proceedings of the National Academy of Sciences of the United States of America*, 101(2):423–8.

Hansen, J., Sato, M., Ruedy, R., Lacis, A., and Oinas, V. (2000). Global warming in the twenty-first century: an alternative scenario. *Proceedings of the National Academy of Sciences of the United States of America*, 97(18):9875–80.

Haywood, J., Office, U. K. M., and Boucher, O. (2000). Estimates of the Direct and Indirect Radiative Forcing Due To Tropospheric Aerosols : a Review. *Journal of Geophysical Research: Atmospheres*, 38(4):513–543.

Huijnen, V., Flemming, J., Kaiser, J. W., Inness, A., Leitão, J., Heil, A., Eskes, H. J., Schultz, M. G., Benedetti, A., Hadji-Lazaro, J., Dufour, G., and Eremenko, M. (2012). Hindcast experiments of tropospheric composition during the summer 2010 fires over western Russia. *Atmospheric Chemistry and Physics*, 12(9):4341–4364.

Hurtt, G. C., Chini, L. P., Frolking, S., Betts, R. a., Feddema, J., Fischer, G., Fisk, J. P., Hibbard, K., Houghton, R. a., Janetos, A., Jones, C. D., Kindermann, G., Kinoshita, T., Klein Goldewijk, K., Riahi, K., Shevliakova, E., Smith, S., Stehfest, E., Thomson, A., Thornton, P., van Vuuren, D. P., and Wang, Y. P. (2011). Harmonization of land-use scenarios for the period 1500-2100: 600 years of global gridded annual land-use transitions, wood harvest, and resulting secondary lands. *Climatic Change*, 109(1):117–161.

Iacono, M. J., Delamere, J. S., Mlawer, E. J., Shephard, M. W., Clough, S. a., and Collins, W. D. (2008). Radiative forcing by long-lived greenhouse gases: Calculations with the AER radiative transfer models. *Journal of Geophysical Research: Atmospheres*, 113(13):2–9.

Immerzeel, W. W., van Beek, L. P. H., and Bierkens, M. F. P. (2010). Climate change will affect the Asian water towers. *Science (New York, N.Y.)*, 328(5984):1382–1385.

Jacobi, H.-W., Lim, S., Ménégoz, M., Ginot, P., Laj, P., Bonasoni, P., Stocchi, P., Marinoni, A., and Arnaud, Y. (2015). Black carbon in snow in the upper Himalayan Khumbu Valley, Nepal: observations and modeling of the impact on snow albedo, melting, and radiative forcing. *The Cryosphere*, 9:1685–1699.

Jacobson, M. Z. (2004). Climate response of fossil fuel and biofuel soot, accounting for soot's feedback to snow and sea ice albedo and emissivity. *Journal of Geophysical Research D: Atmospheres*, 109(21).

Jacobson, M. Z. (2005). Correction to Control of fossil-fuel particulate black carbon and organic matter, possibly the most effective method of slowing global warming. *Journal of Geophysical Research*, 110(D14):D14105.

Jiao, C., Flanner, M. G., Balkanski, Y., Bauer, S. E., Bellouin, N., Berntsen, T. K., Bian, H., Carslaw, K. S., Chin, M., De Luca, N., Diehl, T., Ghan, S. J., Iversen, T., Kirkeväg, A., Koch, D., Liu, X., Mann, G. W., Penner, J. E., Pitari, G., Schulz, M., Seland Ø., Skeie, R. B., Steenrod, S. D., Stier, P., Takemura, T., Tsigaridis, K., Van Noije, T., Yun, Y., and Zhang, K. (2014). An aerocom assessment of black carbon in Arctic snow and sea ice. *Atmospheric Chemistry and Physics*.

Kääb, A., Berthier, E., Nuth, C., Gardelle, J., and Arnaud, Y. (2012). Contrasting patterns of early twenty-first-century glacier mass change in the Himalayas. *Nature*, 488(7412):495–8.

Kaiser, J. W., Heil, A., Andreae, M. O., Benedetti, A., Chubarova, N., Jones, L., Morcrette, J. J., Razinger, M., Schultz, M. G., Suttie, M., and Van Der Werf, G. R. (2012). Biomass burning emissions estimated with a global fire assimilation system based on observed fire radiative power. *Biogeosciences*, 9:527–554.

Keegan, K. M., Albert, M. R., McConnell, J. R., and Baker, I. (2014). Climate change and forest fires synergistically drive widespread melt events of the Greenland Ice Sheet. *Proceedings of the National Academy of Sciences of the United States of America*, 111(22):1–4.

Klein Goldewijk, K. and Verburg, P. H. (2013). Uncertainties in global-scale reconstructions of historical land use: An illustration using the HYDE data set. *Landscape Ecology*, 28(5):861–877.

Koch, D., Menon, S., Del Genio, A., Ruedy, R., Alienov, I., and Schmidt, G. a. (2009). Distinguishing aerosol impacts on climate over the past century. *Journal of Climate*, 22(10):2659–2677.

Kopacz, M., Mauzerall, D. L., Wang, J., Leibensperger, E. M., Henze, D. K., and Singh, K. (2011). Origin and radiative forcing of black carbon transported to the Himalayas and Tibetan Plateau. *Atmospheric Chemistry and Physics*, 11(2010):2837–2852.

Lamarque, J. F., Bond, T. C., Eyring, V., Granier, C., Heil, A., Klimont, Z., Lee, D., Liousse, C., Mieville, A., Owen, B., Schultz, M. G., Shindell, D., Smith, S. J., Stehfest, E., Van Aardenne, J., Cooper, O. R., Kainuma, M., Mahowald, N., McConnell, J. R., Naik, V., Riahi, K., and Van Vuuren, D. P. (2010). Historical (1850-2000) gridded anthropogenic and biomass burning emissions of reactive gases and aerosols: Methodology and application. *Atmospheric Chemistry and Physics*, 10(15):7017–7039.

Lasslop, G., Thonicke, K., and Kloster, S. (2014). SPITFIRE within the MPI Earth system model: Model development and evaluation. *Journal of Advances in Modeling Earth Systems*, 6:740–755.

Lawrence, D. M., Oleson, K. W., Flanner, M. G., Fletcher, C. G., Lawrence, P. J., Levis, S., Swenson, S. C., and Bonan, G. B. (2012). The CCSM4 land simulation, 1850-2005: Assessment of surface climate and new capabilities. *Journal of Climate*, 25(7):2240–2260.

Lohmann, U. and Feichter, J. (2005). Global indirect aerosol effects: a review. *Atmospheric Chemistry and Physics*, 4(6):7561–7614.

Mahowald, N., Ward, D. S., Kloster, S., Flanner, M. G., Heald, C. L., Heavens, N. G., Hess, P. G., Lamarque, J.-F., and Chuang, P. Y. (2011). Aerosol Impacts on Climate and Biogeochemistry. *Annual Review of Environment and Resources*, 36(1):45–74.

Marlon, J., Bartlein, P., Carcaillet, C., Gavin, D., Harrison, S., Higuera, P., Joos, F., Power, M., and Prentice, I. (2008). Climate and human influences on global biomass burning over the past two millennia. *Nature geoscience*, 1(October 2008):697–702.

Ménégoz, M., Gallée, H., and Jacobi, H. W. (2013). Precipitation and snow cover in the Himalaya: From reanalysis to regional climate simulations. *Hydrology and Earth System Sciences*, 17(10):3921–3936.

Ménégoz, M., Krinner, G., Balkanski, Y., Boucher, O., Cozic, A., Lim, S., Ginot, P., Laj, P., Gallée, H., Wagnon, P., Marinoni, A., and Jacobi, H. W. (2014). Snow cover sensitivity to black carbon deposition in the Himalayas: from atmospheric and ice core measurements to regional climate simulations. *Atmospheric Chemistry and Physics*, 14(8):4237–4249.

Myhre, G., Samset, B. H., Schulz, M., Balkanski, Y., Bauer, S., Berntsen, T. K., Bian, H., Bellouin, N., Chin, M., Diehl, T., Easter, R. C., Feichter, J., Ghan, S. J., Hauglustaine, D., Iversen, T., Kinne, S., Kirkeväg, A., Lamarque, J. F., Lin, G., Liu, X., Lund, M. T., Luo, G., Ma, X., Van Noije, T., Penner, J. E., Rasch, P. J., Ruiz, A., Seland, Skeie, R. B., Stier, P., Takemura, T., Tsigaridis, K., Wang, P., Wang, Z., Xu, L., Yu, H., Yu, F., Yoon, J. H., Zhang, K., Zhang, H., and Zhou, C. (2013a). Radiative forcing of the direct aerosol effect from AeroCom Phase II simulations. *Atmospheric Chemistry and Physics*, 13(4):1853–1877.

Myhre, G., Shindell, D., Bréon, F.-M., Collins, W., Fuglestvedt, J., Huang, J., Koch, D., Lamarque, J.-F., Lee, D., Mendoza, B., Nakajima, T., Robock, A., Stephens, G., Takemura, T., and Zhan, H. (2013b). 2013: Anthropogenic and Natural Radiative Forcing. *Climate Change 2013: The Physical Science Basis. Contribution of Working Group I to the Fifth Assessment Report of the Intergovernmental Panel on Climate Change*, pages 659–740.

National Ice Center (2008). Updated daily. IMS daily Northern Hemisphere snow and ice analysis at 1 km, 4 km, and 24 km resolutions. *Boulder, CO: National Snow and Ice Data Center. Digital media, provided in netCDF format by ICDC (http://icdc.zmaw.de).*

Oleson, K. W., Lawrence, D. M., Gordon, B., Flanner, M. G., Kluzek, E., Peter, L. J., Levis, S., Swenson, S. C., and Thornton, P. E. (2010). Technical Description of version 4.0 of the Community Land Model (CLM). *NCAR/TN-478+STR NCAR Technical Note*, (April):266.

Otto, J., Raddatz, T., and Claussen, M. (2011). Strength of forest-albedo feedback in mid-Holocene climate simulations. *Climate of the Past*, 7(3):1027–1039.

Pithan, F. and Mauritsen, T. (2014). Arctic amplification dominated by temperature feedbacks in contemporary climate models. *Nature geoscience*, 7(February):2–5.

Polashenski, C. M., Dibb, J. E., Flanner, M. G., Chen, J. Y., Courville, Z. R., Lai, A. M., Schauer, J. J., Shafer, M. M., and Bergin, M. (2015). Neither dust nor black carbon causing apparent albedo decline in Greenland's dry snow zone; implications for MODIS C5 surface reflectance. *Geophysical Research Letters*, pages n/a–n/a.

Pöschl, U. (2005). Atmospheric aerosols: Composition, transformation, climate and health effects. *Angewandte Chemie - International Edition*, 44(46):7520–7540.

Rabl, A. and Spadaro, J. V. (2000). Public health impact of air pollution and implications for the energy system. *Annual Review of Energy and the Environment*, 25:601–627.

Räisänen, P., Luomaranta, A., Järvinen, H., Takala, M., Jylhä, K., Bulygina, O. N., Luojus, K., Riihelä, A., Laaksonen, A., Koskinen, J., and Pulliainen, J. (2014). Evaluation of North Eurasian snow-off dates in the ECHAM5.4 atmospheric general circulation model. *Geoscientific Model Development*, 7(6):3037–3057.

Ramsay, B. (1998). The interactive multisensor snow and ice mapping system. *Hydrological Processes*, 12(February):1537–1546.

Randerson, J. T., Chen, Y., van der Werf, G. R., Rogers, B. M., and Morton, D. C. (2012). Global burned area and biomass burning emissions from small fires. *Journal of Geophysical Research*, 117(G4):G04012.

Reick, C. H., Raddatz, T., Brovkin, V., and Gayler, V. (2013). Representation of natural and anthropogenic land cover change in MPI-ESM. *Journal of Advances in Modeling Earth Systems*, 5(3):459–482.

Riahi, K., Grübler, A., and Nakicenovic, N. (2007). Scenarios of long-term socio-economic and environmental development under climate stabilization. *Technological Forecasting and Social Change*, 74(7):887–935.

Roeckner, E., Bäuml, G., Bonaventura, L., Brokopf, R., Esch, M., Giorgetta, M., Hagemann, S., Kirchner, I., Kornblueh, L., Rhodin, A., Schlese, U., Schulzweida, U., and Tompkins, A. (2003). The atmospheric general circulation model ECHAM5: Part 1: Model description. *MPI Report*, 349(349):1–140.

Roesch, A. and Roeckner, E. (2006). Assessment of snow cover and surface albedo in the ECHAM5 general circulation model. *Journal of Climate*, 19(16):3828–3843.

Rothermel, R. C. (1972). A mathematical model for predicting fire spread in wildland fuels. *USDA Forest Service Research Paper INT USA*, (INT-115):40.

Sand, M., Berntsen, T. K., Seland, O. y., and Kristjánsson, J. o. E. (2013). Arctic surface temperature change to emissions of black carbon within Arctic or midlatitudes. *Journal of Geophysical Research: Atmospheres*, 118(14):7788–7798.

Schneck, R., Reick, C. H., and Raddatz, T. (2013). Land contribution to natural CO2 variability on time scales of centuries. *Journal of Advances in Modeling Earth Systems*, 5(2):354–365.

Shindell, D. and Faluvegi, G. (2009). Climate response to regional radiative forcing during the twentieth century. *Nature Geoscience*, 2(4):294–300.

Sitch, S., Smith, B., Prentice, I. C., Arneth, A., Bondeau, A., Cramer, W., Kaplan, J. O., Levis, S., Lucht, W., Sykes, M. T., Thonicke, K., and Venevsky, S. (2003). Evaluation of ecosystem dynamics, plant geography and terrestrial carbon cycling in the LPJ dynamic global vegetation model. *Global Change Biology*, 9:161–185.

Skeie, R. B., Berntsen, T., Myhre, G., Pedersen, C. a., Strãm, J., Gerland, S., and Ogren, J. a. (2011). Black carbon in the atmosphere and snow, from pre-industrial times until present. *Atmospheric Chemistry and Physics*, 11(14):6809–6836.

Stamnes, K., Tsay, S. C., Wiscombe, W., and Jayaweera, K. (1988). Numerically stable algorithm for discrete-ordinate-method radiative transfer in multiple scattering and emitting layered media. *Applied optics*, 27(12):2502–2509.

Stanelle, T., Bey, I., Raddatz, T., Reick, C., and Tegen, I. (2014). Anthropogenically induced changes in twentieth century mineral dust burden and the associated impact on radiative forcing. *Journal of Geophysical Research : Atmospheres*, pages 526–546.

Stein, U. and Alpert, P. (1993). Factor Separation in Numerical Simulations. *Journal of the Atmospheric Sciences*, 50(14):2107–2115.

Stevens, B., Giorgetta, M., Esch, M., Mauritsen, T., Crueger, T., Rast, S., Salzmann, M., Schmidt, H., Bader, J., Block, K., Brokopf, R., Fast, I., Kinne, S., Kornblueh, L., Lohmann, U., Pincus, R., Reichler, T., and Roeckner, E. (2013). Atmospheric component of the MPI-M earth system model: ECHAM6. *Journal of Advances in Modeling Earth Systems*, 5(2):146–172.

Stier, P., Feichter, J., Kinne, S., Kloster, S., Vignati, E., Wilson, J., Ganzeveld, L., Tegen, I., Werner, M., Balkanski, Y., Schulz, M., and Boucher, O. (2005). The aerosol-climate model ECHAM5-HAM. *Atmospheric Chemistry and Physics Discussions*, 4(5):5551–5623.

Stohl, A., Klimont, Z., Eckhardt, S., Kupiainen, K., Shevchenko, V. P., Kopeikin, V. M., and Novigatsky, a. N. (2013). Black carbon in the Arctic: The underestimated role of gas flaring and residential combustion emissions. *Atmospheric Chemistry and Physics*, 13(17):8833–8855.

Stroeve, J., Box, J. E., Wang, Z., Schaaf, C., and Barrett, A. (2013). Re-evaluation of MODIS MCD43 Greenland albedo accuracy and trends. *Remote Sensing of Environment*, 138:199–214.

Thomas, G. E. and Stamnes, K. (1999). *Radiative Transfer in the Atmosphere and Ocean*. Cambridge Atmospheric and Space Science Series, Cambridge University Press, New York.

Thonicke, K., Spessa, A., Prentice, I. C., Harrison, S. P., Dong, L., and Carmona-Moreno, C. (2010). The influence of vegetation, fire spread and fire behaviour on biomass burning and trace gas emissions: Results from a process-based model. *Biogeosciences*, 7(6):1991–2011.

Toon, O. B., Mckay, C. P., Ackerman, T. P., and Santhanam, K. (1989). Rapid calculation of radiative heating rates and photodissociation rates in inhomogeneous multiple scattering atmospheres. *Journal of Geophysical Research*, 94(89):287–301.

Twomey, S. (1977). The Influence of Pollution on the Shortwave Albedo of Clouds. *Journal of the Atmospheric Sciences*, 34(7):1149–1152.

van Vuuren, D. P. and Carter, T. R. (2014). Climate and socio-economic scenarios for climate change research and assessment: Reconciling the new with the ol. *Climatic Change*, 122(3):415–429.

van Vuuren, D. P., Edmonds, J., Kainuma, M., Riahi, K., Thomson, A., Hibbard, K., Hurtt, G. C., Kram, T., Krey, V., Lamarque, J. F., Masui, T., Meinshausen, M., Nakicenovic, N., Smith, S. J., and Rose, S. K. (2011). The representative concentration pathways: An overview. *Climatic Change*, 109(1):5–31.

Vaughan, D., Comiso, J., Allison, I., Carrasco, J., Kaser, G., Kwok, R., Mote, P., Murray, T., Paul, F., Ren, J., Rignot, E., Solomina, O., Steffen, K., and Zhang, T. (2013). Observations: Cryosphere. *Climate Change 2013: The Physical Sci- ence Basis. Contribution of Working Group I to the Fifth Assessment Report of the Intergovernmental Panel on Climate Change*, pages 317–382.

Veira, A., Kloster, S., Schutgens, N. a. J., and Kaiser, J. W. (2015a). Fire emission heights in the climate system Part 2: Impact on transport, black carbon concentrations and radiation. *Atmospheric Chemistry and Physics*, 15(13):7173–7193.

Veira, A., Lasslop, G., Kloster, S., and Max, I. (2015b). Wildfires in a warmer climate : Emission fluxes , emission heights and black carbon concentrations in. *Journal of Geophysical Research - Atmospheres*, pages 1–67.

von Hardenberg, J., Vozella, L., Tomasi, C., Vitale, V., Lupi, A., Mazzola, M., Van Noije, T. P. C., Strunk, A., and Provenzale, A. (2012). Aerosol optical depth over the Arctic: A comparison of ECHAM-HAM and TM5 with ground-based, satellite and reanalysis data. *Atmospheric Chemistry and Physics*, 12(15):6953–6967.

Wang, X., Doherty, S. J., and et al. Huang, J. (2013). Black carbon and other light-absorbing impurities in snow across Northern China. *Journal of Geophysical Research: Atmospheres*, 118(3):1471–1492.

Ward, D. S., Kloster, S., Mahowald, N. M., Rogers, B. M., Randerson, J. T., and Hess, P. G. (2012). The changing radiative forcing of fires: Global model estimates for past, present and future. *Atmospheric Chemistry and Physics*, 12(22):10857–10886.

Warren, S. G. (1982). Optical properties of snow. *Reviews of Geophysics*.

Warren, S. G. (2013). Can black carbon in snow be detected by remote sensing? *Journal of Geophysical Research: Atmospheres*.

Warren, S. G. and Wiscombe, W. J. (1980). A model for the spectral albedo of snow. II: Snow containing atmospheric aerosols. *Journal of Atmospheric Sciences*, 37:2734–2745.

Westerling, A. L., Hidalgo, H. G., Cayan, D. R., and Swetnam, T. W. (2006). Warming and earlier spring increase western U.S. forest wildfire activity. *Science*, 313(5789):940–3.

Xu, B., Cao, J., Hansen, J., Yao, T., Joswia, D. R., Wang, N., Wu, G., Wang, M., Zhao, H., Yang, W., Liu, X., and He, J. (2009). Black soot and the survival of Tibetan glaciers. *Proceedings of the National Academy of Sciences*, 106(52):22114–22118.

Xu, B., Cao, J., Joswiak, D. R., Liu, X., Zhao, H., and He, J. (2012). Post-depositional enrichment of black soot in snow-pack and accelerated melting of Tibetan glaciers. *Environmental Research Letters*, 7(1):014022.

Ye, H., Zhang, R., Shi, J., Huang, J., Warren, S. G., and Fu, Q. (2012). Black carbon in seasonal snow across northern Xinjiang in northwestern China. *Environmental Research Letters*, 7(4):044002.

Zege, E., Katsev, I., a.V. Malinka, a.S. Prikhach, Heygster, G., and Wiebe, H. (2011). Algorithm for retrieval of the effective snow grain size and pollution amount from satellite measurements. *Remote Sensing of Environment*, 115(10):2674–2685.

Zender, C. S., Bush, B., Pope, S. K., Bucholtz, A., Collins, W. D., Kiehl, J. T., Valero, F. P. J., and Vitko, J. (1997). Atmospheric absorption during the Atmospheric Radiation Measurement (ARM) Enhanced Shortwave Experiment (ARESE). *Journal of Geophysical Research*, 102(D25):29901.

Zhang, K., O'Donnell, D., Kazil, J., Stier, P., Kinne, S., Lohmann, U., Ferrachat, S., Croft, B., Quaas, J., Wan, H., Rast, S., and Feichter, J. (2012). The global aerosol-climate model ECHAM-HAM, version 2: Sensitivity to improvements in process representations. *Atmospheric Chemistry and Physics*, 12:8911–8949.

Zhao, C., Hu, Z., Qian, Y., Ruby Leung, L., Huang, J., Huang, M., Jin, J., Flanner, M. G., Zhang, R., Wang, H., Yan, H., Lu, Z., and Streets, D. G. (2014). Simulating black carbon and dust and their radiative forcing in seasonal snow: a case study over North China with field campaign measurements. *Atmospheric Chemistry and Physics*, 14(20):11475–11491.